A study of the mechanical behavior of thin polycrystalline platinum and platinum-ruthenium thin films.

INFORMATION TO USERS

This manuscript has been reproduced from the microfilm master. UMI films the text directly from the original or copy submitted. Thus, some thesis and dissertation copies are in typewriter face, while others may be from any type of computer printer.

The quality of this reproduction is dependent upon the quality of the copy submitted. Broken or indistinct print, colored or poor quality illustrations and photographs, print bleedthrough, substandard margins, and improper alignment can adversely affect reproduction.

In the unlikely event that the author did not send UMI a complete manuscript and there are missing pages, these will be noted. Also, if unauthorized copyright material had to be removed, a note will indicate the deletion.

Oversize materials (e.g., maps, drawings, charts) are reproduced by sectioning the original, beginning at the upper left-hand corner and continuing from left to right in equal sections with small overlaps.

ProQuest Information and Learning
300 North Zeeb Road, Ann Arbor, MI 48106-1346 USA
800-521-0600

A study of the mechanical behavior of thin polycrystalline Pt and Pt-Ru thin films

by

Seungmin Hyun

Presented to the Graduate and Research Committee

of Lehigh University

in Candidacy for the Degree of

Doctor of Philosophy

in

Materials Science and Engineering

Lehigh University

July, 2002

Approved and recommended for acceptance as a dissertation in partial fulfillment of the requirements for the degree of Doctor of Philosophy

7/23/02

Date

Dr. Richard P. Vinci
Dissertation Advisor

7/29/02

Accepted Date

Committee Members:

Dr. Richard P. Vinci
Committee Chair

Dr. Helen M. Chan
Committee Member

Dr. Alwyn Eades
Committee Member

Dr. Ray A. Pearson
Committee Member

Dr. Miltiadis K. Hatalis
Committee Member

Acknowledgement

I am deeply indebted to many people for their help. Without them, I could not finish the long journey at Lehigh University. First and foremost, I would like to express my sincere appreciation to Prof. Richard P. Vinci for providing me with the means and the guidance to complete this work. Although he had a very busy schedule, he was always accessible. I enjoyed conversations with him and learned a lot of things from him. I also thank to the members of my research committee: Prof. Alwyn Eades for helping me with TEM image analysis, Prof. Helen M. Chan, Prof. Miltiadis K. Hatalis and Prof. Ray A. Pearson.

I would like to thank Dr. Oliver Kraft at Max Planck Institut für Metallforschung in Germany for providing me with Pt and Pt-Ru alloy films. I also appreciate to Dave Ackland for helping me with TEM operations. I appreciate the help from Prof. Hatalis's Group. Especially, I thank Sooraj Karnik for showing me how to use α-step and spin coater.

I also thank Xiaodong Tao for teaching me how to analyze grain size distribution. I appreciate to Dr. Kevin Luer for helping me with sample annealing and giving advice for lab. settings. Dr. Paul Flinn and Mike Mori are gratefully acknowledged for their assistance of wafer curvature measurement at Stanford University. I also appreciate the help from our group members: Dr.Richard R. Chromik for comments regarding my dissertation, Dr. Ralph Spolenak (now Max Planck Institut für Metallforschung in Germany) for Focused Ion Beam operation and wafer curvature measurements, Paul El-Deiry and Nicholas Barbosa for making delightful school life.

I would like to thank all former and current members of Korean student society at Lehigh University (Drs Jaechul Oh, Sungduk Kim, Jinhyun Kim, Hyoungchan Ha and special tennis members : Dongjoo Kim, Dongjun Cho and Choung-Yeol Seo) for making my life enjoyable.

Finally, I owe to my deep gratitude to my family. I thank my parents for their unconditional support and endless encouragement during the study. Also I thank my aunts, Yoosook Park and Yoosoon Cho, for their love. Without them, I could not continue Ph. D. course for many years at this country. Especially for my lovely wife, Seonghee, I really appreciate her patience and sacrifice.

Funding for this work was supported by NSF DMR-0072134, subcontract PY-0826

List of Tables

List of Figures

Ch. 1

Ch. 2

Ch. 3

Ch. 4

Ch. 5

Ch. 6

Abstract

In this study, the mechanical behaviors of Pt and Pt-Ru alloy thin films have been studied using the nanoindentation and wafer curvature techniques. These films are potential candidates as electrode materials for DRAM applications. However, several reliability issues related to stress problems have arisen due to the harsh processing conditions that exist during the formation of thin film capacitors. We investigated deformation mechanisms of Pt and Pt-Ru alloy thin films for the application. The films were prepared by DC magnetron sputtering, and the composition of Ru was varied from 0 to 20 wt% by codeposition.

The local deformation behavior of pure Pt films was investigated using the nanoindentation method. The deformation behavior was studied in terms of both grain size and proximity of the indenter tip to a grain boundary. Small-scale deformation behavior was strongly related to the microstructural length scale (grain size). Dislocation emission from grain boundaries was proposed as a mechanism for the unique nanoindentation loading behaviors.

The effectiveness of solid solution strengthening was systematically explored in the Pt-Ru alloy films. Wafer curvature and nanoindentation techniques were used to investigate the stress mechanism of the films, and the influence of solid solution alloying was observed as a function of Ru content. The experimental results were compared to flow stress calculations that are based on dislocation motion in thin films. The detailed analyses of strengthening mechanisms show that that the solid solution strengthening mechanism is mostly responsible for the film hardening.

The stress evolution of Pt films at elevated temperatures was also explored as a function of grain size. The stress-temperature behavior of Pt shows a dependence on the grain size. Two models, deformation mechanisms map and diffusional wedge model, were used to understand the stress-temperature behavior of Pt films. Diffusional wedge model does agree with the stress-temperature behavior of Pt films. A combination of the two models is found to be most accurate in the case of a non-columnar film.

Ch. 1 Introduction

1.1 Stress related reliability of metal thin films

The stress effects on the various metal thin lines in microelectronic applications are very important because high stress can cause stress-voiding [Lee et al. 2002], hillock growth [Kristensen et al. 1991, Kim et al. 2000], electromigration [Kao et al. 2001, and loss of adhesion [Mattox 1982]. Some of the effects on metal films are shown in Figure 1.1. During integrated circuit fabrication, materials go through many thermal cycles. An important origin of high stress during fabrication is the thermal mismatch between the metal and the surrounding materials. Tensile or compressive stresses develop during thermal cycling, and these stresses can cause the reliability problems. Tensile stress induces voids in metal lines. Compressive stress causes hillock growth on the films. Electromigration, the mass transport by the electric field and charge transfer, occurs in interconnecting lines in microelectronic devices under a high current density.
At one end of the line, atoms are depleted resulting in tensile stresses, but at the other end, atoms accumulate and compressive stresses develop. A large void is formed in order to relax the tensile stresses and hillocks, extrusions on the metal surface, reduce the compressive stresses [Tu et al. 1992].

In application of thin film metallization, adhesion to the substrate and to the surrounding walls is very important. The film/substrate interface is affected by several factors such as a strong bonding across the film/substrate interface and an absence of long-term degradation modes (e.g., corrosion) [Mattox 1982]. Residual stress or external stress is the one of the important factors.

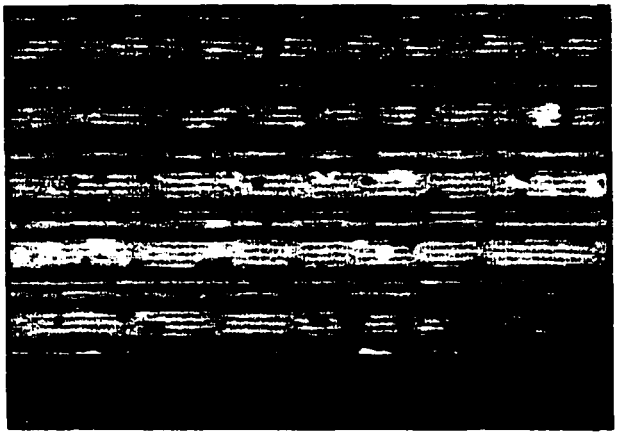

(a)

(b)

(c)

(d)

Figure 1.1. Stress effects on metal films. (a) stress-induced voids in Al lines under silicon nitrides [Lee et al. 2002], (b)electromigration ; void formed in a Al(Cu) line [Kao et al. 2001]. (c) a sunken grain in a blanket Al film [Kristensen et al. 1991]. (d) hillock formation in a Pt film [this work]

Compressive stress can cause the film to buckle up off and tensile stress can force the film to peel.

1.2 Pt electrodes for thin film capacitors

In integrated circuit (IC) memory technology, the increasing integration density of dynamic random access memory (DRAM) cells has resulted in the need for high dielectric constant oxide films as capacitor materials. It may be possible to achieve high device densities by using ferroelectrics. As potential candidates for ferroelectric materials, lead zirconium titanate (PZT), barium titanate, barium strontium titanate (BST), strontium titanate, and lanthanum-doped PZT have been investigated [Sreenivas et al. 1988, Li 1991, Sakuma et al. 1990, Takemura et al. 1994, Horikawa et al. 1993, Jones et al. 1992].

Integration of ferroelectric thin film capacitors onto silicon requires a suitable electrode. The formation of thin film capacitors involves the deposition of the dielectric material over a previously formed electrode. Figure 1.2 shows a cross-sectional TEM image of a stacked capacitor structure [Kotecki et al. 1999] and the schematic diagram of the stacked capacitor cell. High processing temperatures and high oxygen partial pressure are common during the synthesis of ferroelectric oxide films. It is important that no interfacial low dielectric constant layer should be formed during high-temperature oxygen processing. A layer with low dielectric constant, formed in series with a high-permittivity material, will drastically reduce the net charge storage density of the capacitor, and hence, reduce the field across the high-permittivity dielectric. To be compatible with Si and ferroelectric processing steps, the electrodes should be a good

oxygen diffusion barrier and should have good adhesion, high electrical conductivity after ferroelectric deposition and good mechanical hardness at high temperature.

Various electrode materials, ranging from noble metal films to complex conducting oxides, have been studied by previous researchers. Hren [Hren et al. 1992] has shown the problems relating to the preparation of different electrode materials (Pt, Pt/Ti, RuO_2) and their compatibility with ferroelectric PZT thin films. Parikh [Parikh et al. 1990] has evaluated the compatibility of various diffusion barriers (TiNx, TiOx, ZrOx) for PZT deposition on silicon. Conducting oxide electrodes have been also investigated to improve degradation phenomena such as electrical fatigue and a diffusion of Pb through the electrode when PZT is used [Al-Shareef et al. 1996, Ramesh et al. 1992, Lee et al. 1993, Bernstein et al. 1993]. However, oxide electrodes such as RuO_2 and IrO_2 cause a leakage current problem.

Pt electrodes have been widely studied for electrode applications due to their excellent resistance to oxidation and good conductivity. In addition, platinum has a high work function and high hardness at high temperature, making it a good candidate for electrode material for capacitor applications. However, an annealing ambient such as O_2 and N_2 affects interfacial electrode reactions (Pt/Ti and Pt/Ti/TiN) [Olowolafe et al. 1993]. Material diffusion through Pt grain boundaries can cause composition change of the ferroelectric material. Finally Pt has poor adhesion to dielectric materials. To overcome leakage current problem in oxide electrodes and oxygen diffusion and adhesion problems in Pt electrodes, novel electrode systems of Pt alloys are investigated in this work. Pt and Pt-Ru alloy systems were selected to investigate the applications for electrode materials. Although the electrical characterizations are critical, this work will

only directly address mechanical issues. Large fraction of Ru in Pt matrix produces single-phase alloy system (solid solution alloy). Small amounts of Ru in Pt dramatically increase the hardness of the alloy [Metal Handbook 1990]. The advantages of solid solution alloying on high temperature strength have been reported in the literature for bulk materials [Metal Handbook 1990]. The increase in strength is the result of interaction between the stress field of a dislocation and the stress field associated with the solute atom. Alloying can increase the tensile strength by a factor of 2 to 4 times [Savitsky et al. 1978] and can decrease the creep rate by more than an order of magnitude [Usikov et al. 1981]. Alloying may also improve the adhesion with the substrate and block the diffusion of oxygen.

Most electrode studies have focused on interface reactions and electrical properties of devices. Only a few stress evolution studies have been performed on the electrodes and thin film capacitors [Spierings et al. 1995]. The stress on devices is often large and may exceed the strength of the film resulting in cracking and delamination. Very large thermal stresses in the electrode are induced in these materials during the manufacture of thin film capacitors. This is because the metal has a coefficient of thermal expansion that differs widely from that of the silicon substrate (Pt : 9×10^{-6}/°C and Si : 3×10^{-6}/°C). The large stress level may cause poor adhesion between the Pt film and SiO_2 layer and promote hillock growth on the surface of the film resulting in direct contact between the top and bottom electrodes. Thus, it is important to understand the mechanisms that control the mechanical properties of these thin films so that integrated circuit structures can be designed for mechanical reliability as well as for electronic device performance.

The stress relaxation mechanisms of metal films have been studied by previous researchers to understand the mechanical behaviors of thin films [Thouless et al. 1993, Gao et al. 1999]. However, these relaxation mechanisms are still not fully understood. Moreover, the mechanical properties of solid solution thin films have not been heavily studied. Only mechanical behavior of bulk forms of these alloys has been investigated. Previous studies of mechanical behavior mostly focused on pure metal films such as Al and Cu. In this work, thin films of solid-solution alloy were studied to improve fundamental understanding of the deformation mechanisms active in thin films. High temperature deformation mechanisms such as creep and diffusional flow were investigated to predict the stress level of Pt thin films. Microstructure evolution and adhesion to the substrate of thin films with various Ru contents were briefly studied in this work. Length scale issues affecting deformation behavior of Pt films were also explored by the nanoindentation method.

1.3 Outline

Chapter 2 briefly reviews some the previous work on stress development in metal films. Low temperature and high temperature deformation mechanisms in metallic films and stress testing methods are also reviewed.

Chapter 3 provides detailed experimental procedures used in this work including sample preparation and characterization methods of the Pt and Pt-Ru thin films.

Chapter 4 presents microstructure characterization of Pt and Pt-Ru films. Hillock formation in the films after heating is also examined according to different experimental conditions.

Ch. 2 Background

In this chapter, the Pt-Ru alloy system is introduced and a summary of the previous work on stress development in metal films is presented. Mechanisms regarding mechanical properties of thin films are also reviewed.

2.1 Pt-Ru system

The Pt-Ru phase diagram contains a large homogenous solid solution fraction as shown in Figure 2.1. Up to 46wt% of Ru in Pt matrix, single phase alloy, Pt type (FCC), can be produced at high temperature. In the composition range of 0 to 33wt% of Pt a solid solution in HCP Ru also exists in the system. The solid solution alloying effect on mechanical strength is shown in Figure 2.2 for the bulk Pt-Ru system. A small fraction of Ru in the Pt matrix improves the strength of the Pt-Ru system significantly. In this study, the Pt-rich single phase with Ru concentration in the range of 0 to 20 wt% is selected to investigate mechanical behavior of Pt-Ru thin films under well-defined conditions.

2.2 Thin film formation and structure development

There are three types of growth mechanisms observed in film formation [Ohring 1992]; (1) island (Volmer-Weber), (2) layer and (3) Stranski-Krastanov. The island growth mechanism occurs when atoms in the film are bound more strongly to each other than to the substrate. So, the small clusters on the substrate grow in three dimensions to form islands.

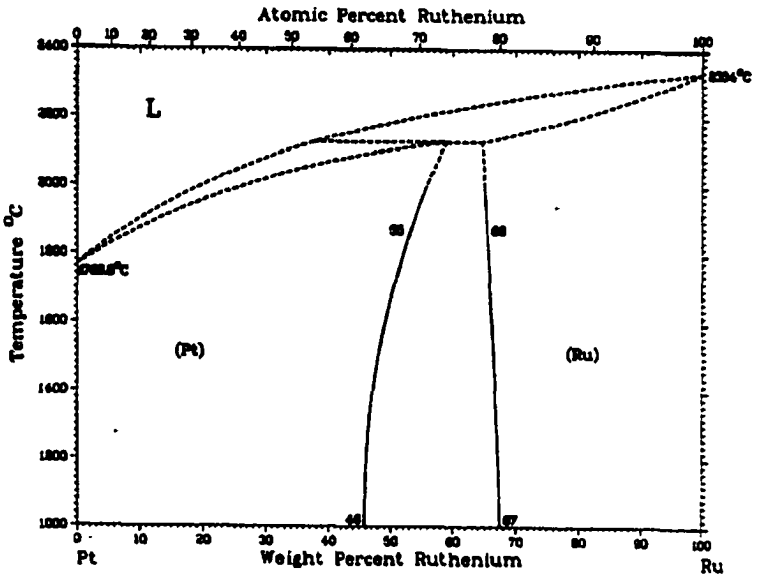

Figure 2.1. Pt-Ru Binary alloy phase diagram [Massalski "Binary alloy phase diagrams 1990].

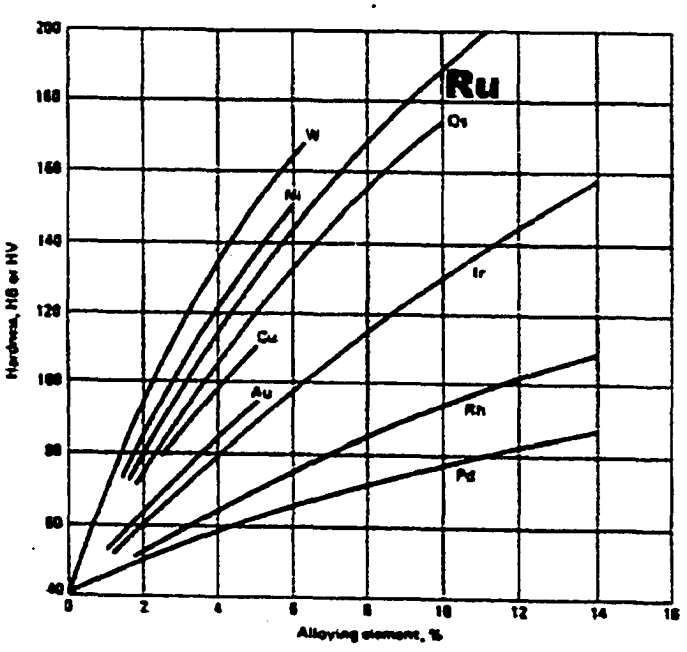

Figure 2.2. Hardness change of bulk Pt according to Ru content [Metal Handbook 1990].

Layer growth happens when bonding of atoms in the film is less strong than that of atoms to the substrate. A small stable nucleus occurs in two dimensions resulting in planar sheets. Finally, the Stranski-Krastanov growth mechanism is the combination of the previous two mechanisms. After formation of one or more monolayers (layer growth), the island growth mechanism dominates in film formation.

2.2.1 Microstructure from physical vapor deposition (PVD)

In the study of PVD (sputtering and evaporator) coatings, the microstructure of as-deposited films depends on various parameters such as substrate temperature, gas pressure, deposition rate and impurities. The effect of deposition parameters on microstructures of as-deposited films is often described using the "Structure Zone Model" (SZM) or "Zone Model". The model was initially proposed by Movchan and Dechishin [Movchan et al. 1969] for thick films of Ti, Ni, W, ZrO_2, Al_2O_3 and Fe deposited at high deposition rates by electron beam evaporation. The authors explained that the homologous deposition temperature (T/T_m, ratio of deposition temperature to melting temperature) corresponded to three different microstructure zones. Zone 1 (T/T_m <0.3) consists of tapered crystals that have voided boundaries. Zone 2 ($0.3< T/T_m <0.5$) is characterized by columnar grains, separated by dense boundaries, that increase in size with increasing substrate temperature. Zone 3 ($0.5< T/T_m <1$) consists of equiaxed grains.

Thornton [Thornton 1977] reviewed the structure zone model after a brief survey of some film structures produced by evaporation and sputtering methods. High deposition rates were used for thick film fabrication (Ti, Cr, Fe, Cu, Mo and Al on metal and glass substrates). For sputtering, he added the effect of an additional deposition parameter, Ar

gas pressure, on the previous Zone Model. The expanded Zone Model, which predicts coating microstructure as a function of the substrate temperature and inert gas pressure, is shown in Figure 2.3. Many structure observations can be explained by this approach. The expanded Zone model is basically same as the previous zone models proposed by Movchan and Dechishin, but Zone T is added to account for a dense fibrous structure with a smooth, highly reflective surface.

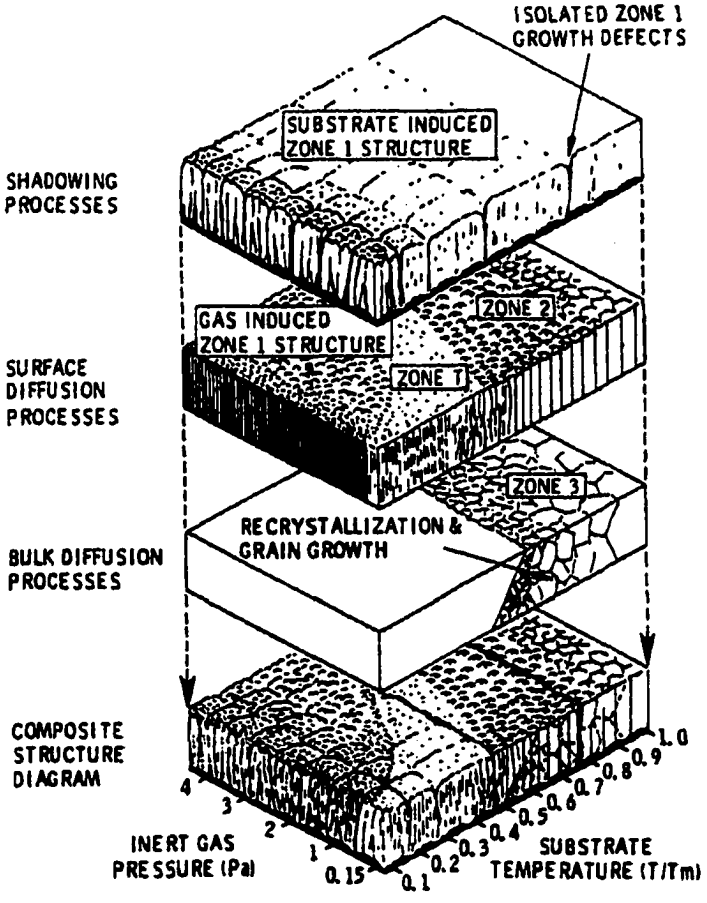

Figure 2.3. Schematic representation showing of the Thornton Zone model in terms of temperature and inert gas pressure [Thornton 1977].

Grovenor [Grovenor 1984] showed that the structure of the thick films can be classified into four characteristic zones according to film growth mechanisms which

depend on the substrate temperature. The model was based on the concept of variations in individual grain boundary mobilities that cause three characteristic regimes of growth. The new part of this approach is based on bulk process, especially grain growth, in contributing to the structure of films. The zone model for the grain structure of vapor deposited metal films is shown in Figure 2.4.

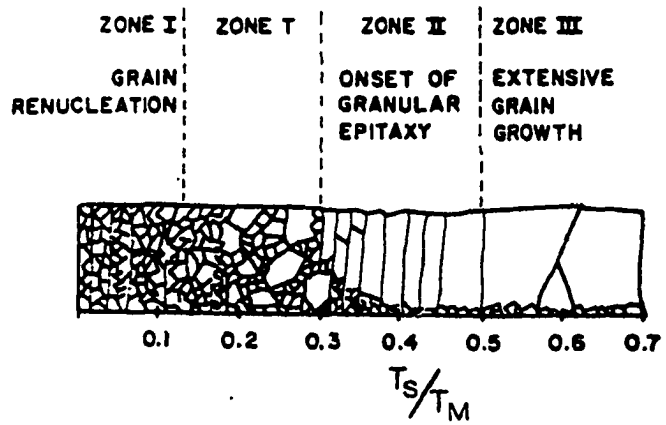

Figure 2.4. Zone model for evaporated metal film [Grovenor 1984].

In zone I, the grains are equiaxed with a fine grain diameter and all grain boundaries are almost immobile. In zone T, some fraction of the boundaries become mobile, and this kind of grain growth produces a bimodal grain structure. In zone II, all grain boundaries are mobile and columnar structures with uniform grain diameter are produced.
Zone III is characterized by lateral grain growth with grain sizes larger than the film thickness. The zone I structure is observed in both the thin and thick films. It is suggested that the fine equiaxed grains are always the initial structure of a deposit whatever the

substrate temperature. The transition from zone I to zone T to zone II presumably arises from the change in the mobility of grain boundaries with increasing temperature.

2.3 Intrinsic stress development in thin film

The stress evolution in thin films has been studied mostly in the context of reliability problems in microelectronic applications. The large residual stress often observed during deposition leads to severe problems, which include delamination, buckling and cracking. If the stress origin of thin films can be understood, then reliable production in industry can be achieved by controlling the stress behaviors of thin films.

Total stress is the sum of the thermal stress and intrinsic stress. The thermal stress is caused by the difference in the thermal expansion coefficients of the film and the substrate during the temperature change. The intrinsic stress depends on the film deposition parameters because deposition conditions affect the film microstructure resulting in stress development. Several researchers have explored intrinsic stress evolution in thin films. In this section, several works are represented to understand the stress evolutions during deposition and processing.

2.3.1 Temperature effect

The temperature of deposition plays an important role in stress development. If the ratio of deposition temperature divided by melting temperature, T/Tm, exceeds 0.25~0.3, thermal stress dominates because atomic mobility is large. Otherwise, intrinsic stress dominates at low T/T_m. Low melting point materials such as Al and Mg are soft at room temperature and have a high coefficient of thermal expansion. The intrinsic stress

of soft materials is less likely to be affected by deposition conditions because thermal stress is the dominant factor. On other hand, high melting point materials such as chrominum, molybdenum, platinum and tungsten are harder and have a relatively low coefficent of thermal expansion, resulting in high intrinsic stress. The intrinsic stress of high melting point materials depends strongly on deposition parameters.

2.3.2 Ar pressure effect

Thornton [Thornton et al. 1979] studied the internal stresses in thin films deposited at low T/T_m using magnetron sputtering sources. The transitions between compressive and tensile stresses for various metal thin films were observed by changing the working pressures. Compressive internal stress can be obtained under low Ar working pressure, due to the bombardment by energetic argon neutrals reflected from the cathode. The reflected argons can readily penetrate the film surface and become buried in the surface, or the argons knock atoms on the surface resulting in high density films (atomic peening effect) [d'Heurle 1989]. Internal stress change as a function of the argon pressure is shown in Figure 2.5. Ar gas pressure plays an important role in establishing the intrinsic stress.

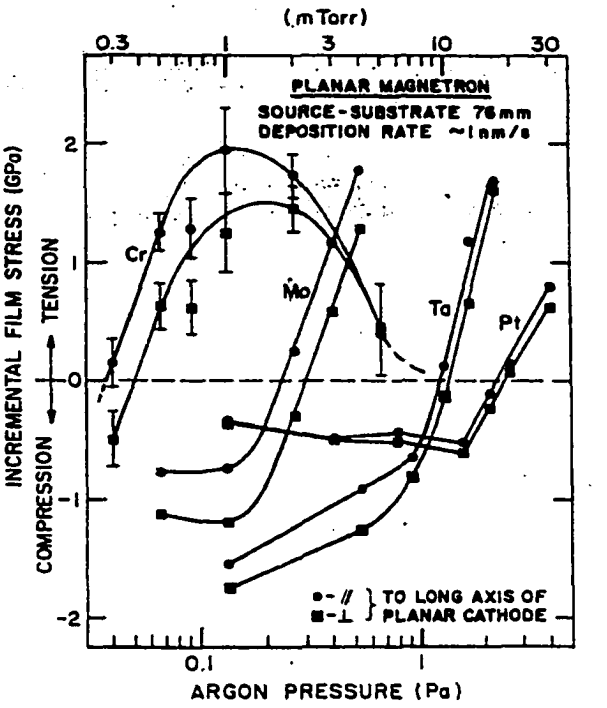

Figure 2.5. Biaxial internal stresses vs. argon working pressure for Cr, Mo, Ta and Pt metal films sputtered from a DC planar magnetron source onto glass [Hoffman 1982].

2.4. Stress in Blanket Pt films on Si substrate

The stress in an elastically isotropic film on a rigid substrate is biaxial [Nix 1989]. If x and y are mutually perpendicular axes in the plane of the film, and z is a normal axis to the film, the strains and stresses in the film are defined by

$$
\begin{aligned}
E\varepsilon_{xx} &= \sigma_{xx} - \nu(\sigma_{yy} + \sigma_{zz}) \\
E\varepsilon_{yy} &= \sigma_{yy} - \nu(\sigma_{xx} + \sigma_{zz}) \\
E\varepsilon_{zz} &= \sigma_{zz} - \nu(\sigma_{xx} + \sigma_{yy}) \qquad (2.1) \\
\varepsilon &= \varepsilon_{xx} = \varepsilon_{yy} = -\frac{e_T}{3} \\
\sigma_{xx} &= \sigma_{yy} = \sigma,\ \sigma_{zz} = \sigma_{xy} = \sigma_{yz} = \sigma_{xz} = 0
\end{aligned}
$$

where e_T is a dilatational transformation strain. The biaxial stress in the film can be shown by

$$\sigma = M\varepsilon \quad (2.2)$$

where M is the biaxial modulus of the film. For an isotropic film, M is defined by

$$M = \frac{E_f}{1-\upsilon_f} \quad (2.3)$$

where E_f is Young's modulus and ν_f is Poisson's ratio of the film.

For a film that is not isotropic, the orientation of the film decides the biaxial modulus. For a cubic material with a (111) normal to the substrate, the biaxial modulus is given by

$$M(111) = \frac{6C_{44}(C_{11}+2C_{12})}{C_{11}+2C_{12}+4C_{44}} \quad (2.4)$$

where C_{ij}'s are components of the stiffness matrix. For a cubic material with a (100) normal, M is given by

$$M(100) = C_{11} + C_{12} - \frac{2C_{12}^2}{C_{11}} \quad (2.5)$$

Although Young's modulus and Poisson's ratio of the film in the (100) plane are not isotropic, the biaxial modulus is isotropic in the plane of the film.

The biaxial moduli for Pt and Si are shown in Table 2.1.

Table 2.1. Biaxial moduli for Pt and Si

Material(orientation)	Biaxial modulus, M (GPa)
Pt(111)	337
Pt(100)	235
Si(111)	229
Si(100)	182

2.4.1 Stress evolution in thin film (stress-temperature relation)

Thermal stress is a function of the difference in the coefficient of thermal expansion of film and the substrate. The elastic thermal stress change during temperature change is given by

$$\Delta\sigma_{th} = M(\alpha_f - \alpha_s)(T_2 - T_1) \quad (2.6)$$

$\Delta\alpha\Delta T$ is the elastic thermal strain on the film.

There are two different types of stress-temperature behavior in FCC metal films. First, noble metal film, which has no native oxide on the surface, shows a relaxation behavior at high temperature. Second, metal films such as Al having a native oxide on the top of the film maintain a certain stress level at high temperature due to the retardation of the relaxation mechanism resulting from a passivation layer. A typical example of noble metal film stress evolution, which is the second Pt stress-temperature curve, is shown in figure 2.6(a). The stress at room temperature is tensile. At the initial heating, the film first deforms elastically (A region). Above 500°C, the stress curve deviates from elastic deformation and shows the plastic deformation behavior (B region) and the shape of the stress-temperature curve is determined by the plastic deformation mechanism (C region). During cooling, plastic deformation still dominates (C region) and upon further cooling, a stress increase occurs as the plastic deformation mechanism changes (D region). The behavior of stresses during thermal cycling in typical FCC Al thin films [Kim 2001] on a Si substrate is shown in Figure 2.6(b). As the film is heated, the greater thermal expansion of the aluminum film first relaxes the tensile stress in the film and later causes the film to go into a state of compression. At the initial unloading portion of the curve, the differences in thermal expansion between the film and substrate are accommodated

by elastic deformation of the film. The stress of the film decreases elastically with a slope of $M\Delta\alpha$ (region A). Above 140°C, plastic deformation starts and the compressive stress developed (region B). On cooling, a tensile stress developed elastically (region C). As the temperature further decreased, plastic deformation is observed (region D).

The stress-temperature relations are dominated by the effects of elastic and plastic deformation. However, microstructural changes also affect the stress evolution during thermal cycling. The densification of the film, mostly grain growth, causes a sudden stress relaxation during the first heating cycle [Nix 1989].

2.5 Techniques for thin film stress measurement

The conventional methods of measuring stress in bulk materials have very limited applications to thin films. A large area of a bulk specimen is measured with standard testing methods whereas a small area should be tested for materials in thin film form. Test methods for a material in its thin film form usually provide different quantities than macroscopic tests due to the small dimension. In addition, the behavior of a thin film attached to a substrate may be significantly different from an isolated film. Therefore, specific techniques for measuring stresses are required. Several techniques have been developed to test mechanical properties of thin films. Selected techniques from among the many existing mechanical characterization methods are described here.

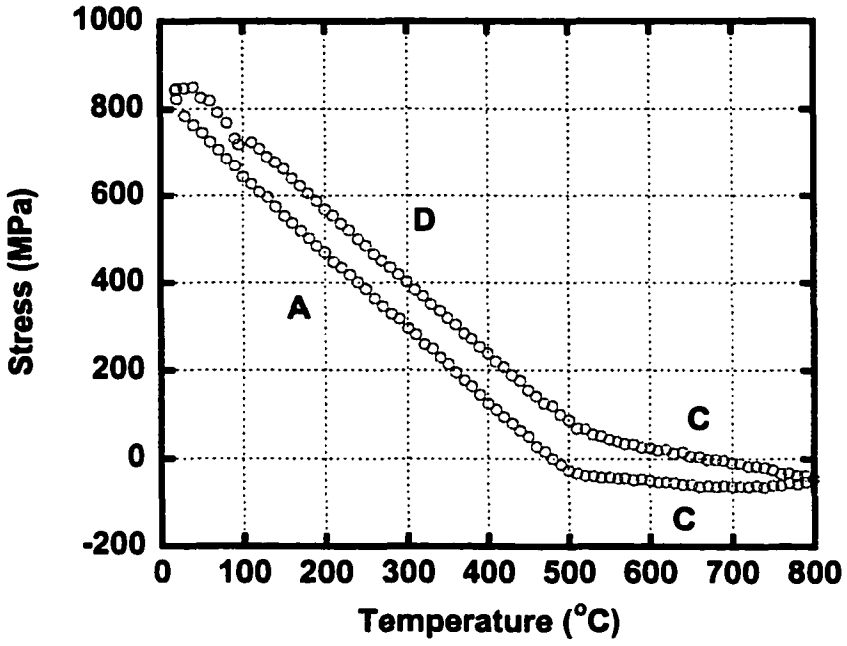

(a)

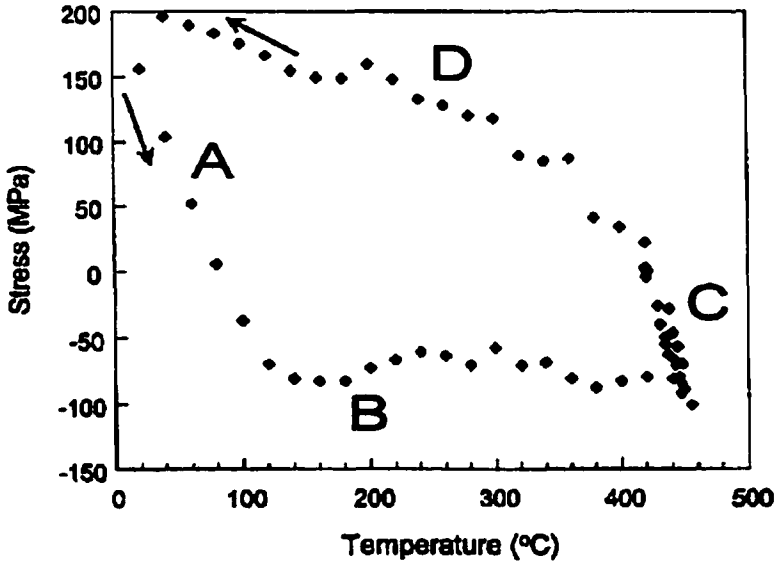

(b)

Figure 2.6. Stress-temperature curves during thermal cycling of metal thin films. (a) Pt film and (b) Al film [Kim 2001].

interplanar spacing of (hkl) planes perpendicular to the plane of the film, d_o, and the lattice interplanar spacing, $d_{\phi\psi}$, in an arbitrary direction defined by ψ and ϕ are known, the strain in that direction is expressed as

$$\varepsilon_{\phi\psi} = \frac{d_{\phi\psi} - d_o}{d_o} \qquad (2.8)$$

where ϕ is the angle in the plane of the film and $\varepsilon_{\phi\psi}$ is the strain.

These x-ray techniques provide a significant benefit over other methods for this particular application. It is possible to directly determine strains in metallic lines that lie beneath layers of other materials. However, x-ray strain measurement requires a high degree of accuracy. If the measuring structure is quite small, experimental difficulties arise due to resolution limits.

2.5.3 Bulge test

The bulge test has a long history for studying the mechanical properties of thin films. A thin film is clamped over a circular hole and a uniform pressure applied to one side of the film. So, a free-standing film portion on a substrate is required to deliver a direct pressure on the film as shown in Figure 2.7.

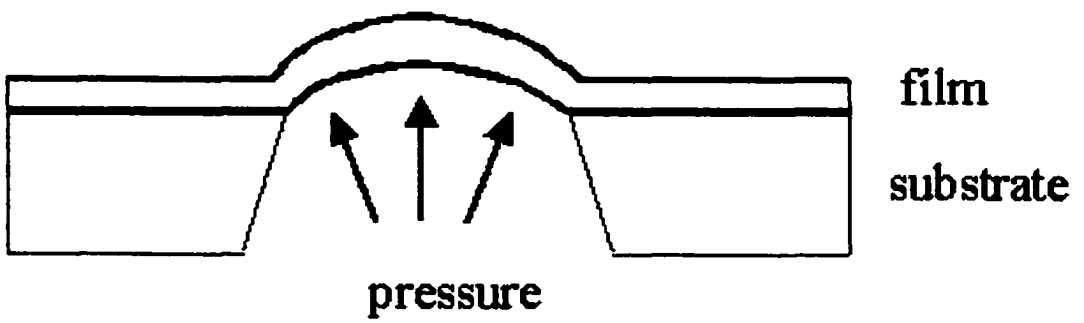

Figure 2.7. Schematic diagram of Bulge test

A stress-strain curve can be obtained from the relationship between the applied pressure and the deflection of the film. Young's modulus, Poisson's ratio and residual stress can all be measured [Vlassak et al. 1992]. The test does not require thermal cycling for introducing a strain on the film. Thus, unlike the wafer curvature technique, it is not necessary to have a difference in thermal expansion between film and substrate.

2.5.4. Nanoindentation

Nanoindentation test is a technique for measuring the hardness of materials. A hard indenter with a known load is pushed into a testing material, and displacement of the indentation is measured simultaneously. Indentation with very low load and displacement can be performed as shown in Figure 2.8. Elastic modulus and hardness of thin films can be measured [Oliver et al. 1992]. However, the indented material is deformed under a large hydrostatic pressure. So, the study of elastic and plastic properties of materials is difficult because such a high pressure may introduce phase transformations and densification [Nix 1989]. Detailed explanation of the technique will be given in Chapter 5, section 5.2.

2.5.5 Microtensile testing

The microtensile test is similar to the common uniaxial tensile test for bulk materials except that test samples are much smaller. A schematic diagram of the test is shown in Figure 2.9. A free-standing film is gripped and pulled in tension [Ruud et al. 1993]. The test is very simple and data interpretation is easy. However, sample

preparation is not easy because film deposition and etching, and mounting a free-standing film are very difficult procedures.

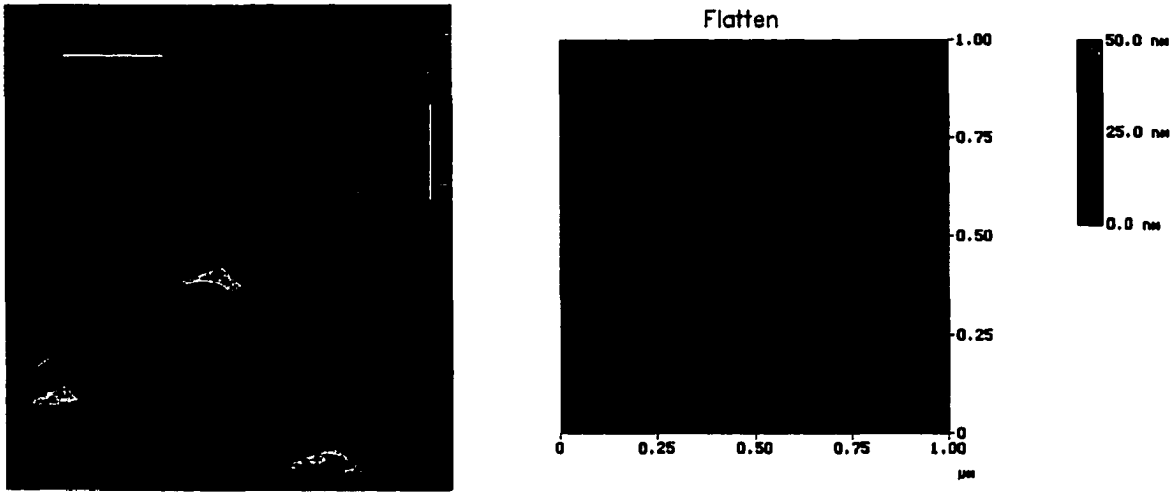

(a) SEM image of lead-free solder alloy (b) AFM image of Pt-10 wt% Ru film

Figure 2.8. Nanoindented area on (a) lead-free solder alloy [Richard Chromik at Lehigh University], (b) Pt-10 wt% Ru film

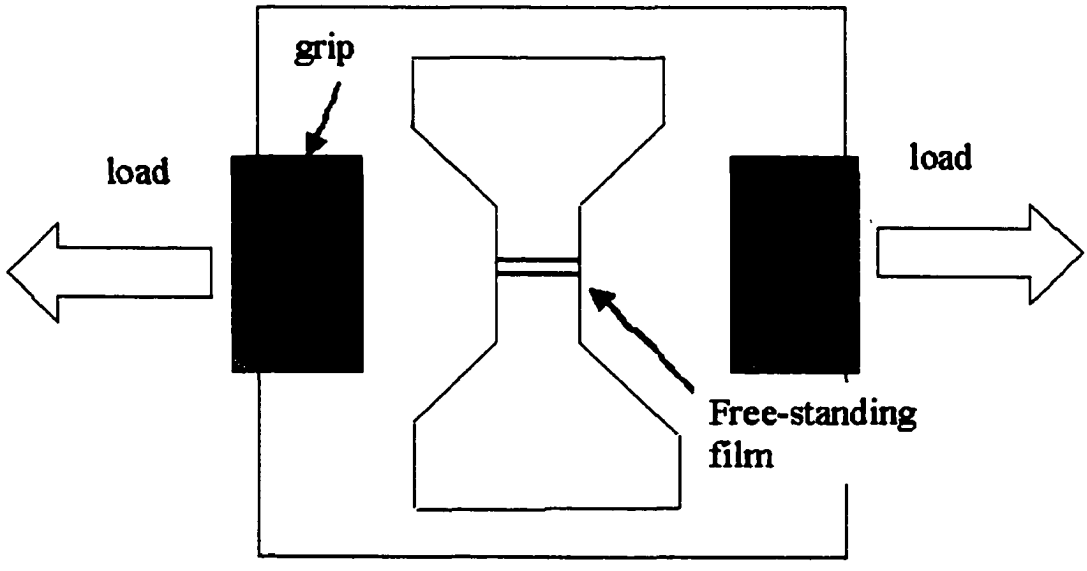

Figure 2.9. A schematic diagram of microtensile test

Nonuniform loading may introduce wrinkling of the free-standing film. Accurate measurement of mechanical properties can be only acquired through proper grip holding and good loading alignment. Direct measurement of the film stress without making a fully free-standing film can eliminate these difficult procedures. Tensile test of the film on a thinned polymer substrate can provide mechanical properties of the film [Kang et al. 1997] or an X-ray technique can be used to remove the substrate effects on the mechanical response of the film from the substrate [Kretschmann et al. 1997].

2.5.6 Microbeam bending test

Free-standing cantilever beams of the films are fabricated using micro-machining techniques to remove the underlying substrate [Nix 1989]. The ends of the beams are deflected using a depth sensing apparatus such as the nanoindenter shown in Figure 2.10. The beam's modulus can be obtained from the load, deflection and beam geometry. Plastic deformation of the beam can be studied with this technique. The beam bending load-displacement curve provides plastic properties such as the yield strengths and the strain hardening of microbeams.

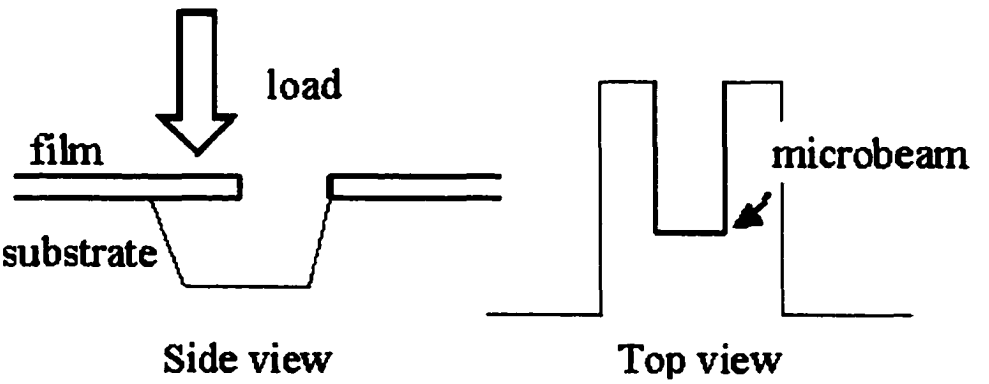

Figure 2.10. Schematic diagrams of microbeam bending test

2.6. Mechanical behavior of thin film

2.6.1 Low temperature and crystallography orientation dependent plasticity in continuous films

2.6.1.1 Dimensional constraint

A widely used model that describes the motion of dislocations in thin films (the dislocation glide model) was published by Nix [Nix 1989] and follows the approach introduced by Freund [Freund 1987]. As a dislocation moves in a film, a misfit dislocation is created at the film/substrate interface as shown in Figure 2.11.

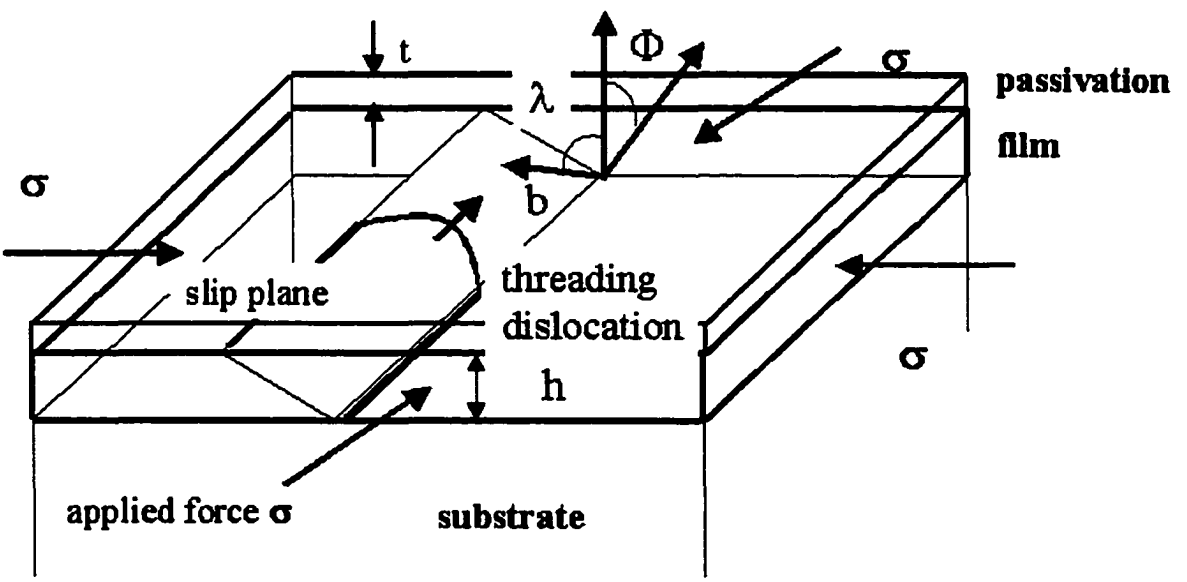

Figure 2.11. The dislocation motion at the film/substrate and film/passivation interfaces.

He considered the work done by the biaxial stress in the film when the dislocation travels a unit distance as given by

$$W_{strain} = \left(\frac{\cos\phi\cos\lambda}{b\sin\phi}\right)\sigma h \quad (2.9)$$

where ϕ and λ are the included angles between the glide plane normal direction and Burgers vector and the film normal direction, respectively. In order for the dislocation to move, the work done by the stress in the film must be equal to or greater than the energy of the dislocation that is created at the film substrate interface and at the film oxide interface if an oxide film is present on the surface of the film. The energy of the dislocation at the interface is

$$W_i = \left(\frac{b^2}{4\pi(1-\nu)}\right)\left[\frac{2\mu_f\mu_s}{(\mu_f+\mu_s)}\ln\left(\frac{\beta_s h}{b}\right)+\frac{2\mu_f\mu_o}{\mu_f+\mu_o}\ln\left(\frac{\beta_o t}{b}\right)\right] \quad (2.10)$$

where μ_f, μ_s and μ_o are the elastic shear moduli of the film, substrate and oxide, and h and t are the thickness of the film and oxide, and β_s and β_o are constants. Therefore, the equation describing the minimum biaxial stress needed to move the dislocation in the film is

$$\sigma = \frac{\sin\phi}{\cos\phi\cos\lambda}\frac{b}{2\pi(1-\nu)h}\left[\frac{\mu_f\mu_s}{\mu_f+\mu_s}\ln\left(\frac{\beta_s h}{b}\right)+\frac{\mu_f\mu_o}{\mu_f+\mu_o}\ln\left(\frac{\beta_o t}{b}\right)\right] \quad (2.11)$$

The length of the glide plane, or the distance between the interface pinning points, is given by $\sin\phi/h$, assuming that the grain structure is typically columnar in the film. The relation between the applied biaxial stress and the resolved stress on the glide plane involves the Schmid factor $(\cos\phi\cos\lambda)^{-1}$. From this model, the yield strength of the film depends inversely on the thickness of the film. However, no obstacles to dislocation motion or grain size strengthening have been considered in this model.

2.6.1.2 Grain size strengthening in thin film

Grain boundaries can greatly influence the stress levels in thin films by strengthening as described by the Hall-Petch relation [Griffin et al. 1986]. The Hall-Petch equation is based on the proposition that plastic flow involves glide of dislocations that can pile up at a grain boundary. When the stress concentration reaches a critical value, slip propagates to an adjacent grain. Since a small-grained material has a large number of grain boundaries that can block dislocation motion, a small-grained material is stronger than a large-grained material. Griffin has shown that the decrease in plastic flow stress at varying strains is correlated with the increase in grain size according to a Hall-Petch type relation [Griffin et al. 1986]. The Hall-Petch relationship is given by

$$\sigma = \sigma_o + kd^{-1/2} \quad (2.12)$$

where σ_o is average yield strength of a single grain, k is grain size coefficient and d is average grain size.

Venkatraman has shown that the strength of polycrystalline thin films depends on both their grain sizes and their thickness, and that the components of strengthening due to the film thickness and grain size can be separated by using two techniques [Venkatraman et al. 1992]. He used an anodic etch to reduce the thickness of Al films without changing the grain diameter. And a laser reflow method produced large grains reducing the grain boundary effect while keeping the thickness of the films constant. It was found that residual stresses were inversely related to both thickness and grain size.

$$\sigma_{flow} = \sigma_{flow,thick} + \sigma_{flow,gb} \quad (2.13)$$

the factor C_{ijk}. For FCC metals, C_{ijk} is 2.00, 1.42 and 3.46 for the (100), (110) and (111) orientations, respectively. The high yield stress of the (111) oriented film in comparison to the (110) and (100) films is clearly due to the difference between the C_{111}(=3.46) and the C_{100}(=2.00) for the two films. Deposited polycrystalline films are not in general perfectly textured. FCC metal films are usually (111) textured but also contain components of other orientations such as (110) and (112). If the grains with different orientations support different stresses, a local stress gradient will be established. The differences in stress levels lead to differences in strain energy density (W) between grains. W is defined by

$$W = M\varepsilon^2 \quad (2.15)$$

Energy density consists of elastic deformation term ($=\sigma_e^2/M$) prior to yielding and plastic deformation term ($\sigma_{y,ijk}^2/M$) in yielding (ijk) oriented grains, where M is the biaxial modulus.The energy differences between grains of different crystallographic orientation can exist and lead to the development of microstructure changes in thin film such as hillock growth and abnormal grain growth. It is proposed that under certain initial conditions of film thickness and grain size, the strain energy difference between strongly and weakly oriented grains, which are (111) and (100) in Al, respectively, provides sufficient driving force for the preferred growth of the weakly oriented grains. Thompson has also discussed the effects of film thickness on texture evolution during grain growth in thin film [Thomson et al. 1993].

2.6.2 High temperature deformation mechanisms

As described above, low temperature models predict a largely athermal strength behavior (low temperature plastic deformation). However, in microelectronic applications, thin film devices are often fabricated at high temperature. Thus, an understanding of the stress relaxation mechanisms at elevated temperature is required for the reliability of thin film devices.

Some approaches to modeling the stress relaxation of thin films assume that the creep properties can be described by these of the material in a bulk form. Thouless has modified the bulk strain-rate expressions for diffusional deformation to account for the stress state in thin films [Thouless et al. 1993]. The resulting deformation mechanism map model for thin films is based on the assumption that the film is allowed to slide freely on the substrate. However, the diffusional stress relaxation mechanisms are generally inhibited at the interfaces of the substrate and film because the presence of a strong adhesion between the substrate and the film prevents diffusional deformation at the interface.

Turlo and Gao [Turlo 1992, Gao 1999] introduced another diffusional deformation mechanism to explain the inhibition of the Thouless mechanism at the interface of the substrate and films. Constrained grain-boundary diffusion in the films on substrates is studied as a grain boundary diffusion problem in which no sliding and no diffusion are allowed at the interface of the film and the substrate. This mechanism explains that the effects of diffusional flow between the free surface and the grain boundary almost completely relax the stresses above the temperatures at which grain-

boundary diffusion can occur. Schematic diagrams of two models are shown in Figure 2.12.

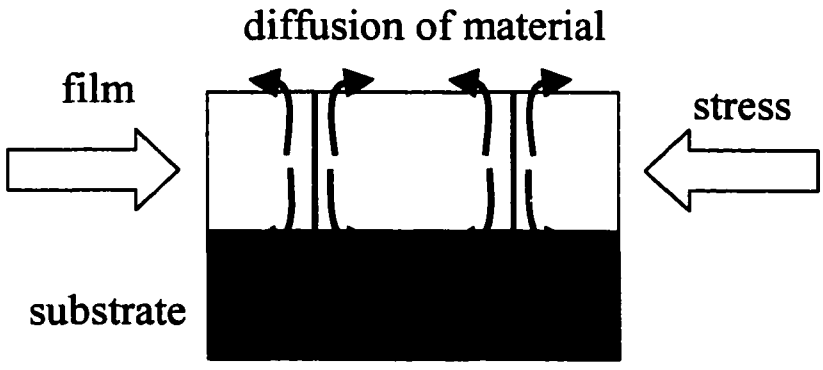

(a) Thouless model

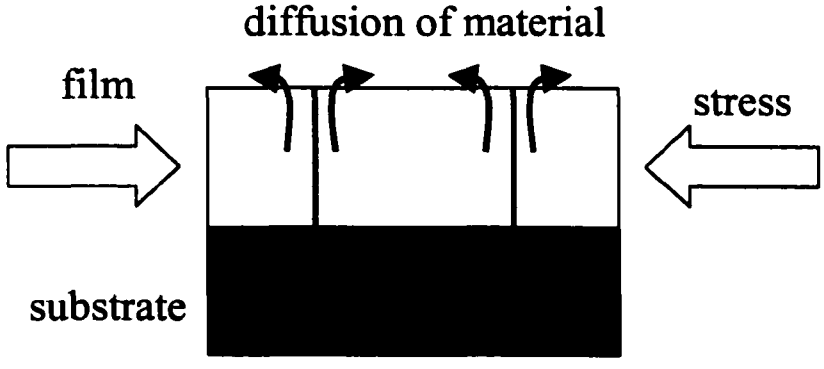

(b) Gao model

Figure 2.12. Comparison of Thouless model and Gao model.
(a) Diffusion of material from the grain boundary to the surface and the interface
(b) (Thouless model). (b) Diffusion of material from the grain boundary to the surface (Gao model). Both diffusional flow can relax compressive stress in the film. However, the Thouless model allows more extensive relaxation.

2.6.3 Passivation films

Stress in the metal lines used as interconnections in very large scale integration (VLSI) is important because stresses can be large enough to cause failure of metal lines. Complicated stress states can be induced in metal lines with the presence of dielectric layers that are encapsulating the metal lines. The stress states of the metal lines at elevated temperature are significantly affected by the presence of a passivation layer.

Shen [Shen et al. 1998] proposed a linear kinematic hardening model to explain stress-temperature behavior of passivated copper films after higher stress level is observed in passivated copper films compared to that in continuous copper films. The strain hardening effect on the residual stress was considered for passivation films. The temperature dependent yield behavior of the passivated Cu films was explained with a strong strain hardening mechanism based on a shear band model.

Ch.3 Experimental Procedure

3.1 Sample Preparation

3.1.1 Deposition of Pt and Pt-Ru Thin Films

Pt and Pt-Ru alloy films were prepared from two sputtering systems : one located in Germany (Max Planck Institut für Metallforschung, Stuttgart, type 1 film) and the other at Lehigh University (type 2 film). The main difference between the two systems is that the system at Germany is equipped with an Ar ion gun for the substrate pre-cleaning procedure. Pure Pt 99.99% and Pt-20wt%Ru 99.9% alloy sputtering targets were used to produce the Pt and Pt-Ru films. The substrates were 3 inch diameter Si (100) wafer with a thermally grown oxide layer approximately 100 nm thick. The total thickness of each wafer was about 400μm thick.

The films (Type 1) prepared in Germany were DC-magnetron sputtered on uncooled substrates at ambient temperature with a sputter base pressure of 4.5×10^{-9} Torr and an Ar pressure of 2×10^{-3} Torr. Pt-Ru alloy films were fabricated by a co-sputtering method, and the composition of Pt-Ru was calculated from known deposition rates of each target and confirmed with XPS analysis. To achieve the desired film thickness, it was important to verify the deposition rate at a given sputtering power. The deposition rates of Pt and Pt-20 wt% Ru were very similar to each other. The deposition rates were about 25 nm/min at 150 W sputter power and about 8.3 nm/min at 50 W sputter power. Specific film compositions were prepared with various deposition rates by controlling the sputter power. All substrates were pre-cleaned with an ion gun to improve the adhesion between film and substrate. After film fabrication, the film thickness was about 200nm,

which was measured using a Tencor α-step profilometer [KLA-Tencor]. Certain samples were annealed at 800°C in N_2 atmosphere to cause microstructure changes.

Pt films (type 2 film) of 200nm thickness and 500nm thickness were deposited using an AJA International sputtering system at Lehigh University as shown in Figure 3.1.

Figure 3.1. AJA international sputtering system

The films were deposited at 350°C temperature in the DC-mode on Si wafer substrates. All substrates were pre-cleaned with the standard RCA cleaning procedure and heated at 400°C for 40 min before film deposition to reduce any negative moisture effect on adhesion between film and substrate. 30W power and 5×10^{-3} Torr Ar pressure were selected to produce the pure Pt films. To achieve the desired film thickness, the calibrated films were deposited on a dummy Si wafer with straight marker lines for a fixed time at a

given power. The wafer was then soaked in acetone with ultrasonic vibration, which dissolved the marker lines and lifted off the film resulting in steps in the deposited metal. After the lift off procedure, the height of the steps was measured using a Tencor α-step profiler [KLA-Tencor]. Several points over the wafer were selected to obtain an average film thickness. The film deposition rate was then calculated by dividing the average film thickness by the deposition time. The deposition rate of pure Pt was 4.2 nm/min at a sputtering power of 30W. All samples for the experiment and data analysis are listed in Table 4.1.

Table 3.1. Sample preparation conditions

Sputtering Conditions	Film	Sample name	Annealing conditions
Type 1	Pt	GS 35	800°C in N_2
Deposited at	1 wt% Ru	Pt-1 wt% Ru	atmosphere
room temperature	2 wt% Ru in Pt	Pt-2 wt% Ru	
	5 wt% Ru in Pt	Pt-5 wt% Ru	
	10 wt% Ru in Pt	Pt-10 wt% Ru	
	20 wt% Ru in Pt	Pt-20 wt% Ru	
Type 2	Pt 200nm thickness	GS 145	none
Deposited at 350°C	Pt 500nm thickness	GS 200	

3.2 Characterization

3.2.1 Composition Analysis

A Scienta ESCA-300 system equipped to perform X-ray photoelectron spectroscopy (XPS) was used to determine the composition of the Pt-Ru thin films. The Scienta ESCA-300 system uses a rotating anode that provides high resolution and excellent intensity of monochromatized X-rays [Gelius et al. 1990]. The XPS technique is based in the measurement of the energy distribution of electrons ejected from a material during X-ray bambardment. The kinetic energy (E_{KE}) of the ejected electron is related to incident a photon energy ($h\nu$) and binding energy (E_B) of a material. The relationship of these energy terms is expressed as

$$E_{KE} = h\nu - E_B \quad (3.1)$$

Since the $h\nu$ is known, E_B determines the E_{KE} of the electrons. The E_B provides the identification of an element. Due to the loss of energy in the inelastic scattering process, the x-ray only interacts at the surface of the material in the range between 2 to 15 atomic layers. XPS has an advantage over auger electron analysis (AES) because X-rays are less likely to damage surfaces than the electrons that are used for AES analysis.

The Scienta XPS system was equipped with an Ar ion gun. A short exposure to the Ar ion beam can remove surface contaminations such as carbon and oxygen. Thus, the composition analysis of Pt-Ru films was achieved following by the surface cleaning procedure. The system can detect 0.1 atomic % of Ru in Pt matrix. Approximately 1 by 1 cm coupons were prepared and an as-deposited Pt-20 wt% Ru film was used as a standard specimen for the composition analysis. The spot size of a beam is approximately 0.2 mm × 2 mm. The Ar ion gun can also be used for a depth profile analysis of the films.

The Ar ion gun can keep etching the surface of a specimen and then a spectrum acquired and used to detect the elements of the exposed surface through the film. The compositions before and after annealing of Pt-10wt%Ru film were examined with the depth-profile method of the instrument. Results are reported in Chapter 4.

3.2.2 Microstructural Characerization

3.2.2.1 Transmission Electron Microscopy (TEM)

All of the plan view TEM samples were prepared by chemically etching the substrate from the wafer backside. A small sample coupon (approximately 5 mm × 5 mm × 400μm) was cut, and then the thickness of the coupon was mechanically reduced using sandpaper manually. The ground coupon, approximately 100 μm thick, was then mounted film side down on a plastic plate (polypropylene stirring rod) with Krazy Glue and partially covered with a wax [Ackland], leaving a small area in the center uncoated for the chemical etching. The mounted sample was etched with a solution of HF, HNO_3, and CH_3HCOOH (3:5:3 ratio) [Kim 2001], creating a window of Pt or Pt-Ru films. The procedure for plan view TEM sample preparation is schematically shown in Figure 3.2. After creating the window, 1,2 Dichloro-ethane (CH_2ClCH_2Cl) was used to remove the wax on the backside of the specimen. The specimen was released from the plastic plate by soaking it in an acetone bath. The back-etched samples were then mounted on TEM copper grids using M-Bond adhesive and dried overnight at room temperature. Finally, the Precise Ion Polishing System (PIPS) was used to produce a thinner film so that it could be penetrated by the 200kV electron beam.

The microstructure of Pt and Pt-Ru films, as-deposited and annealed, was observed in plan view using a JEOL 2000FX transmission electron microscope. A 200kV electron beam was used for the observation. Grain morphology and grain size distribution of films were measured from the bright field images.

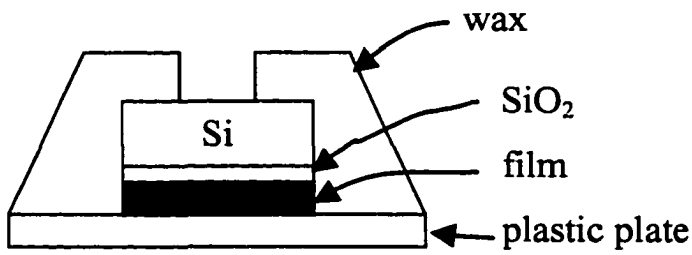

(a) Side view

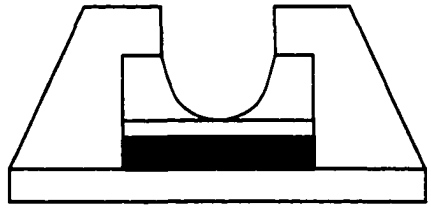

(b)

Figure 3.2. TEM specimen preparation. (a) The film side face down on a plastic plate and the sample is coated with wax. (b) Chemical solution, a combination of HF, HNO_3, and CH_3HCOOH is used to etch the Si from the back side.

Plan-view images were hand-traced to delineate the grain boundaries. Approximately 50 to 250 grains were used to measure average grain size of each film by hand-tracing method. The traced images were scanned, and then the digitized images were analyzed using a shareware software (NIH image) [Ristau 1998]. The average grain diameter was calculated based on the assumption of a circular grain shape, using

$$d = \sqrt{4A/\pi} \quad (3.2)$$

where d is diameter and A is grain area. The results of these measurement are listed in section 4.1

3.2.2.2 Scanning electron microscopy (SEM)

A JEOL XL 30 was used to see the surface morphology of annealed Pt and Pt-Ru thin films. The operating voltage of 20 KeV is selected to observe hillock formation on the surface of thin films with a vacuum mode. No special specimen preparation was necessary.

3.2.2.3 Focused Ion Beam (FIB)

Localized milling and deposition of conductors and insulators with high precision can be achieved from Focused Ion Beam (FIB) technology. Hence TEM sample preparation, device modifications, failure analysis and micromachining for MEMS (microelectromechanical system) are easily achieved from FIB technique [Reyntjens et al. 2001]. The structure of FIB is similar to SEM, but a gallium ion(Ga^+) beam is used instead of an electron beam. When incident ions(Ga^+) hit the surface of a sample, sputtering of natural and ionized atoms, and electron emission occurs. For imaging, a low current beam is used to scan a sample, and secondary ions and electrons are generated from the sample. Since secondary electron emission rate depends on the crystalline orientation of the sample, individual grain contrast can be achieved with the FIB technique. Specimen cutting is obtained using a high ion beam current resulting in a physical sputtering of the sample. A micromachining procedure enables TEM cross-section specimen preparation. The TEM sample preparation is shown in Figure 3.3.

(a) amorphous layer Pt deposition

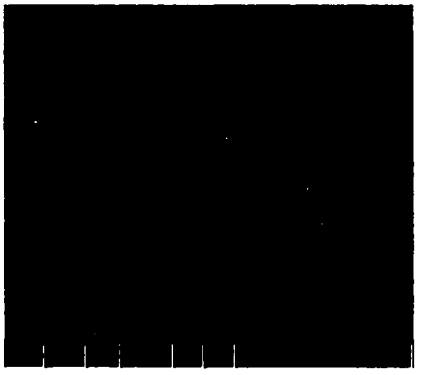

(b) fast milling

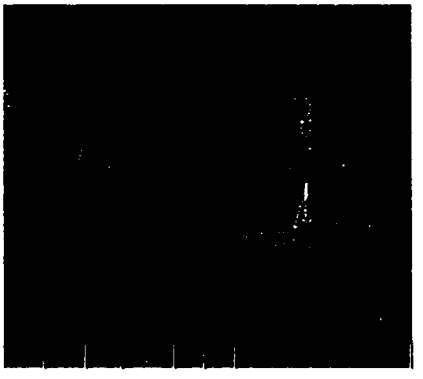

(c) fast milling both side.

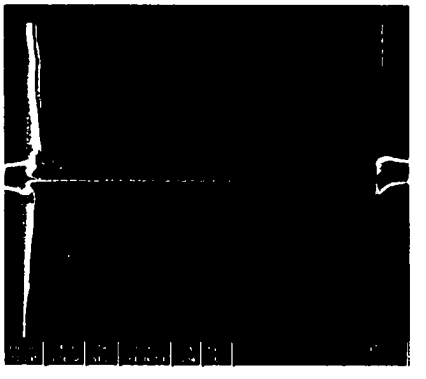

(d) slow milling, polish the wall

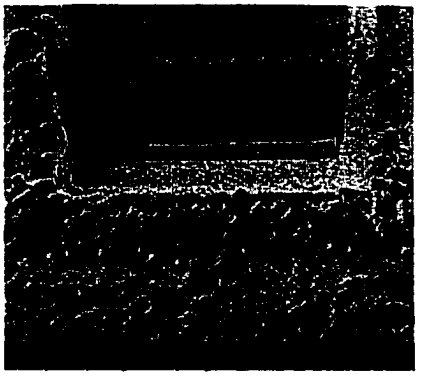

(e) sample cutting

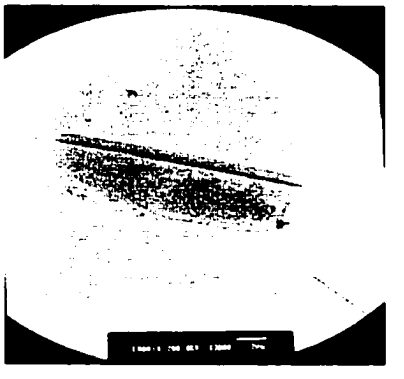

(f) cross-section TEM specimen

Figure 3.3. FIB cross-section TEM sample preparation (Hyoungjoon Park at Lehigh University).

A protection layer, amorphous Pt coating, is deposited on the specimen (a), and material is removed with a rough and fast milling (b) and (c). Precise milling is used to polish the side-wall (d). Finally, the polished wall is cut and the cross section sample is ready for TEM observation (e) and (f). Annealed pure Pt cross-section TEM specimen was prepared for this procedure with a Focused Ion Beam instrument (Fei XP dual beam workstation). The TEM image of the specimen was taken using a JEOL 2000 transmission electron microscope. Cross-section and plain view images of samples GS 150 and GS 200 were acquired with the instrument to examine the grain morphology. The high power of Ga ions was used to cut the film and a low power ion beam was used for imaging with high grain contrast.

3.2.2.4 X-ray Diffraction

X-ray diffraction was used to determine preferred crystalline orientation of the Pt and Pt-Ru thin films according to different fabrication conditions of the as-deposited and annealed films. A Rigaku X-ray diffractometer system with monochromatic CuK_{α} radiation (λ=1.541Å) was used to perform θ-2θ (Bragg-Brentano) scans. For these measurements, 2θ was scanned from 20° to 80° in 800 sec with beam energy of 50eV and 100mA. Results are presented in section 4.1.3.

3.3 Mechanical test

3.3.1. Wafer curvature technique

The stress in the Pt and Pt-Ru films was measured by the wafer curvature method.

The equipment for the wafer curvature measurement is a laser system built at Stanford University, first developed by Flinn [Flinn et al. 1987]. A schematic diagram of the apparatus is shown in Figure 3.4.

Curvature is obtained by scanning the film surface with a laser beam and determining the angle of reflection. The laser beam is reflected from the wafer at an angle. A curved wafer provides a different angle of the reflecting beam while the wafer is scanned. A laser beam scans across the wafer through a lens with a rotating mirror. The rotating mirror is located at the focus of the lens, so the incident laser beam can reach the sample through the lens, which is perpendicular with a laser beam. If the surface of the wafer is flat, the laser beam is reflected to one point on a position sensitive photodiode. The photodiode is used to measure the displacements of the reflected laser beam in the case of the curved wafer. The curvature of the wafer is related to the displacement of the reflected spots in the focal plane. The sample sits on a tripod of thermocouples in a high temperature furnace. So, the exact temperature of the wafer can be determined during measurement. Atmosphere is controlled by continuously flowing N_2 gas, and desired oxygen level of atmosphere in the furnace can be checked with an oxygen sensor before and during the stress measurement. A fast cooling rate can be obtained by controlling the gas flow rates in the furnace.

The wafer curvature was measured while the sample, a 3 inch wafer, was enclosed in a convection furnace in N_2 atmosphere. To remove the effects of any inherent curvature in the thermally oxidized Si wafer, the curvature of the wafer was measured prior to Pt and Pt-Ru film deposition, and then the previous curvature was subtracted from every measurement of the film/substrate combination. Heating and cooling rates of

12°C /min were used for temperature cycling up to 800°C which covers the temperature range for ferroelectric fabrication (450-800°C). The slow cooling rates are observed below 200°C due to the limitation of a cooling method, liquid N_2.

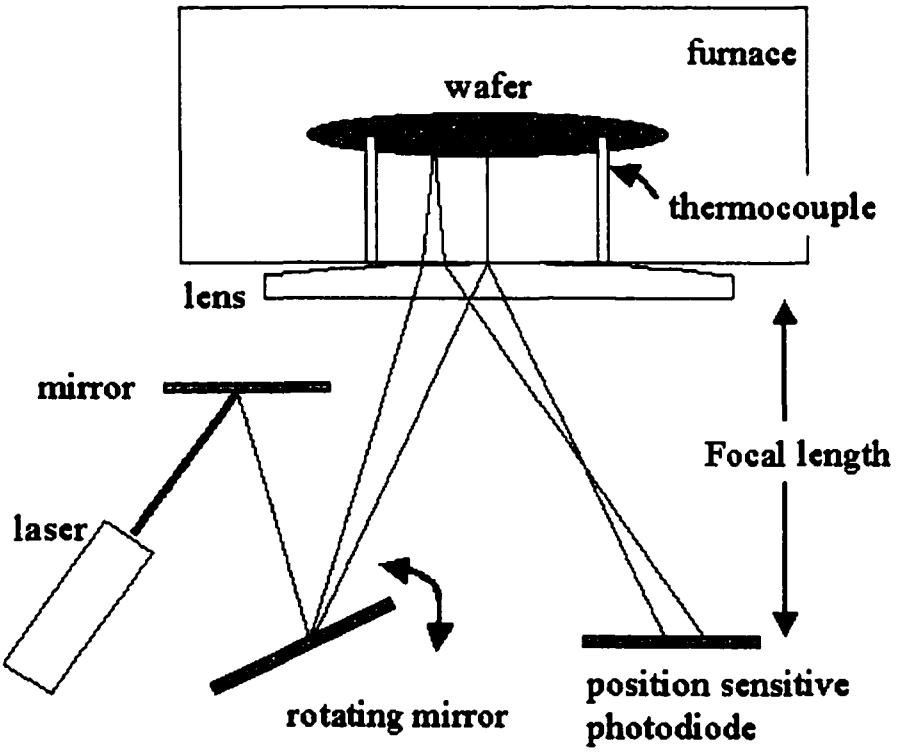

Figure 3.4. A schematic diagram of a wafer curvature measurement system.

3.3.2 Nanoindentation method

Depth-sensing indentation using a Hysitron Triboscope was used to measure the mechanical behaviors of the Pt and Pt-Ru thin films. The Triboscope is capable of operating at a load range of 1μN to 10mN with 100nN sensitivity and at a displacement range of 5μm full scale with 0.2 nm sensitivity. A diamond tip (Berkovich, tip

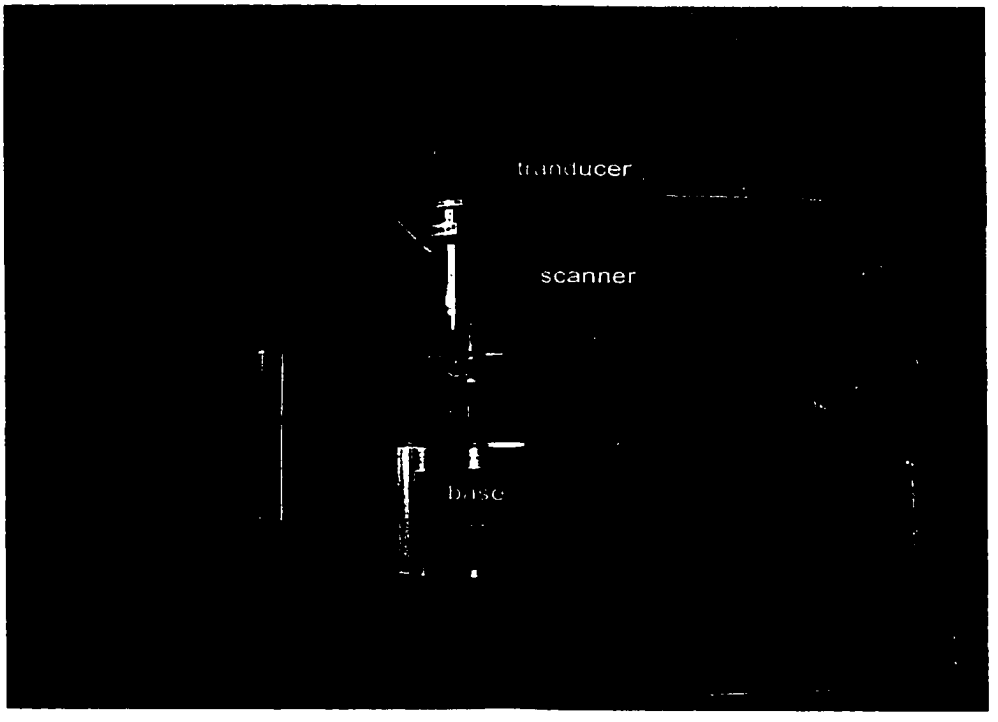

(a) Nanoindentation instrument

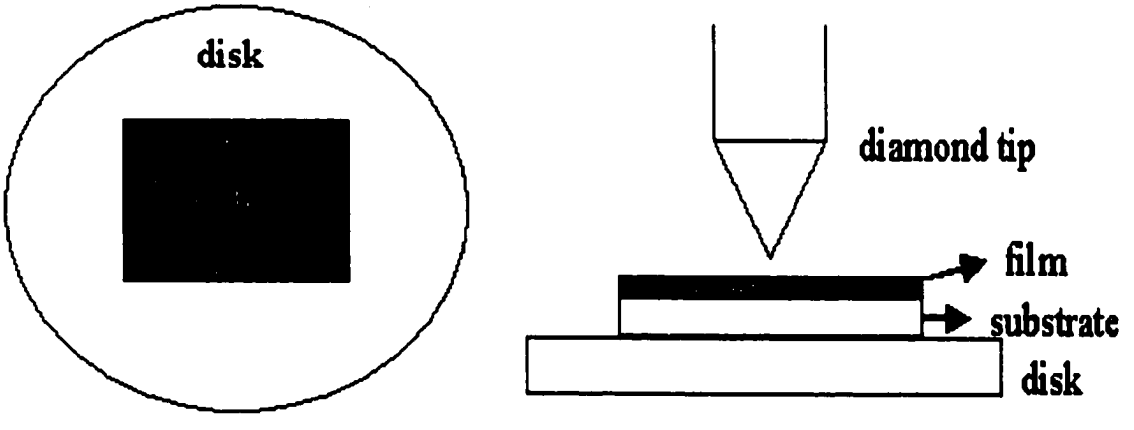

(b) top view of sample mounted on disk (c) side view of sample in the instrument

Figure 3.5. Nanoindentation instrument. Sample is mounted on an AFM scanner that is placed under the nanoindenation tranducer equipped with a diamond tip.

Ch. 4 Microstructure development of Pt and Pt-Ru films

In this chapter, the as-deposited microstructure of the Pt and Pt-Ru thin films is studied according to thin film fabrication conditions. Also, evolution of microstructure is examined in terms of Pt-Ru composition, deposition conditions and annealing conditions. The features of primary interest in the microstructure study are the average grain size and crystallographic orientation of the films. Well-characterized microstructure information is important for the interpretation of the mechanical behavior of films. For instance, large or small-grains influence a hardening mechanism such as that described by the Hall-Petch relationship and can also change creep behavior at high temperature. Texture also provides useful information to understand the elastic behavior of films. Microstructure characterizations including grain size and preferred crystalline orientation of Pt and Pt-Ru thin films are described in this chapter. Hillock formation on Pt and Pt-Ru films after certain annealing conditions is also examined to understand the hillocking mechanism.

4.1 Microstructure

4.1.1 TEM images and grain size analysis

4.1.1.1 Solid solution alloy films

Grain size analyses were performed with TEM (Transmission Electron Microscopy) as described in Chapter 3. The microstructures of the as-deposited and annealed films (type 1) were examined to observe the extent of any solid solution alloy effect on grain size. Figures 4.1 and 4.2 show TEM images of as-deposited and annealed films.

(a) Pt as-deposited film

(b) Pt-5wt%Ru as-deposited film

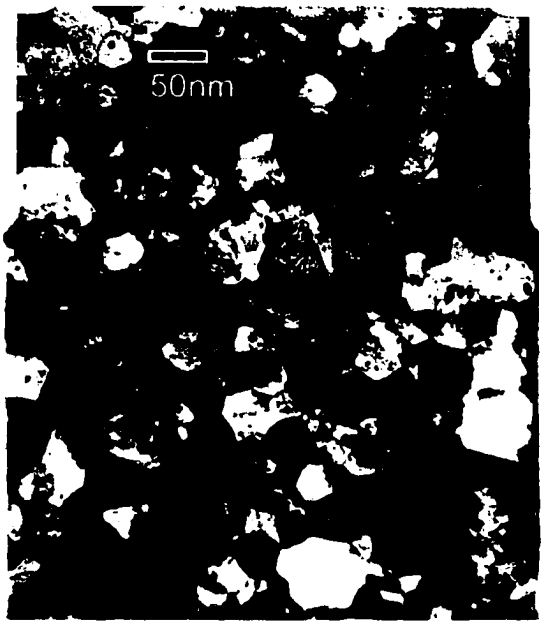

(c) Pt-10wt%Ru as-deposited film

Figure 4.1. TEM images of as-deposited films (type 1).

Figure 4.3 shows the measured average grain sizes of the films. The grain sizes of the as-deposited films, which are all around 35 nm, are not dependent on Ru content. However, the grain sizes of the annealed films decrease with an increase in the amount of Ru. The average grain size of the pure Pt film is 103nm, while that of a Pt-10% Ru film is only 56 nm, as shown in Figure 4.3. This behavior can most likely be explained by the drag effect of solute atoms on grain boundary motion. However, from these observations it cannot be determined if the measured grain sizes are the maximum possible for each composition or if they simply indicate significant differences in growth rate.

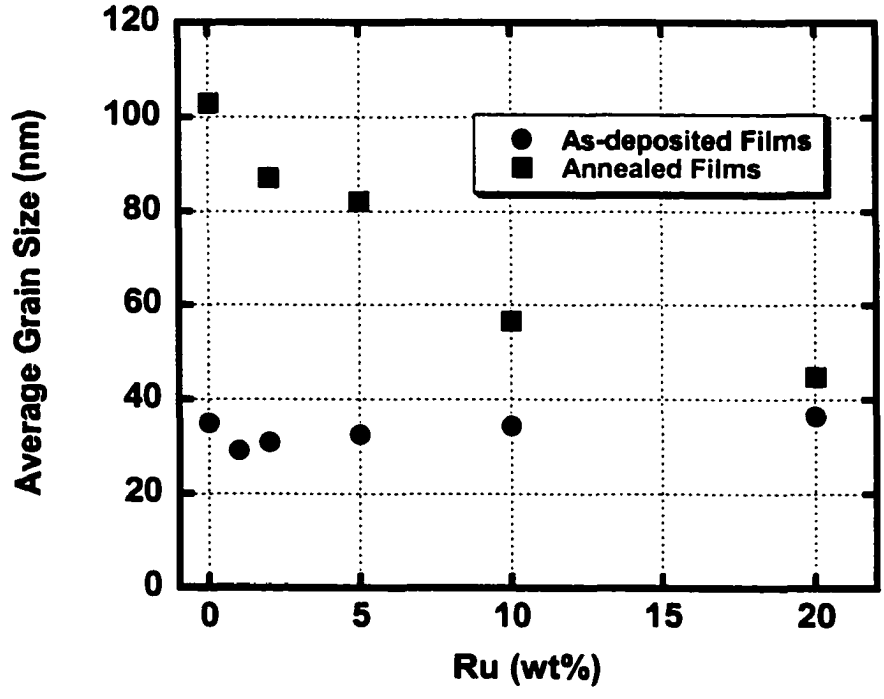

Figure 4.3. Average grain size of Pt and Pt-Ru thin films (type 1).

4.1.1.2 Pt films with different fabrication conditions

The average grain sizes of type 1 (GS 35) and type 2 (GS 145 and GS 200) pure Pt films were determined to be 35nm, 145 nm and 200 nm, respectively. Deposition conditions of type 1 and type 2 films are described in Chapter 3. The TEM images of these three films are shown in Figures 4.4. The TEM images were taken at different magnifications to keep the number of grains in each image approximately the same. High deposition temperature and thick film [long deposition time] (GS 200, which is 500 nm thick and deposited at 350°C) produce bigger average grain size than GS 35 and GS 145. Structure zone models that are based on the substrate temperature can predict the microstructure development during deposition [Chapter 2].

The dislocation density in the image of GS 35 appears to be lower than that of GS 145 and GS 200. However, the observation of low dislocation density in GS 35 might be caused by the loss of dislocation lines during the TEM specimen preparation of GS 35. To avoid overlapping grain boundaries in the images, a thinner specimen was prepared for the small-grained GS 35 compared to the ones of GS 145 and GS 200. Grain size distributions of 3 Pt films (GS35, GS145 and GS200) were characterized by using a lognormal distribution [Zielinski 1995, Tao 2002] as shown in Figure 4.5. Standard deviations of three films are 10.6 nm, 48 nm and 63 nm for GS 35, GS 145 and GS 200. There is very little overlap between the distribution of GS 35 and the others.

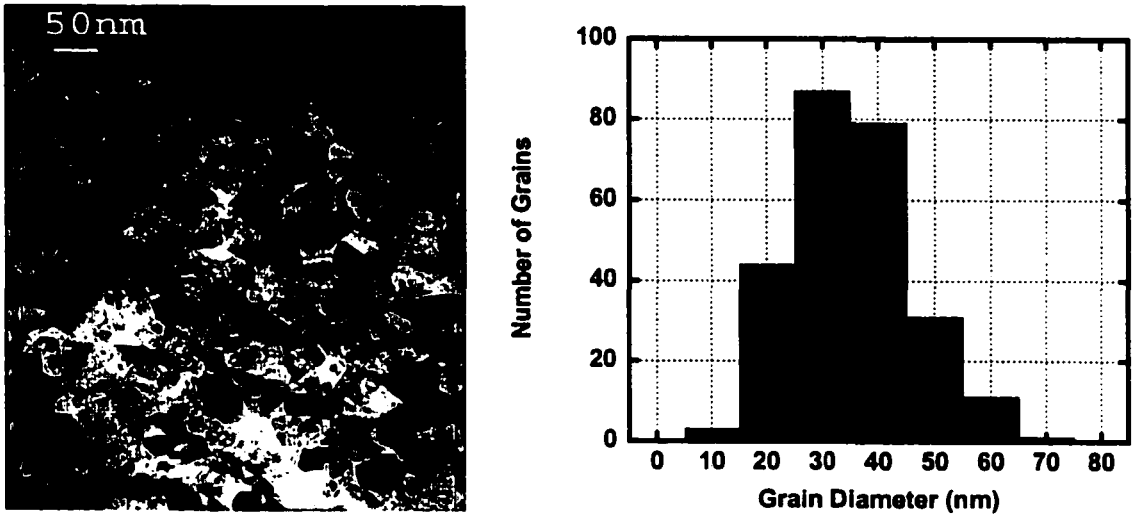

(a) Pt as-deposit film (GS 35)

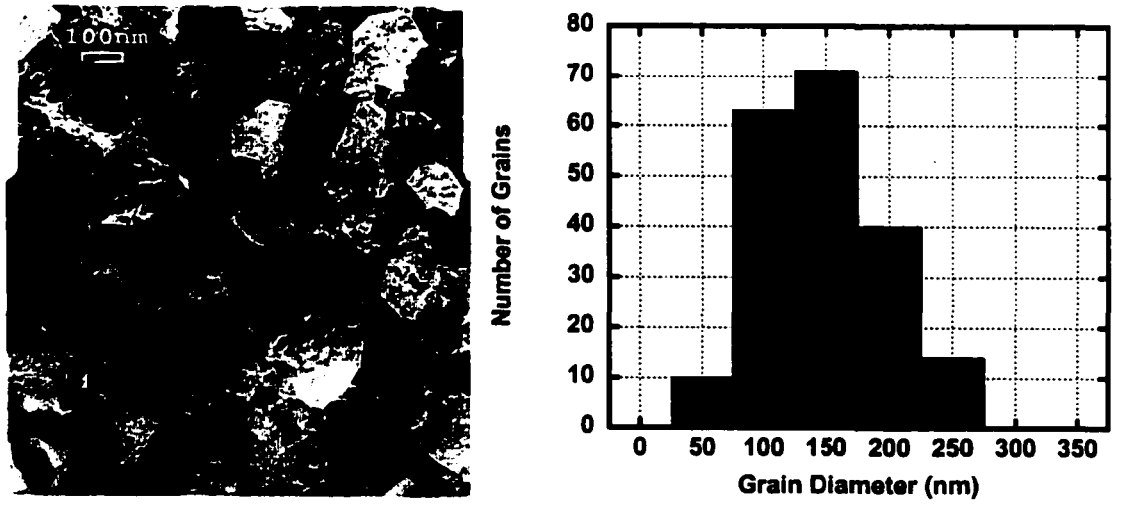

(b) Pt as-deposit film (GS 145)

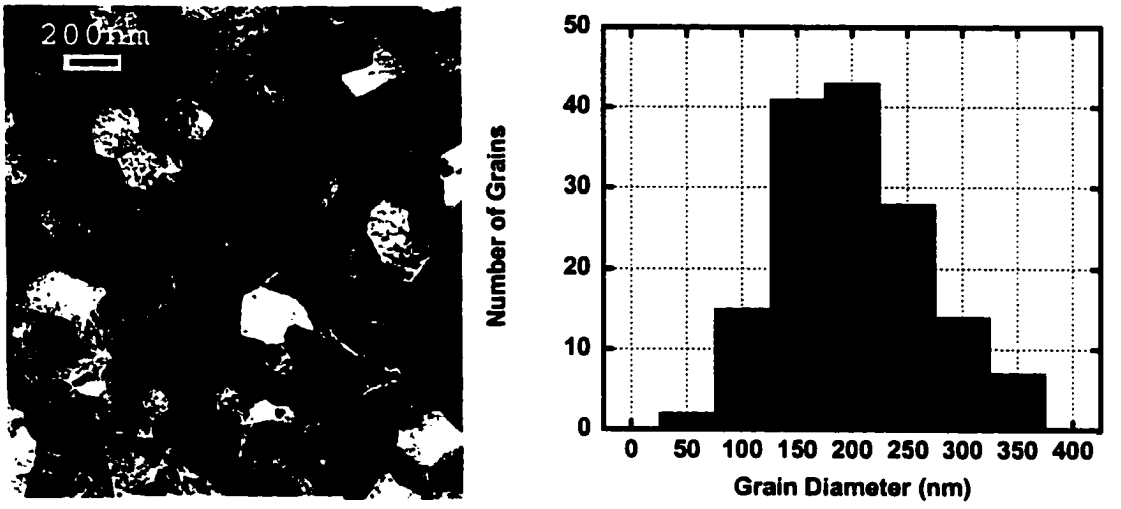

(c) Pt as-deposited film (GS 200)

Figure 4.4. TEM Images and grain size distribution curves of Pt films. The average grain diameters of GS 35 (type 1), GS 145 and GS 200 (type 2) are 35 nm, 145 nm and 200 nm. The magnifications of three TEM images are different to contain same number of grains

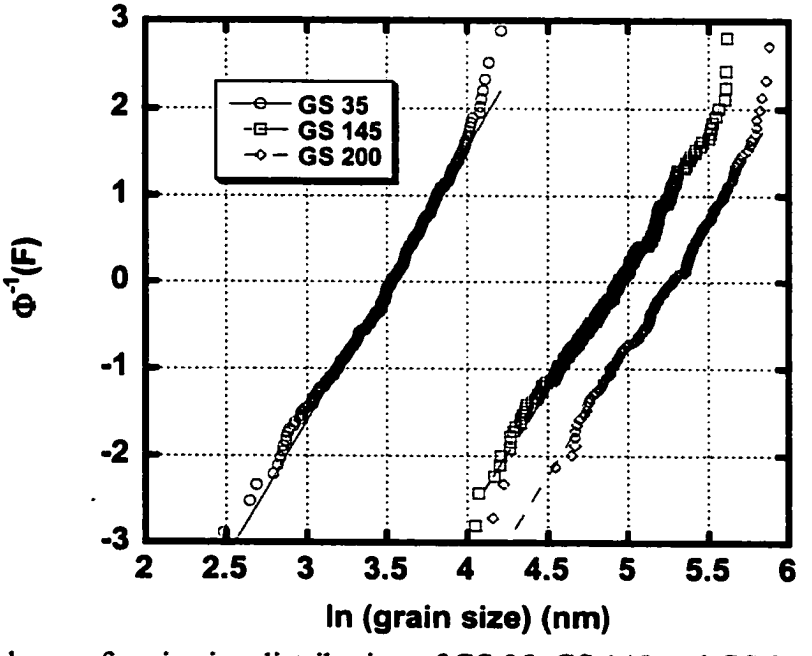

Figure 4.5. Analyses of grain size distribution of GS 35, GS 145 and GS 200. Average grain sizes of GS 35, GS 145 and GS 200 are 35nm, 145nm and 200nm respectively. Standard deviations of three films are 10.60nm, 48nm and 63nm for GS 35, GS 145 and GS 200.

4.1.2 Focused Ion Beam images

FIB images of two of the pure Pt films (GS 145 and GS 200) are shown in Figure 4.6. Plain view images were obtained by using a low power Ga ion beam on the surface of each film for a short time to see grain contrast corresponding to different grain orientations. The cross-section of the film was obtained by using a high power Ga ion beam to cut the film and a low power ion beam to see the image of the film. The average grain size is similar to the film thickness and a fully columnar structure is observed in the GS 145 image. However, a semi-columnar structure is observed on the GS 200 image with the film 1-2 grains thick in most observed locations. GS 35 could not be clearly imaged because of the nano-sized grain structure.

4.1.3 X-ray diffraction measurement

Figures 4.7 and 4.8 show symmetric X-ray scans of the Pt and Pt-Ru films before and after thermal cycling. All scans show a strong (111) orientation peak. Pt films deposited at 350°C (type 2, GS 145 and GS 200) also show a strong (111) orientation peak as shown in Figure 4.9.

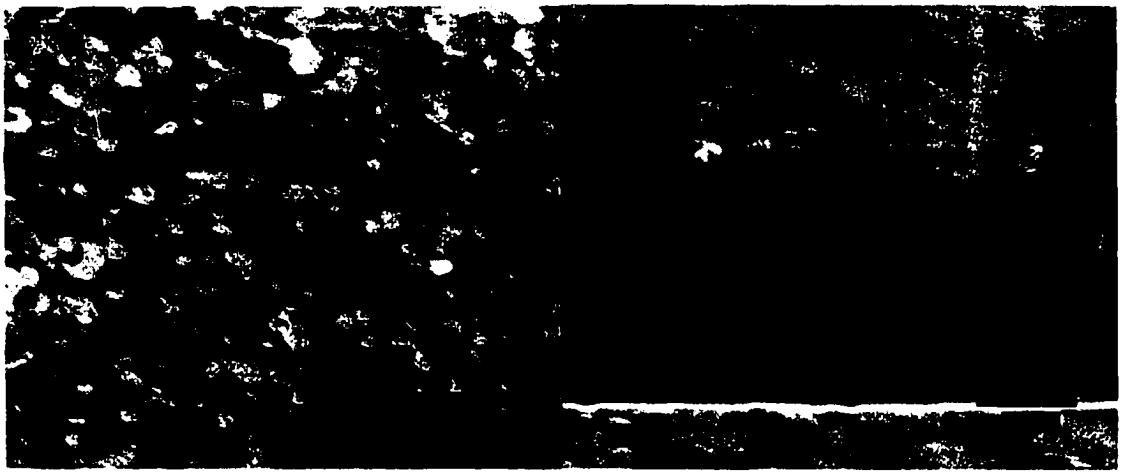

(a) plan view and cross-section images of 200nm thick Pt

(b) plan view and cross-section images of 500nm thick Pt

Figure 4.6. FIB images of as-deposited Pt films. Films were deposited at 350°C. Short exposure to high power Ga ion cut the films and low current of Ga ion beam was used to observe the images (a) 200 nm thick Pt (b) 500 nm thick Pt. Grains in (a) are similar to the film thickness , but grains in (b) are smaller than the film thickness.

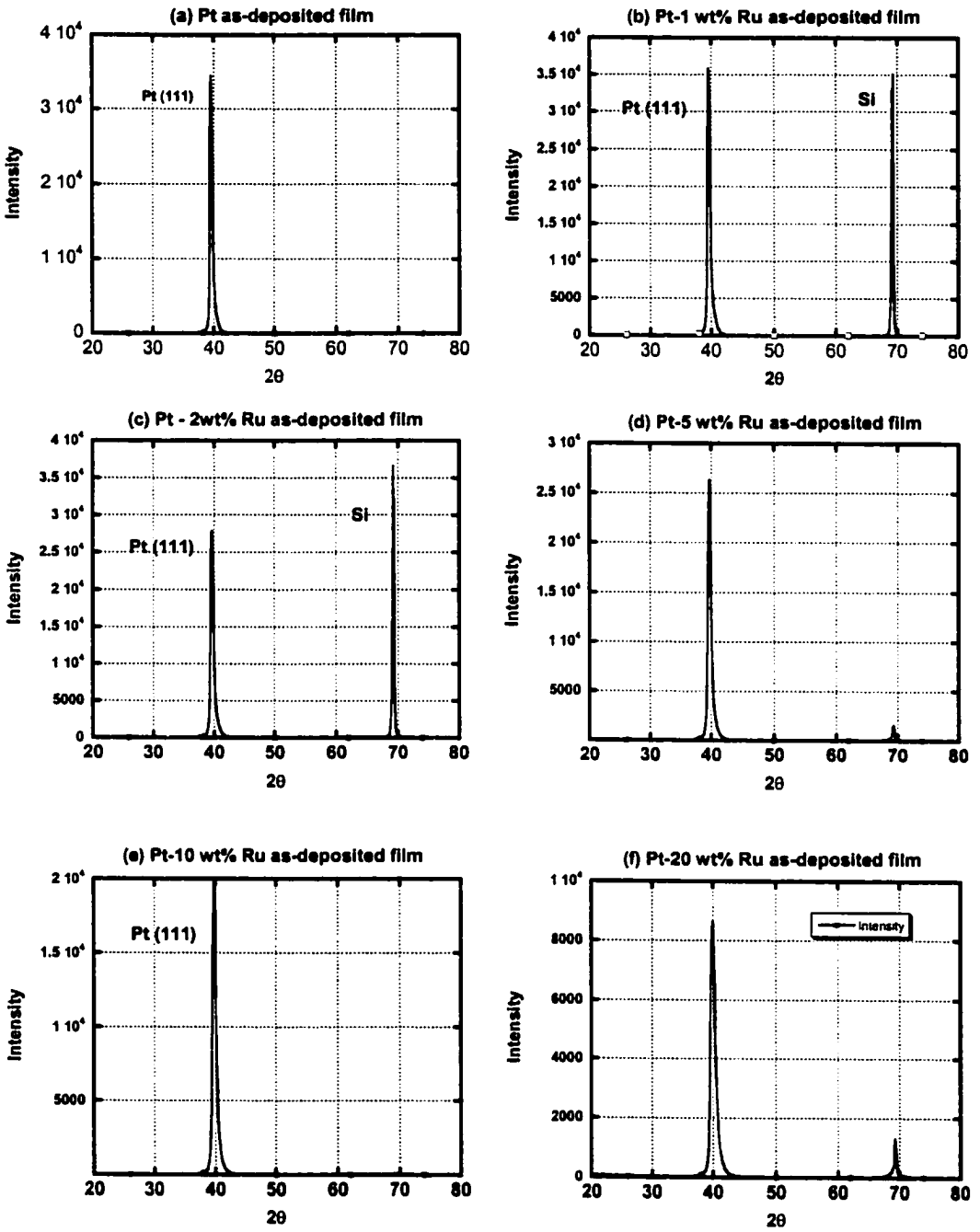

Figure 4.7. X-ray 2θ scan of as-deposited Pt and Pt-Ru films. (a) Pt film (b) Pt-1wt%Ru film (c) Pt-2wt%Ru film (d) Pt-5wt%Ru film (e) Pt-10wt%Ru film (f) Pt-20wt%Ru film

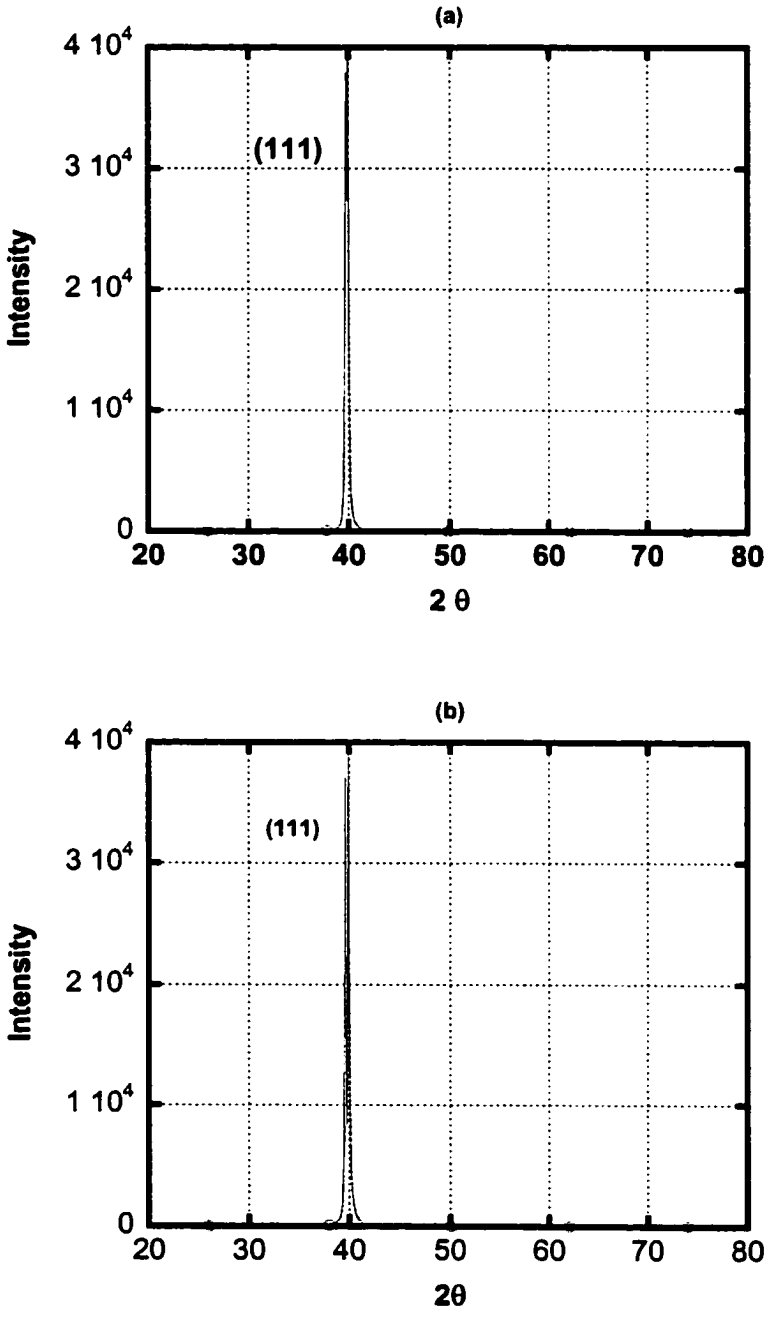

Figure 4.9. XRD 2θ scan of two Pt films(type 2); (a) GS 145 (b) GS 200. All three x-ray diffraction data show strong (111) orientation of Pt film.

4.1.4. XPS analysis

The compositions of the Pt-Ru films (type 1) were verified by the XPS method. Although a careful co-sputtering method was used to fabricate the films, the compositions of as-deposited and thermocycled Pt-Ru films had to be verified. To remove C and O on the surface, Ar ion sputtering was first used to clean the surface of the films. Compositions according to Ru addition are shown in Table 4.1.

Table 4.1. Composition analysis of as-deposited Pt-Ru films

Sample	Ru Concentration (wt %)
Pt- 20 wt% Ru	20
Pt-10 wt% Ru	10
Pt-5 wt% Ru	4.7
Pt-2 wt% Ru	1.9
Pt-1 wt% Ru	1.1

As seen in the Table, the Ru concentration was similar to the predicted Ru content from co-sputtering deposition.

In order to confirm Ru composition through the film depth, XPS depth profiles of as-deposited and thermocycled Pt-10 wt% Ru were characterized by using *in situ* Ar ion sputtering. The composition gradient after thermal cycling is examined by this method. The peak count as a function of sputtering time for a Pt-10wt%Ru thin film is shown in figure 4.10. The Ru/Pt peak ratios are consistent for both sets of measurements. As the sputtering time increased to 40-60 minutes, the peak counts of Pt and Ru decreased because the XPS beam was detecting the substrate material.

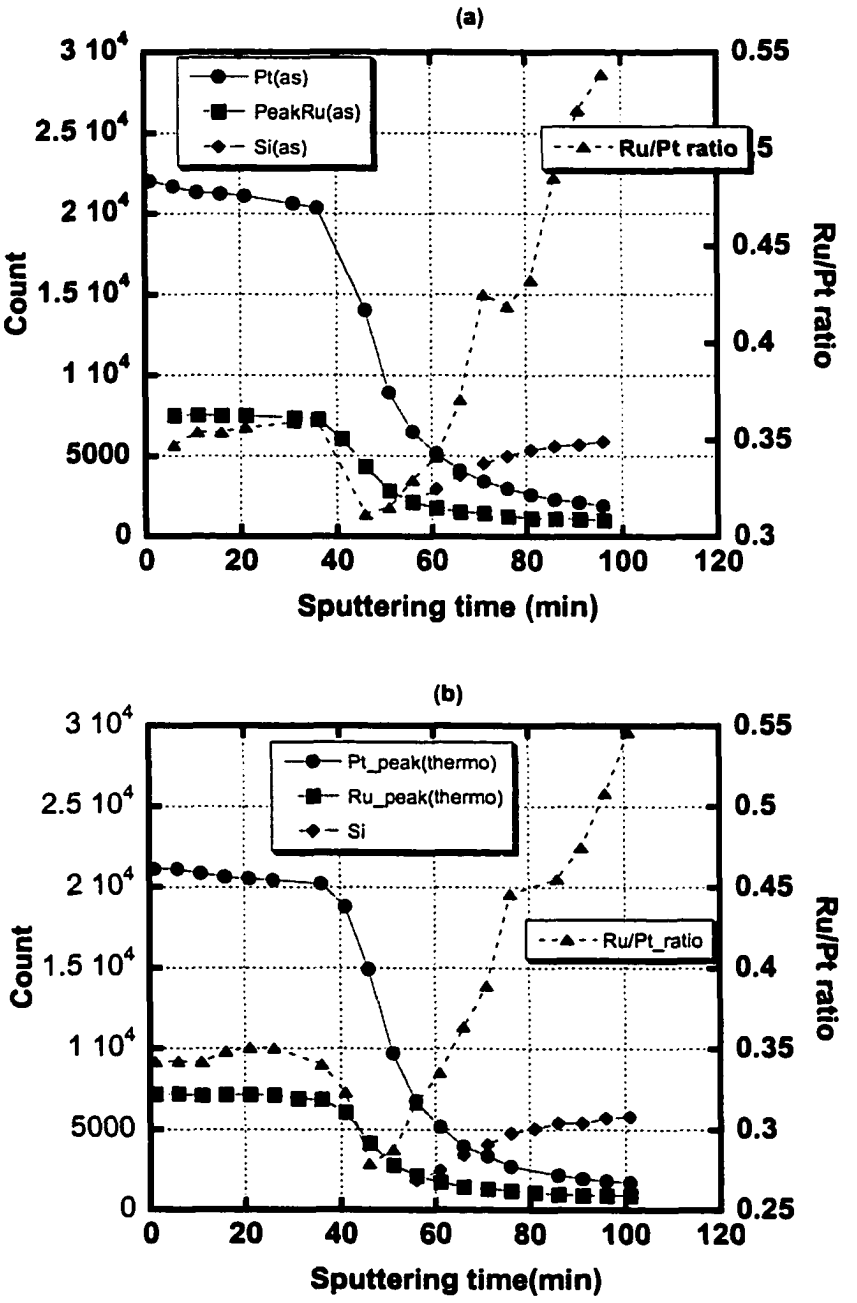

Figure 4.10. XPS depth profile. Pt and Ru count peaks according to sputtering time is presented to compare the ratio of Ru/Pt through Pt-10 wt% Ru films. (a) as-deposited Pt-10 wt% Ru film and (b) thermocycled Pt-10 wt% Ru film.

Figure 4.11 shows the composition of Ru through as-deposited and thermocycled film. The composition of Pt-10 wt% Ru film is fairly consistent through the film thickness, and no composition change is observed after thermocycling. Figure 4.12 shows the Ru peaks of the as-deposited and thermocycled Pt-10wt% Ru film before Ar ion sputtering procedure. At the surface of the thermocycled film, RuO_2 was detected whereas no Ru oxide form was observed on the as-deposited film. Table 4.2 shows the binding energy of Ru and Ru oxide, and RuO_2. Binding energy of Ru and RuO_2 are observed in Figure 4.12 (b).

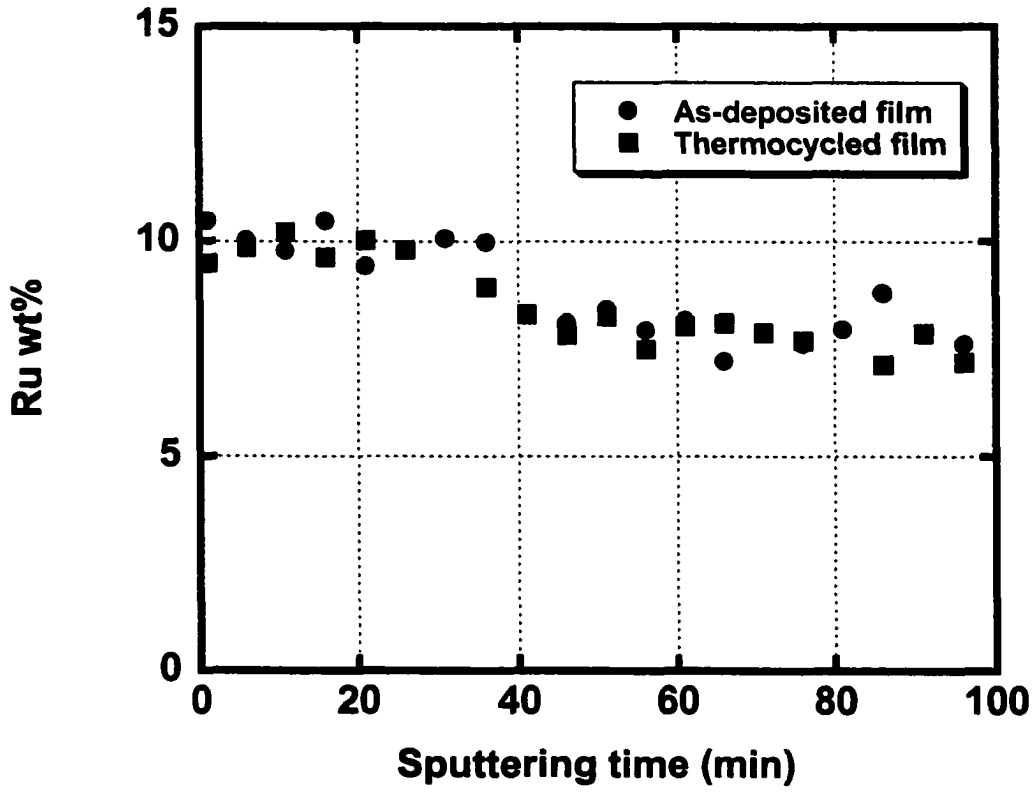

Figure 4.11. Composition analysis of as-deposited and thermocycled Pt-10 wt% Ru films Ru contents in Pt films are consistent through the film, and similar composition results are obtained from as-deposited and thermocycled films.

Table 4.2 Ru binding energy.

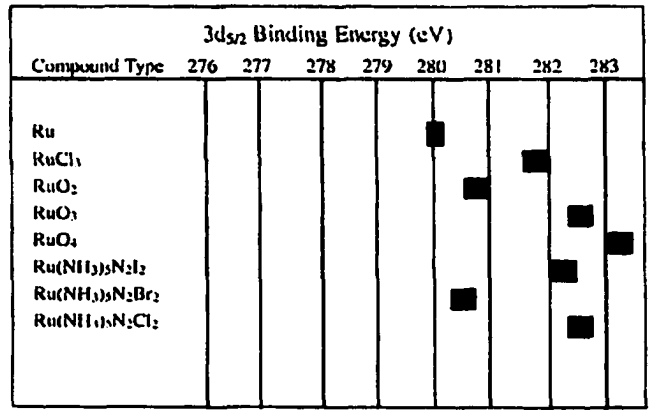

4.2 Hillock formation on Pt and Pt-Ru films

4.2.1 Hillocking of metal films

For microelectronics applications, reliability of device is one of the most important issues. The development of voids and hillocks in metal lines is a commonly observed failure mechanism. The formation of hillocks in metal films is believed to be the result of the relaxation of compressive stress that develops during fabrication. The hillocks are detrimental to integrated circuit structure because they can lead to electrical short circuits [Tu et al. 1992]. In this section, results on the formation of hillocks in Pt and Pt-Ru films were observed and possible mechanisms related to hillock formation are discussed.

Two types of hillock formation have been observed in metallic thin films, called growth hillocks and annealing hillocks. Growth hillocks are defined as hillocks that form during thin film deposition whereas annealing hillocks are classified as heat cycling assisted hillock formations after deposition. Intrinsic compressive stresses that are

generated during deposition are responsible for growth hillock formation. The relaxation of compressive stress during thermal cycling causes annealing hillock formation. many metal films such as lead, aluminum and alloys have shown hillock formation after thermal cycling [Lahiri 1970, Kim et al. 2000, Iwamura 1995].

Several factors including the presence of a passivation layer on the films, grain boundary structure, texture, grain boundary diffusion and grain boundary sliding affect hillock formation in metal films. A passivation overlayer on the metal film plays an important role on hillock formation. In the case of a thick passivation layer, the layer prevents hillock formation by suppressing the diffusive flow of atoms from the interior of film to surface [Dell'oca 1971]. However, a thin passivation layer contributes to create hillock formation because atoms can diffuse to the surface through the weak part of passivation layer to relax large compressive stress [Chang et al. 1993]. The same mechanism has been observed on unpassivated Al thin film due to the native oxide that forms on the surface. Based on this mechanism, hillock formation is not expected on truly bare metal films.

Grain boundary structure and texture in films may change the hillock formation. Even if a uniform strain is applied to a thin film, the yield stresses of grains with different grain orientations result in the development of different stress levels [Sanchez et al. 1992, Nowell 1998]. If the grains with different orientations support different stresses, a local stress gradient will be established. Thus, localized relaxation occurs. The texture strength may be responsible for inhomogeneous hillock distributions. A high yield stress is expected for grains of (111) orientation in FCC metal films, so hillock forms on grains with non-(111) orientation. Grains with boundaries characterized by high angle rotations

are also considered as preferred locations for hillock formation [Nowell 1998]. Grain boundary diffusion also affects hillock formation [Iwamura 1995, Ericson et al. 1991, Genin 1995]. Hillock growth at grain boundary triple junctions suggests a grain boundary diffusion mechanism. Adding a small amount of alloy element could reduce the occurrence hillocks by reducing diffusion through the grain boundary [Bhatt 1971].

Finally, grain boundary sliding is also one of the possible hillock formation mechanisms in metal films. Adhesion between film and substrate is critical to avoiding hillocks because a stress can cause a protrusion of the grain above the surface, leaving a void at the film/substrate interface [Ronay et al. 1980]. Lahiri [Lahiri 1975] compared hillock formations in two different types of lead films to show the grain boundary sliding mechanism. Hillock growth related to the stress-relaxation phenomenon in non-epitaxial lead films was explained as grain boundary sliding and diffusion creep mechanisms. Non-hillock formation in epitaxial lead films after thermal cycling suggested that grain boundary sliding is a key mechanism of hillock growth. Chaudhari [Chaudhari 1974] also displayed interface effects by depositing an Ni underlayer below lead films on one-half of his substrates. The high hillock density in regions with no Ni underlayer, which correspond to poor adhesion, suggested that the interface quality affects hillock formation.

4.2.2 Previous observation of Pt hillock formation

Hillock formations on Pt films have been reported according to various processing conditions such as deposition temperature and annealing ambients. The large thermal expansion difference of Pt ($9x10^{-6}/^{o}C$) and Si ($3x10^{-6}/^{o}C$) causes compressive

stress in the Pt at elevated temperatures. The film relieves some of this large compressive stress by forming hillocks. Matsui and Eichorst showed that compressive stress affects hillock formation according to Pt deposition temperature [Matsui et al 1998, Eichorst 1994]. Lee also observed this result and found Pt pinholes, which are induced by tensile stress, at very high deposition temperature [Lee et al. 1995]. However, Pt hillock formations are not only explained by the compressive stress factor. Hren showed that the annealing atmosphere had an important effect on the generation of hillocks [Hren et al.1992]. A Pt film on a SiO_2/Si substrate annealed in air showed a high density of hillocks, but the one annealed in vacuum showed no hillock formation.

4.2.3 Results

In our study, no growth hillocks were observed under any conditions. Although high residual compressive stresses were measured with the wafer curvature method, the stresses induced from deposition may not be large enough to produce growth hillocks at the temperature range to which the films were exposed. However, hillocks often formed on certain films after annealing at 800°C under N_2 atmosphere. Hillock formation on 200nm thick Pt and Pt-Ru films are shown in Figure 4.13. After heating, hillocks were observed on Pt and Pt-2wt% Ru films, but no visible hillocks were detected on Pt-20 wt% Ru film despite the same annealing condition. Figure 4.14 shows FIB images of hillock formation on Pt and Pt-2 wt% Ru films. In these micrographs, buckling type hillocks are observed. The hillocked films were debonded from the substrate resulting in voids between the film and the substrate. All hillocks are a circular shape from the top view and

the diameters are in the range of 0.5 to 2 μm. The buckling diameter is larger than the film thickness.

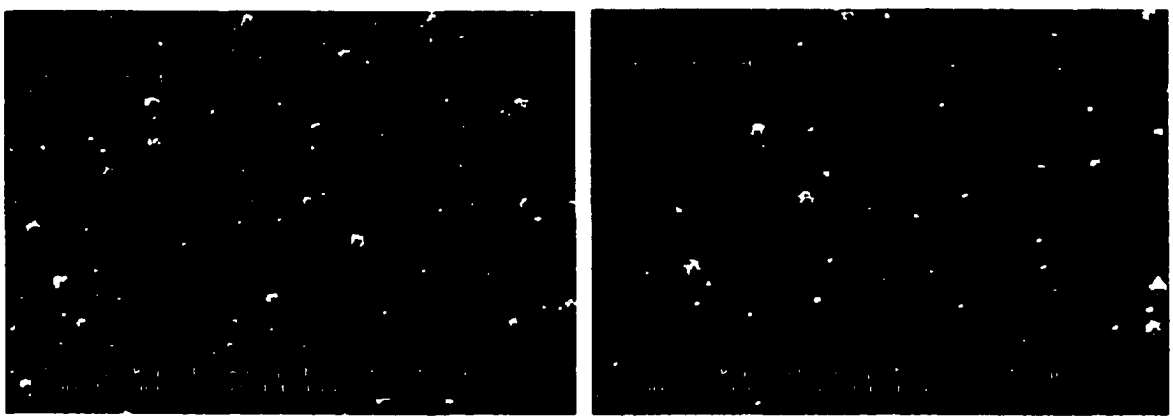

(a) annealed Pt film

(b) annealed Pt-2 wt% Ru film

(c) annealed Pt-20 wt% Ru film

Figure 4.13. SEM Images of Annealed Pt and Pt-Ru Thin Films (200nm thick film, annealed at N_2 atmosphere, heating and cooling rate is 5°C/min)
(a)Pt film (b)Pt –2 wt% Ru film, (c) Pt – 20wt% Ru film

(a) annealed Pt film (b) annealed Pt-2 wt% Ru

Figure 4.14. FIB images of hillocks. Ga ion beam were used to cut the film, and void were observed below the hillock area.

Pt film was annealed several times up to 800°C at N_2 atmosphere. After several thermocyclings, large hillocks form on the surface of the Pt film. Figure 4.15 shows FIB images of hillocks on the Pt film. Hillock formation on the Pt film also shows buckling type hillock as shown in Figure 4.14. Several grains are included to form a hillock. A hole is often observed on the buckled hillock surface (c). This hole can be produced to relieve the stress since several thermocyclings introduce the tensile stress at the surface of the hillock film.

Figure 4.16 shows an SEM image of the annealed Pt film at a vacuum atmosphere. The vacuum annealed Pt film did not form the large hillocks found on the N_2 annealed Pt as shown in Figure 4.13 (a).

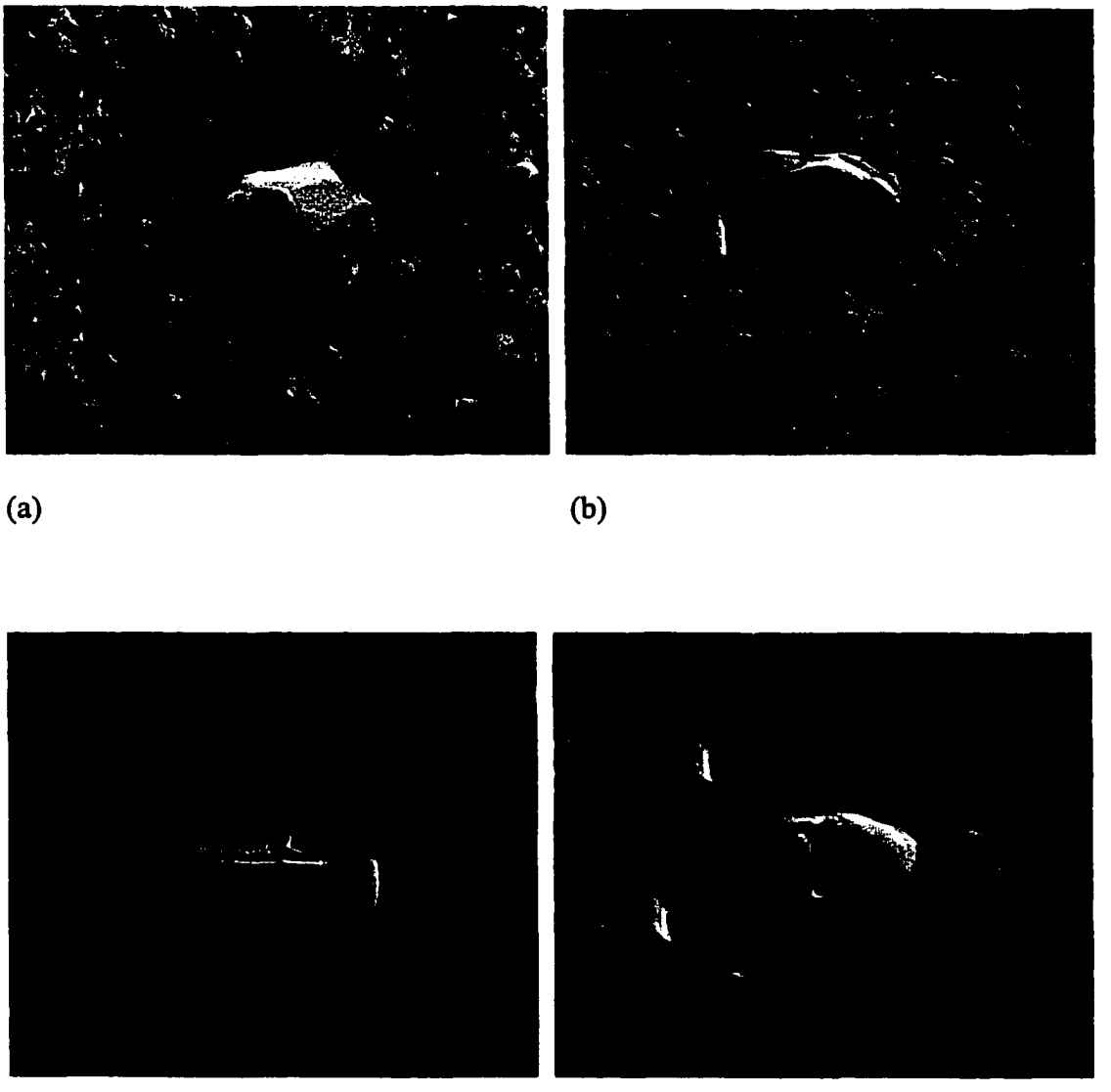

Figure 4.15. FIB images of a Pt film that are thermocycled several times. (a) hillock is composed of several grains. (b) cross-section image of (a), void forms below delaminated film. (c) hole form on a hillock. (c) cross-section image of (c).

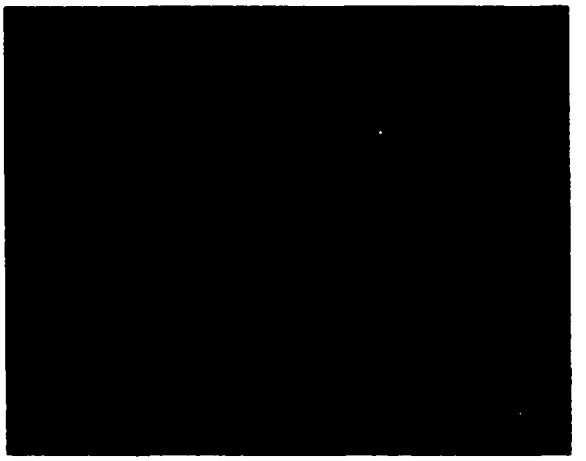

Figure 4.16. An SEM image of a Pt film shows no visible hillock formation. The film was annealed at 800°C, vacuum atmosphere. Buckling type of hillock formation was not observed on the vacuum annealed Pt film.

4.2.4 Discussion

The observation of the film surfaces reveals that hillock formation depends on annealing atmosphere and composition. Hillocks display a buckling type delaminating area and a void is produced at the film/substrate interface. Cross-section FIB images of Pt film do not support a grain boundary diffusion hillock growth mechanism. This mechanism relies on material transport along diffusion path such as grain boundaries. However, hillocks formed on films show the delamination between the film and the substrate, and hillocks are composed of several grains. No large material accumulation due to material transport in hillock area is observed. The diffusion mechanism may therefore not be primary responsible for the hillock formations. The diffusion hillock of Al film is shown in Figure 4.17. The hillock area has large accumulation of Al materials

without the delamination area. This shows a clear difference between Pt hillocks and Al hillocks.

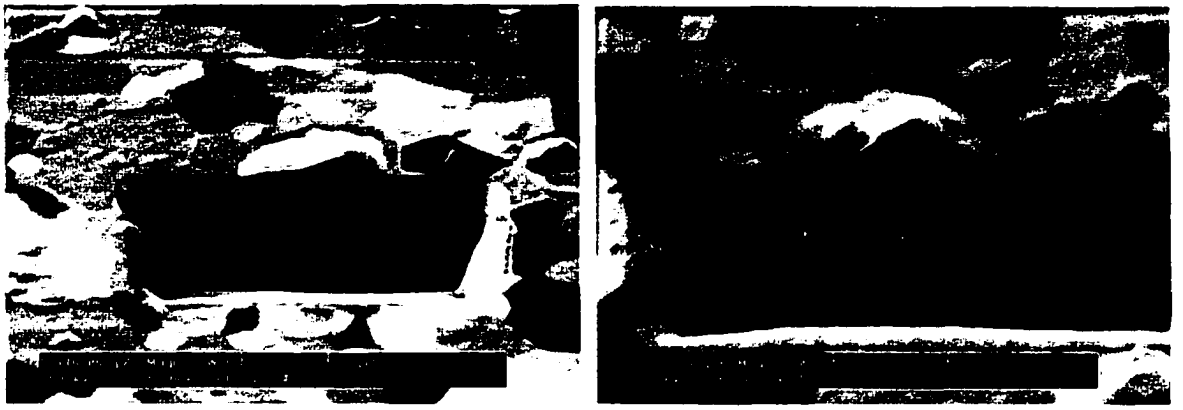

Figure 4.17. Cross sectional FIB images showing hillocks in the Al film [Kim 2001].

Grain boundary sliding mechanism may explain the hillock formation on the film. Large shear stress on a grain boundary causes a grain to slide on the substrate. Large void formation at the film/substrate interface supports the grain boundary sliding model. To understand buckling type hillock formation, the critical force for producing the buckling on the substrate is calculated by the interface delamination mechanism [Marshall et al. 1984].

$$\sigma_c = \frac{\gamma}{12}(1-\nu^2)E(t/a)^2 \quad (4.1)$$

where t is thickness, a is radius of the crack, γ is constant (14.68), E is Young's modulus and ν is Poisson's ratio.

However, the calculated stress for the buckling type hillock formation predicts very high stress up to 70 GPa. Such a high compressive stress was not observed during

annealing procedure, which is shown in Figure 6.2. There might be another mechanism necessary to form hillocks with the compressive stress.

The presence of N_2 may lead to such a hillock formation. N_2 gas can penetrate to the film through grain boundaries and reach to the substrate. The N_2 gas may expand at the bottom of the film resulting in a buckling type hillock formation after annealing. Without N_2 atmosphere, such a buckling type hillock formation is not observed. Pt films annealed in a vacuum atmosphere as shown in Figure 4.16 supports the atmosphere effect on hillock formation. Although the critical force for buckling type hillock formation may be over estimated due to inaccurate hillock size by the reversible hillock growth according to thermocycling [Lahiri 1969], the comparison of two different annealing atmospheres shows the N_2 gas effects on hillocks formation. The buckling type hillock formation is illustrated in Figure 4.18.

The composition of films plays an important role in the formation of hillocks. Figure 4.13 shows different behavior of hillock formation according to Ru composition. In the case of Pt-20wt%Ru film, no hillocks are observed after annealing. Alloy formation in the film could improve the adhesion of the film/substrate interface. However, scratch test of films does not show big different adhesion behavior according to Ru wt %. The hillock formation on Pt-20 wt% Ru may be suppressed due to high hardness of the film or diffusivity change in grain boundary with high Ru content. The diffusivity change may reduce the atmosphere effect and high hardness of alloy films may resist to the shear deformation of the grain boundary that is necessary for grain boundary sliding.

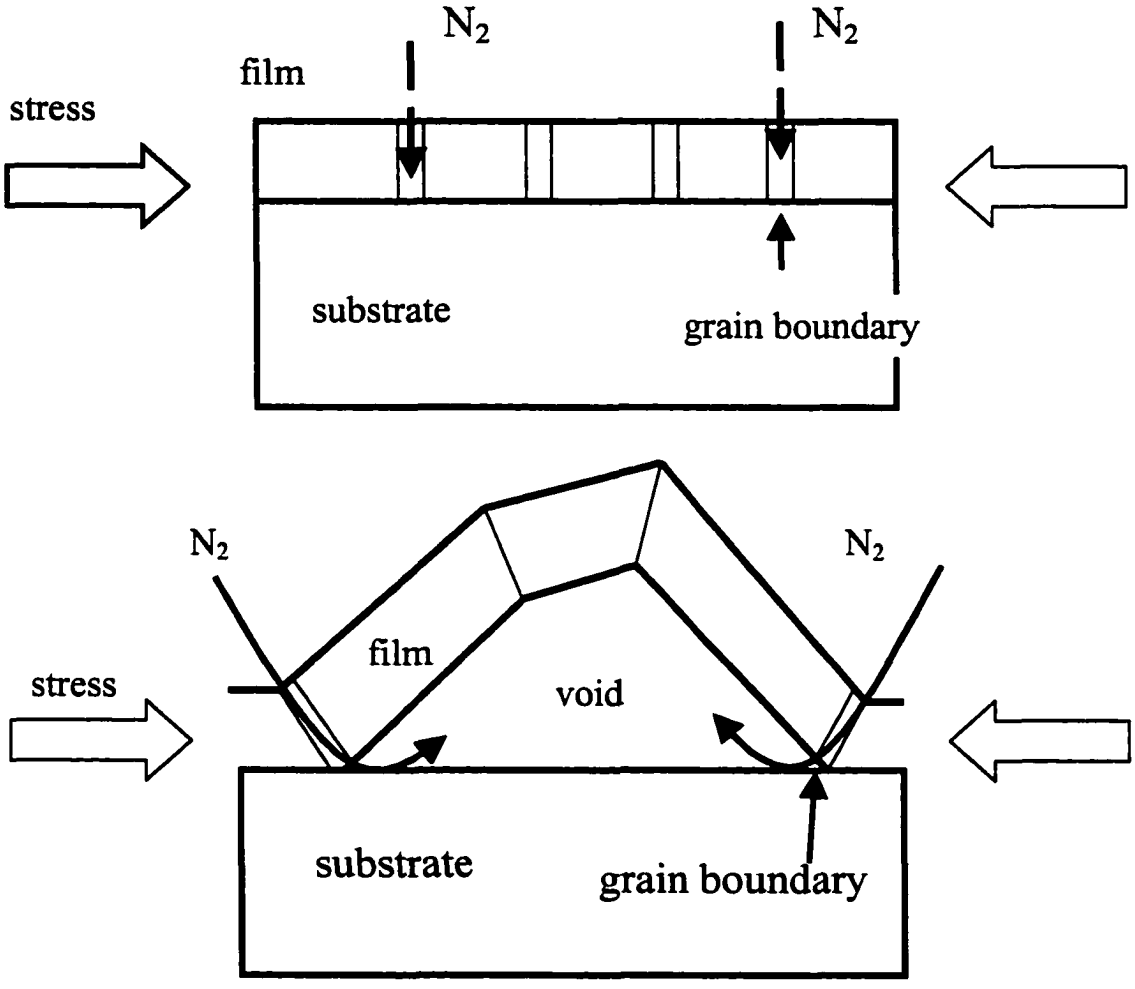

Figure 4.18. Possible grain boundary sliding mechanism on Pt film. Compressive stress with N_2 gas, which penetrates the film during annealing, forms bucking type hillocks.

Ch.5 Grain size effects on nanoindentation loading behavior of pure Pt thin films

5.1 Introduction

Low force, depth-sensing indentation has been developed over the last three decades to measure the mechanical properties of small scale materials [Gane et al. 1968, Doerner et al. 1986, Oliver et al. 1992]. The ease of sample preparation and convenient data acquisition from the instrument make the technique one of the most widely used methods for studying elastic and plastic properties of thin films. Features that differentiate this technique from standard hardness or microhardness tests are that the indentation size is often smaller than the grain size and indentation depth can be controlled on a very fine scale. Because the applied load is highly localized, depth-sensing techniques therefore provide a way to study fundamental dislocation processes during elastic-plastic deformation and, in particular, the effect of defect structure on the deformation [Michalske et al 1998, Kelchner et al 1998, Zimmerman et al. 2001] at the nanometer scale.

Numerous researchers have studied the early stages of elastic-plastic deformation during indentation and have observed pop-in behavior–a sudden change in indentation depth at approximately constant load–for a variety of materials, from metals to oxides [Page et al 1992, Gerberich et al. 1996, Bahr et al. 1998, Corcoran et al. 1997, Suresh et al. 1999, Gouldstone et al. 2000]. Two possible explanations have been reported regarding this discrete deformation behavior in the low loading regime. In one set of

observations, the failure of a thin oxide layer on the top of the material was the main mechanism resulting in the pop-in [Gerberich et al. 1996, Bahr et al. 1998]. However, pop-ins have also been observed in materials like sapphire and Au on which no surface layer is present [Page et al. 1992, Corcoran et al. 1997]. This pop-in behavior could possibly be attributed to existing defects [Oliver et al. 1984]. However, Page [Page et al. 1992] has demonstrated that pop-ins in the load-displacement curve of sapphire can be the result of dislocation loop nucleation under the indenter and not a result of existing defects in the indented materials. The discrete deformation behavior was observed not only in single crystals but also in polycrystals [Gouldstone et al. 2000]. Since the initial paper by Page [Page et al. 1992], discrete dislocation bursts have become a well accepted phenomenon and an active area of study.

Dislocation behaviors exhibited during depth-sensing indentation of thin films are often very different from those associated with traditional large-scale materials because the deformation field size is often in the range of the microstructural feature size. Although size dependent deformation behavior has been heavily investigated [Page et al. 1992, Corcoran et al. 1997, Suresh et al. 1999, Gouldstone et al. 2000], the deformation behaviors particular to thin films are still not fully understood. Recently, Lilleoden et al. [Lilleodden et al. 2001] showed evidence that microstructure plays a key role in determining the magnitude of the pop-in events in Au thin films. A small-grained film and a large-grained film, defined relative to the indenter tip size, displayed very different loading curves. This effect was attributed largely to easy dislocation nucleation when the indenter tip was near a grain boundary. However, this study was preliminary in nature.

In this Chapter, microstructure dependent deformation behavior was systematically explored to add to the growing understanding of pop-in behavior of polycrystalline materials. Pt is ideal for the study since no surface oxide forms and a wide variation of grain size can be obtained by controlling the deposition conditions. Also, the strong (111) texture of a typical Pt film removes many possible orientation effects on the deformation behaviors. A detailed examination of grain size effects on loading behavior was investigated by preparing three films with different average grain sizes. The deformation behavior was studied in terms of both grain size and proximity of the indenter tip to a grain boundary. The goals of this study were to understand small-scale deformation behavior related to the microstructural length scale and to investigate the dislocation effects on the discrete loading behavior according to the specific deformed area.

5.2 Nanoindentation technique

The elastic modulus and hardness of the indented materials can be obtained from the load-displacement data. The key parameters that are to be accurately measured from the data are the final depth of indentation, the stiffness/compliance at initial unloading, and the continuous variation of stiffness/compliance from the unloading curve.

Doerner and Nix [Doerner et al. 1986] introduced a comprehensive method for determining hardness and modulus from indentation load-displacement data. This approach is based on the observation of the initial stages of unloading in the data, and they proposed the indenter could be modeled as a flat punch. Their assumption that the area of contact remains constant as the indenter is unloaded presumes that the initial

portions of unloading curves are linear. The unloading stiffness S=dP/dh can be obtained by fitting a line to the initial portion of the unloading curve as shown in Figure 5.1(a). The contact depth, h_c, can also be obtained from an intercept on the displacement axis. However, the assumption of the Doerner technique, linear unloading at load-displacement curve, did not accurately fit to experimental results.

Oliver and Pharr [Oliver et al. 1992] presented several indentation data, which included indentation results of aluminum, sapphire, fused silica, tungsten and soda lime glass, and pointed out that the shapes of the unloading curves from all materials are not linear. The unloading data are better described by a power law fit. They outlined a new method for analyzing indentation load-displacement data based on this observation. Their method uses analytical solutions for indenter geometries other than a flat punch. A conical indenter was chosen to describe the elastic unloading of an indentation made with a Berkovich indenter because its cross-sectional area varies as the square of the depth of contact, like the Berkovich indenter. For both indenter tips, the load-displacement relationships are nonlinear and the contact area changes continuously during unloading. Figure 5.1(b) shows a cross section view of an indentation and illustrates the parameters for the analysis.

The total displacement h is written as

$$h = h_c + h_s \quad (5.1)$$

where h_c is the vertical distance along which contact is made and h_s is the displacement of the surface at the perimeter of the contact. At peak load, the load and the displacement are P_{max} and h_{max}, respectively, and the radius of the contact circle is a. Upon unloading,

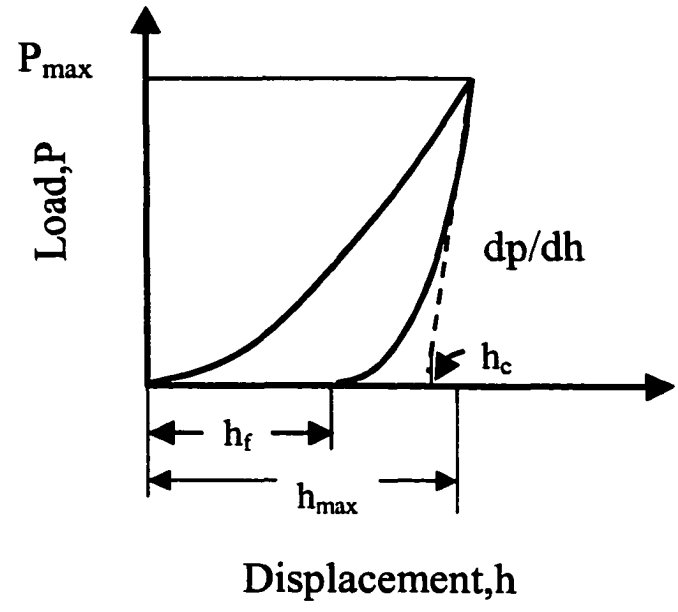

(a)

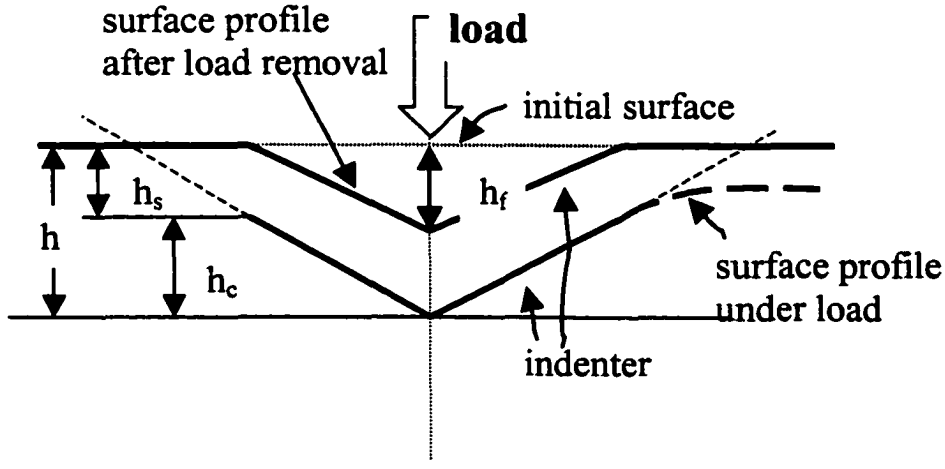

(b)

Figure 5.1. A schematic diagram of a load-displacement curve (a) and a section of an indentation(b)[Oliver et al. 1992]. The experimental parameters to determine hardness and modulus are shown.

the elastic displacements are recovered, and when the indenters is fully withdrawn, the final depth of the residual hardness impression is h_f.

To determine hardness and modulus, three parameters that are the peak load, P_{max}, the depth at peak load, h_{max}, and the initial unloading contact stiffness, S, should be obtained. The contact stiffness, S, is given by the expression [Sneddon 1965]

$$S = \frac{dP}{dh} = \frac{2}{\sqrt{\pi}} E_r \sqrt{A_c} \quad (5.2)$$

$$E_r = \frac{\sqrt{\pi}}{2} \frac{S}{\sqrt{A}} \quad (5.3)$$

where P is the load applied to the indenter, h is the displacement into the sample, A_c is the contact area between the indenter and the film, and E_r is the reduced modulus, given by

$$\frac{1}{E_r} = \frac{1-\nu_f^2}{E_f} + \frac{1-\nu_i^2}{E_i} \quad (5.4)$$

In here, E_f and E_i are the elastic modulus of film and indenter, respectively, and ν_f and ν_i are the Poisson's ratio of film and indenter.

The unloading curve follows a power law relationship as given by

$$P = \alpha(h - h_f)^m \quad (5.5)$$

The contact area at peak load is determined by the geometry of the indenter and the depth of contact, h_c. To determine the contact depth from the experimental data, it is noted that

$$h_c = h_{max} - h_s \quad (5.6)$$

and from Oliver et al.[Oliver et al. 1992]

$$h_s = \varepsilon \frac{P_{max}}{S} \quad (5.7)$$

where ε is a function of the shape of the indenter tip (ε ≅0.75 for a Berkovich indenter) [Oliver et al. 1992]

Hardness is defined as the ratio of the maximum load to the contact area of the indentation.

$$H = \frac{P_{max}}{A_c} \quad (5.8)$$

The contact area, Ac, is determined from the data.

For the ideally perfect Berkovich indenter, the area function is given by

$$A(h_c) = 24.5h_c^2 \quad (5.9)$$

5.3 Model of strain gradient plasticity

Conventional plasticity theory considers the properties of materials to be independent of material length scales. Any hardness increase at small loads is believed to be a consequence of poor surface preparation and inadequate indent area measurement [Vitovec 1986]. However, there are several experiments [Ma et al. 1995, Fleck et al. 1994] that indicate a size dependence of material strength. A small deformation shows stronger mechanical behavior compared with a larger deformation tested in the same material. Structures made of small dimension materials also have much higher yield stress than their bulk forms. The effect of length scales in the case of small deformation must be considered in order to understand the mechanical behavior of small dimension

materials. If the deformation field is small compared to a material length scale, a strain gradient term can be included to explain the observed plastic deformation.

The hardening of a crystalline material is attributed to the density of dislocations. Two cases of dislocation storage can be addressed here. First, the stored dislocations due to the action of locking mechanisms are called "statistically stored dislocations". Second, gradients of plastic shear due to inhomogeneous plastic deformation produce "geometrically necessary dislocations". If a material contains a deformation field and a non-deformation field as shown in Figure 5.2, plastic strain gradients appear. The indentation of a material results in the deformation field beneath the indenter.

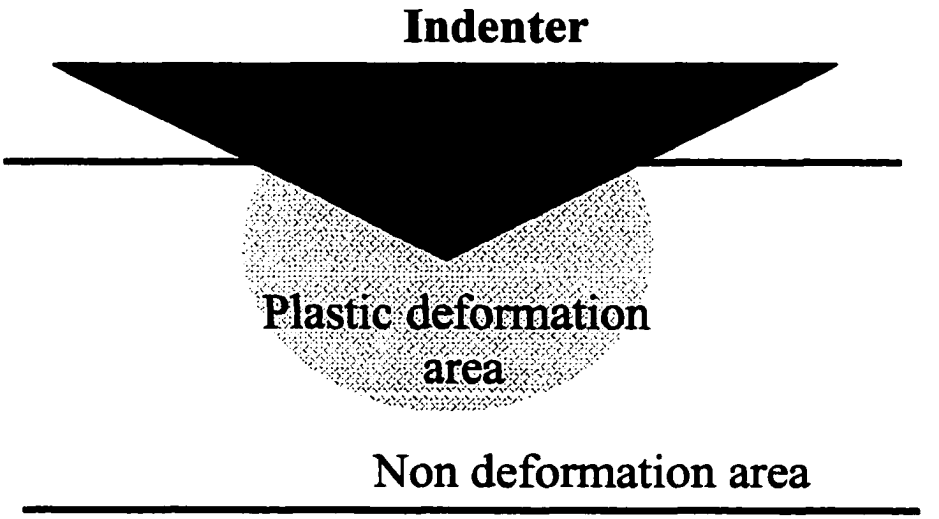

Figure 5.2. Schematic diagram of plastic strain gradient due to indentation.

As the indentation produces large deformation, the total length of the dislocation loops increase. The total length of loops, λ, is proportional to the contact area and the indentation depth as given by [Nix et al. 1998]

$$\lambda = \frac{\pi h a}{b} \quad (5.10)$$

and the hemispherical volume of plastic deformation zone, V, is defined by

$$V = \frac{2}{3}\pi a^3 \quad (5.11)$$

Thus, the density of the dislocation loops is to be

$$\rho_G = \frac{\lambda}{V} = \frac{3h}{2ba^2} = \frac{3}{2\mathrm{bh}}\tan^2\theta \quad (5.12)$$

$$\tan\theta = \frac{\mathrm{h}}{\mathrm{a}} = \frac{\mathrm{b}}{\mathrm{s}} \quad (5.13)$$

From the Taylor relationship between shear stress and dislocation density, the total shear stress can be defined by

$$\tau = \alpha\mu b\sqrt{\rho_G + \rho_S} \quad (5.14)$$

where α is a Schmid Factor constant of 0.3, μ is the shear modulus and ρ_s is the density of statistically stored dislocations. The constant value, α, is chosen for Pt indentation data.

By considering Tabor's factor and the von Mises flow rule, shear stress can be converted to hardness as follows

$$H = 3\sigma,\ \sigma = \sqrt{3}\tau \quad (5.15)$$

$$H = 3\sqrt{3}\tau \quad (5.16)$$

From Equations 5.12, 5.13, 5.14 and 5.16, hardness can be expressed as

$$\frac{H}{H_o} = \sqrt{1 + \frac{h^*}{h}} \quad (5.17)$$

$$H_o = 3\sqrt{3}\alpha\mu b\sqrt{\rho_s} \quad (5.18)$$

$$h^* = \frac{81}{2} b\alpha^2 \tan^2\theta \left(\frac{\mu}{H_o}\right)^2 \quad (5.19)$$

where h* is depends on indenter geometry and the density of statically stored dislocations.

The relationship between hardness and displacement can be predicted according to the strain gradient model. When a Berkovich tip is used, the relationship of indenter depth and contact area is defined by

$$A_c = 24.5h^2 = \pi a^2 \quad (5.20)$$

and this relationship gives the values of tanθ to be

$$\tan\theta = \frac{h}{a} = \sqrt{\frac{\pi}{24.5}} = 0.358 \quad (5.21)$$

H_o is defined as a hardness considering only the density of statistically stored dislocations without the density of geometrically necessary dislocations. Thus, H_o is obtained from Bulk shear stress value of 462 MPa with Equation (5.16) and h* is also calculated from the Equation 5.19 with H_o value of 2.4 GPa and Equation 5.21. Therefore, hardness and depth of indentation can be plotted by following Equation 5.19 with known values. The parameters and values for the calculation are shown in Table 5.1.

Although a sharp Berkovich tip is used for the indentation, the tip of the indenter is not ideally sharp. At very shallow displacement (up to 14nm in the case of 150 nm radius tip), the indentation behavior with a spherical indenter should be considered

[Gouldstone et al. 2000]. When a spherical indenter tip is used, the relationship of indenter depth and contact area is defined by

$$A_c = 2\pi Rh - \pi h^2 = \pi a^2 \quad (5.22)$$

The value of tanθ is expressed as

$$\tan\theta = \frac{h}{a} = \frac{h}{\sqrt{2Rh - h^2}} \quad (5.23)$$

The density of the dislocation loops is to be

$$\rho_G = \frac{\lambda}{V} = \frac{\frac{\pi h}{b}a}{\frac{2}{3}\pi a^3} = \frac{3}{2bh}\tan^2\theta = \frac{3}{2bh} \times \frac{h^2}{2Rh - h^2} \quad (5.24)$$

Table 5.1. The parameters and calculated values for strain gradient model

	H_0 (GPa)	h* (nm) for berkovich tip	μ (GPa)	b (nm)	α
Pt	2.4	129.7	76	0.277	0.3

5.4 Experimental Procedures

All substrates were 3-inch diameter Si (100) wafers with a thermally grown oxide layer approximately 100nm thick. The average wafer thickness was close to 400 μm thick. Three Pt films with different grain sizes were prepared by DC-magnetron sputtering.

A Pt film with small grain size (designated GS 35, as discussed later) was deposited on an uncooled substrate at ambient temperature with a base pressure of

4.5×10^{-9} torr and an Ar pressure of 2×10^{-3} torr. The deposition rate was approximately 25 nm/min at a sputter power of 150 W. The substrate was pre-cleaned with an ion gun to improve the adhesion between the film and the substrate.

A pair of Pt films 200nm thick (GS 150) and 500nm thick (GS 200) were deposited at 350°C. The substrates were pre-cleaned with the standard RCA cleaning procedure. Both substrates were heated to 400°C for 40 min before film deposition to reduce any moisture effects. Sputtering power of 30W and 5×10^{-3} torr Ar pressure were necessary to promote good adhesion to the underlying oxide. The deposition rate was 4.2 nm per min under these conditions.

The average grain sizes of the films were measured from bright field Transmission Electron Microscope (TEM) images. Approximately 150 to 250 grains were used to measure average grain size of each film by hand-tracing the grain boundaries then analyzing the traces with NIH image software. A lognormal distribution [Tao 2002, Zielinski 1995] was used to describe the grain size distributions of the three films. Cross-section images of GS 150 and GS 200 were acquired with a Focused Ion Beam instrument (Fei XP dual beam workstation) to examine the grain morphology. All microstructure analyses are described in Chapter 4.

For a qualitative measure of texture, a Rigaku X-ray diffractometer system was used to perform θ-2θ (Bragg-Brentano) scans. All films show strong (111) crystalline orientation (Chapter 4).

Depth-sensing indentation (Hysitron Triboscope) was used to measure the mechanical behavior of the three Pt thin films. To minimize the substrate effect, indentation depths were limited to 10-20% of the sample thickness. The instrument's

capability for *in situ* high resolution surface imaging was used to observe the indented region by scanning with the indenter tip before and after indentation.

5.5 Results

5.5.1 Low load behavior

Figure 5.4 shows the full load-displacement curves for indentations of GS 35, GS 145 and GS 200. Magnifications of the initial loading curves of the three specimens are shown in Figure 5.5. As shown in the Figures, the three loading curves represent a range of behaviors that are related to the different grain sizes. To understand the loading curve behavior, the initial loading curves are compared with that of elastic contact shown in Figure 5.5. According to the continuum elasticity model of Hertz, elastic deformation is given by the relationship [Johnson 1985],

$$P = \frac{4}{3} R^{1/2} E_r d^{3/2} \quad (5.25)$$

where P is the load, R is the tip radius, d is the deformation depth and E_r is the reduced modulus. E_r is obtained by Equation (5.4). A reduced modulus of 205 GPa for (111) Pt is used for the calculation assuming E_f is 213 GPa, E_i is 1140 GPa, ν_f is 0.39 and ν_i is 0.07.

The elastic response curve fits well with the initial curves of GS 145 and GS 200 before pop-in behavior occurs. As indentation load increases, sudden discrete behavior is observed and the load-displacement curve deviates from the elastic loading curve calculated from Equation (5.25). However, the loading curve of GS 35 is not described by elastic deformation of Hertzian contact. Instead, it follows the Herzian curve only if a reduced modulus of 60 GPa is selected for the calculation of the elastic response. Clearly

this is not due to a true increase in sample compliance, so elastic-plastic deformation must be occurring immediately. In the initial portion of loading (Figure 5.5), GS 35 is less resistant to deformation than the other samples. The first sudden discrete deformation events (pop-ins) are seen in GS 145 and GS 200 at loads of 12 μN and 22 μN respectively (Figure 5.5). In contrast, the loading curve of GS 35 appears to be continuous. Very small discrete deformation loading events may be present in the initial part of the loading curve but the jumps could also be due to other factors such as surface roughness.

The trends shown in Figures 5.4 and 5.5 can also be expressed as changes in hardness throughout each test. Hardness values for the three Pt films calculated at different points on the loading curves are shown in Figure 5.6a. For this plot, hardness is calculated as the load divided by the contact area at all points along the load-displacement curve. The contact area in this calculation is simply obtained from the area function without the elastic recovery. Although this calculated hardness is not the standard indentation hardness value, it is indicative of the resistance to deformation for each of the three films at the specific load. As shown in Figure 5.6b, if hardness values are taken at a load of only at 20 μN then the values increase as average grain size increases. This behavior is expected from the loading curves in Figure 5.5. The purely elastic response of GS 200 gives high strength at the early deformation whereas the immediate inelastic response of GS 35 reveals easy deformation.

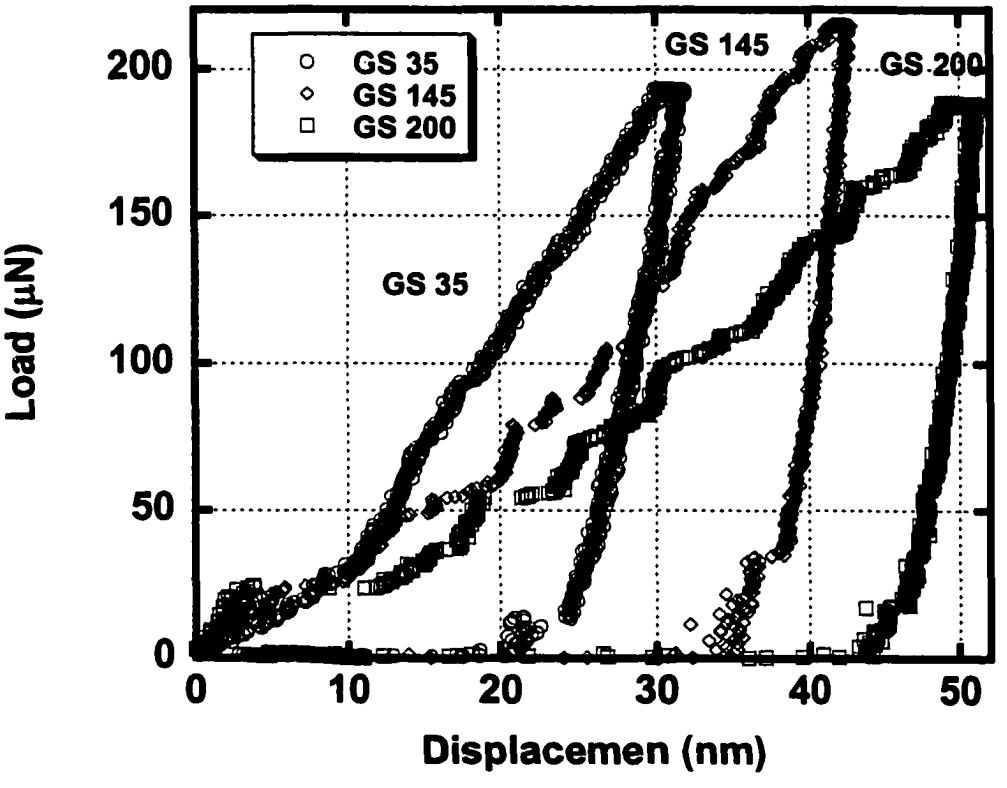

Figure 5.4. Comparison of the load-displacement curves of GS 35, GS 145 and GS 200, named as average grain sizes of three Pt films.

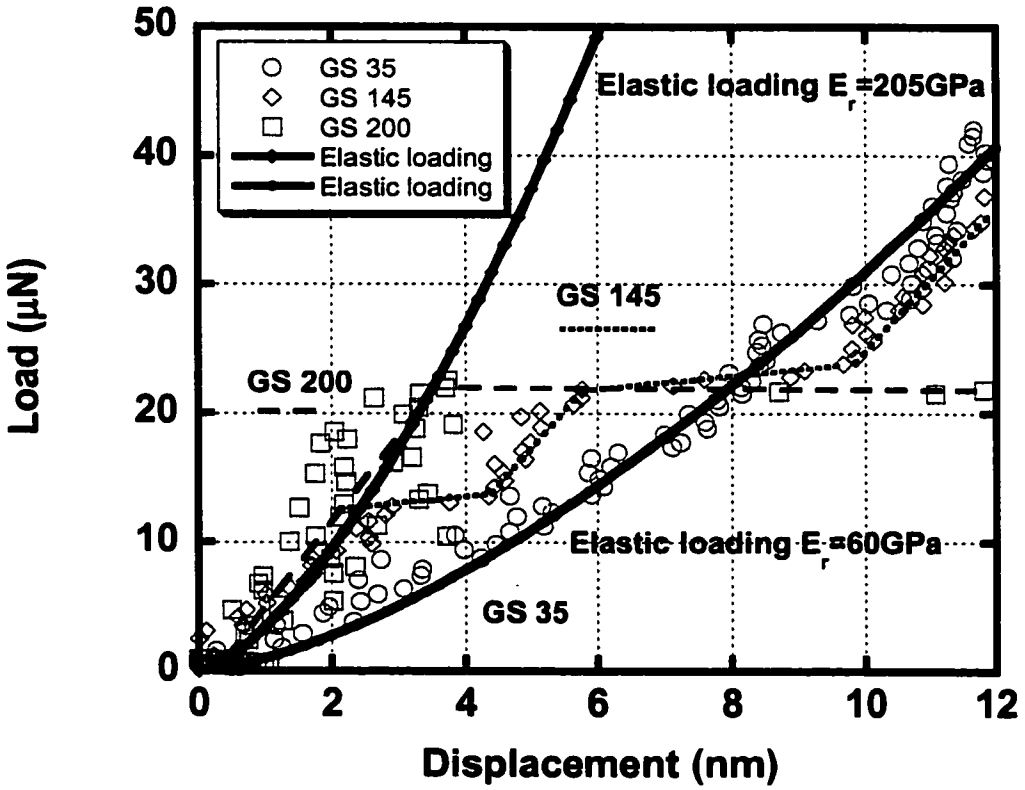

Figure 5.5. Comparison of the loading curves of GS 35, GS 145 and GS 200 at very low loads. The small and large discrete behaviors are observed in GS 145 and GS 200. The lines are the elastic response of Hertzian fit from Equation 5.22.

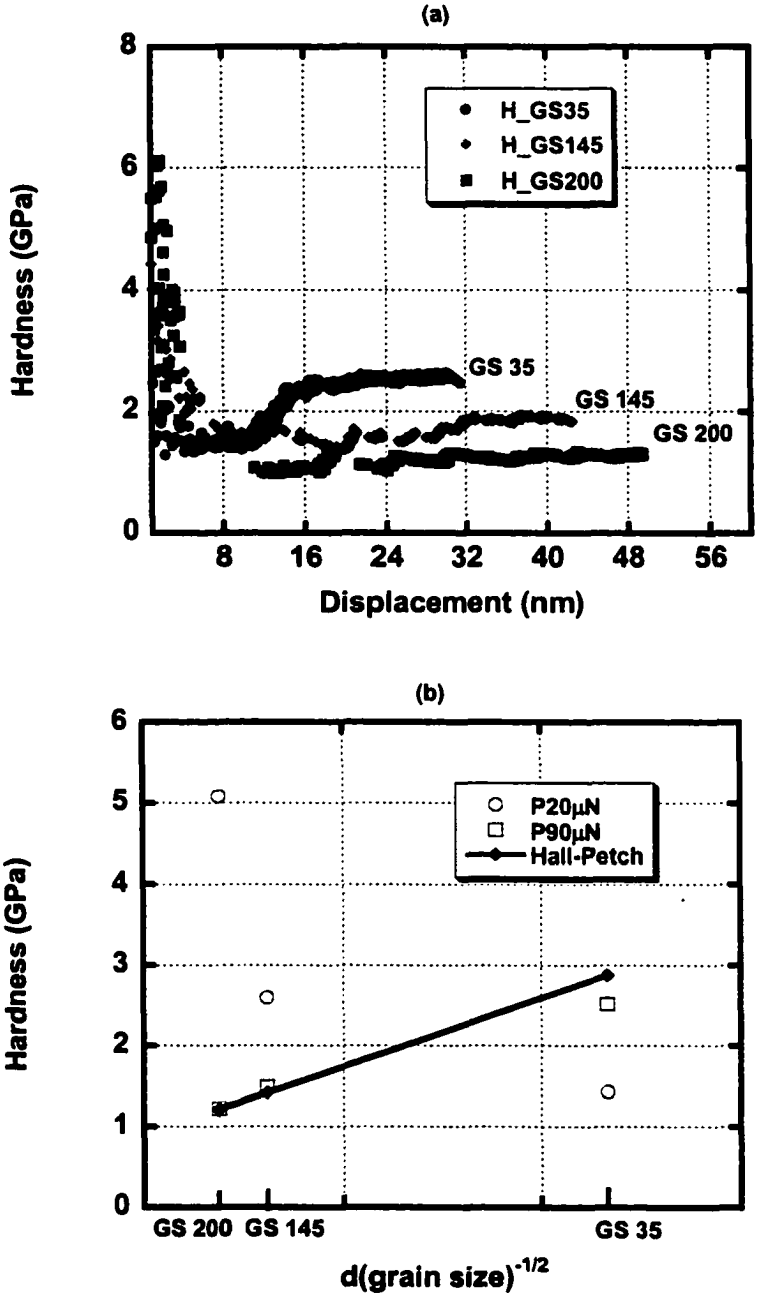

Figure 5.6 (a) Comparison of Hardness of GS 35, GS 145 and GS 200 according to displacement. High strength is observed in GS 145 and GS 200 at the early displacement. (b) Hardness versus inverse square root of average grain size of Pt films. Hardness in this graph is obtained at specific loads (20μN and 90μN) divided by the contact area. Hardness at 90μN increases as average grain size decreases. However, GS 200 (largest average grain size) shows highest hardness at 20μN. Hardness values at 90μN follow Hall-Petch relationship (grain size strengthening mechanism)

of GS 200 are depicted, one for an indent near the center of a grain and one for an indent that overlapped a grain boundary. The indentation in the center of a single grain of the 500nm thick Pt film (GS 200c) shows several pop-in behaviors during indentation, whereas the indentation on a grain boundary in the same film (GS 200gb) shows much less discrete behavior, and approaches a continuous loading curve. Ultimately, the hardness of GS 200gb is higher than that of GS 200c (2.73 GPa and 1.53 GPa respectively). The AFM images of two indented areas of GS 200gb and GS 200c before and after indentations are represented in Figure 5.8.

A few different loading curves of 500nm thick Pt film, which are local microstructure dependent, were observed as shown in Figure 5.9. The AFM images of GS 200 before and after indentation are shown in Figure 5.10. All three deformations demonstrate similar loading behavior at the low displacement, but the plastic deformation of GS 200 starts at a higher load than those of GS 200c and GS 200gb do. Other different deformation behaviors are observed at large displacement. A higher load for GS 200gb deformation is ultimately required because reduced pop-in behavior is observed in the loading curve. GS 200 and GS 200c show a different discrete deformation behavior during initial loading, but at large deformation the loading behaviors are similar to each other. Similar loading behavior was also observed in the GS 145 indentation (Figure 5.11). Although the loading curves of 500nm thick film and GS 145 show several different behaviors, the loading curves of GS 35 are very reproducible as shown in Figure 5.12. The small grain size in GS 35, which is smaller than the tip radius, may produce a reliable loading behavior.

(a) GS 200c

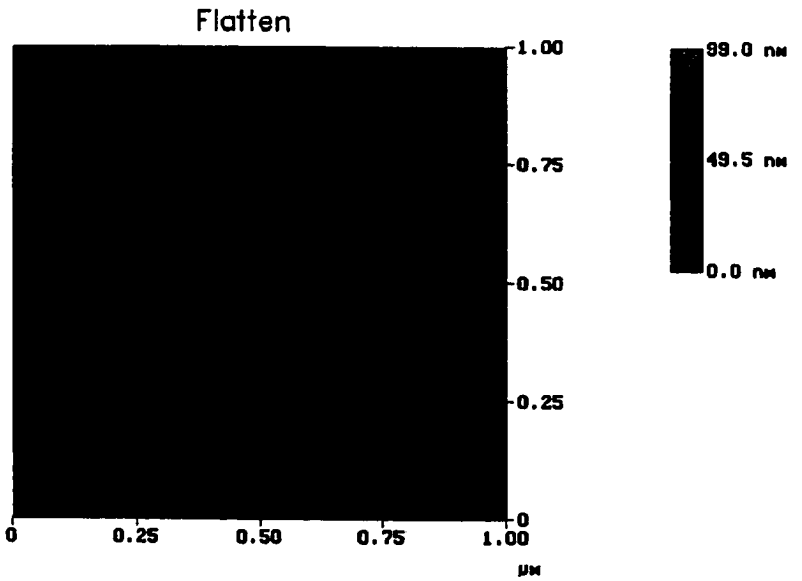

Before indent

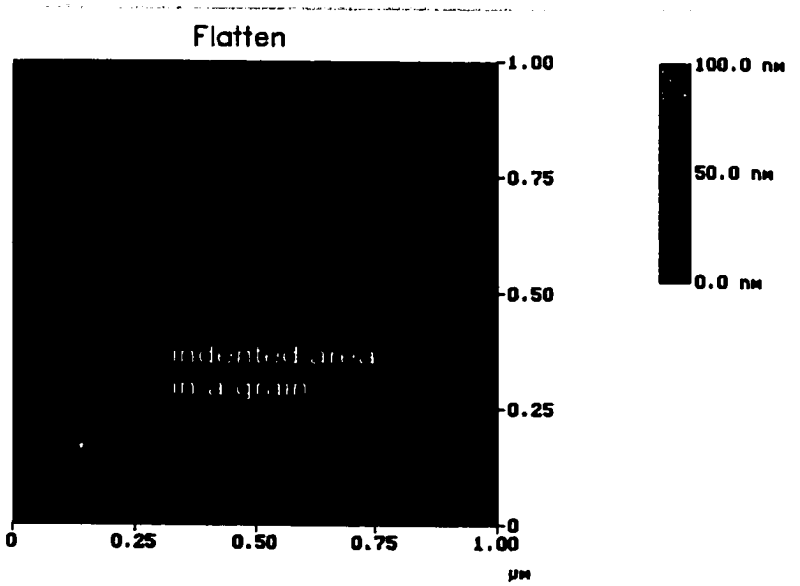

After indent

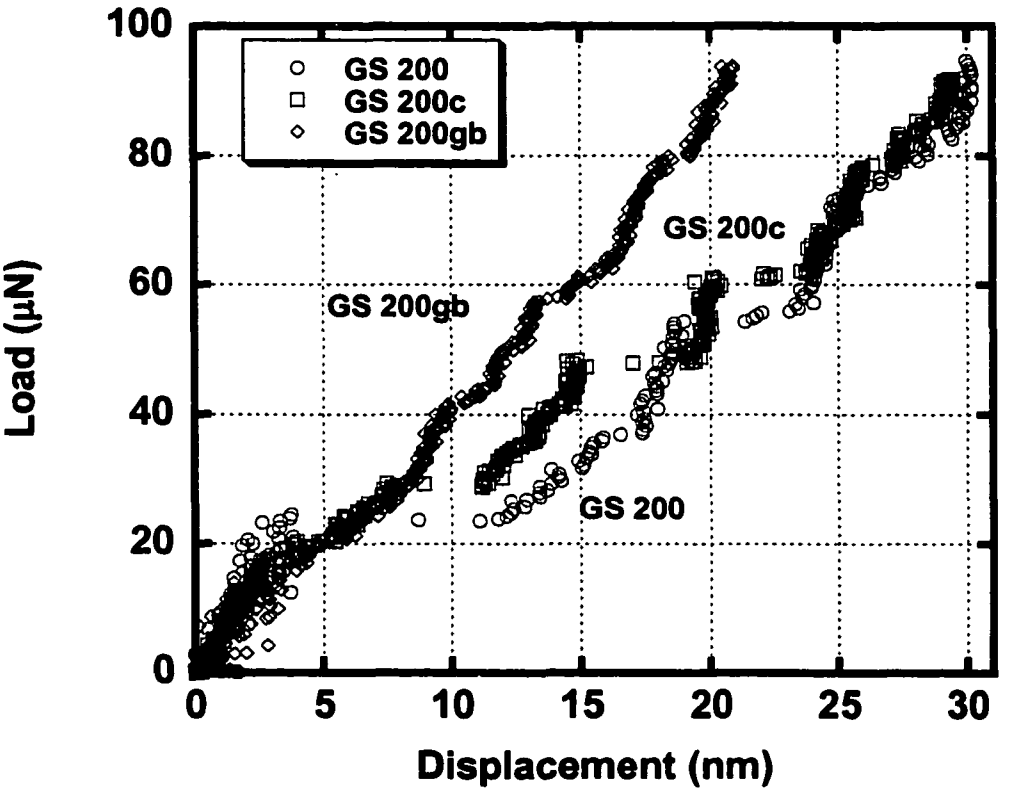

Figure 5.9 Comparison of loading-displacement curves of GS 200, GS 200c and GS 200gb. Although all three loading curves show similar behavior at the early stage of displacement, three samples represent different deformation behavior as displacement increases. The higher load is required for deformation of GS 200gb. GS 200 and GS 200c have different pop-in behavior but load behavior is similar at large displacement.

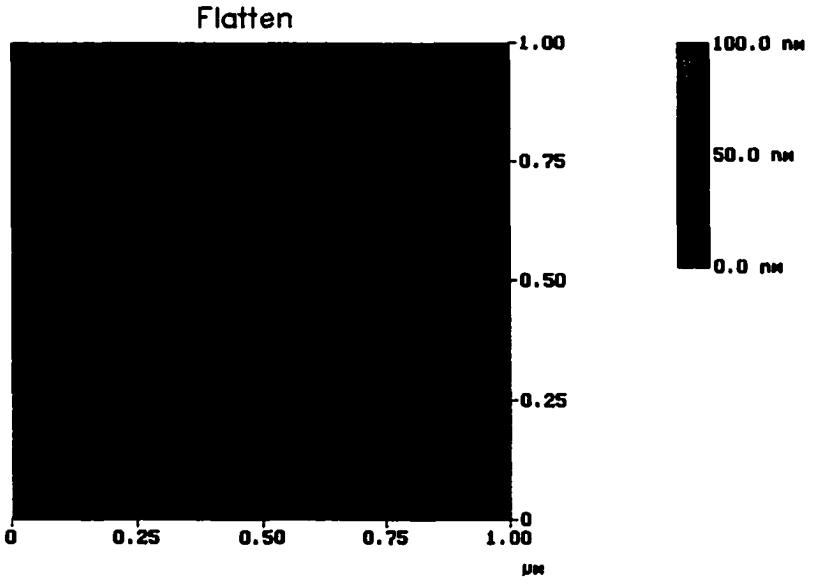

(a) before indent

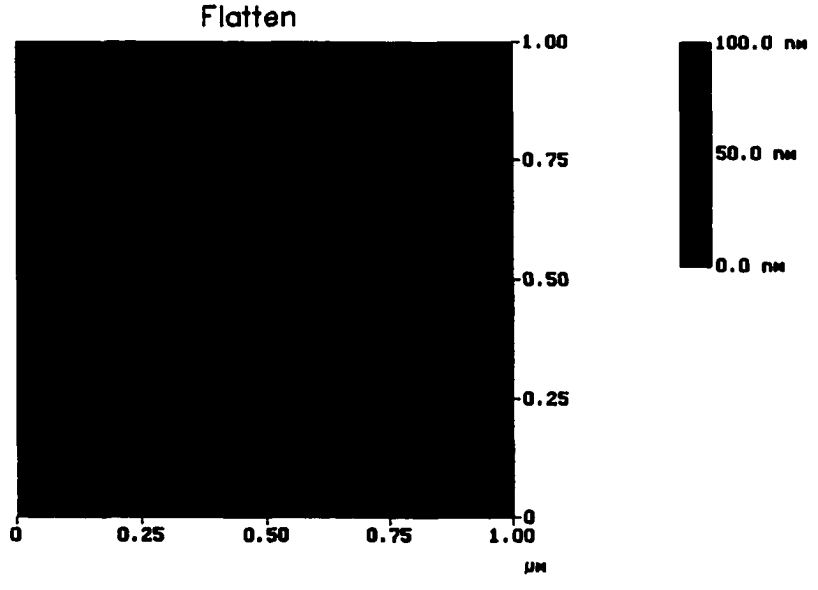

(b) after indent

Figure 5.10. AFM images of GS 200. Indentation starts on the one grain and indentation area includes the grain boundary.

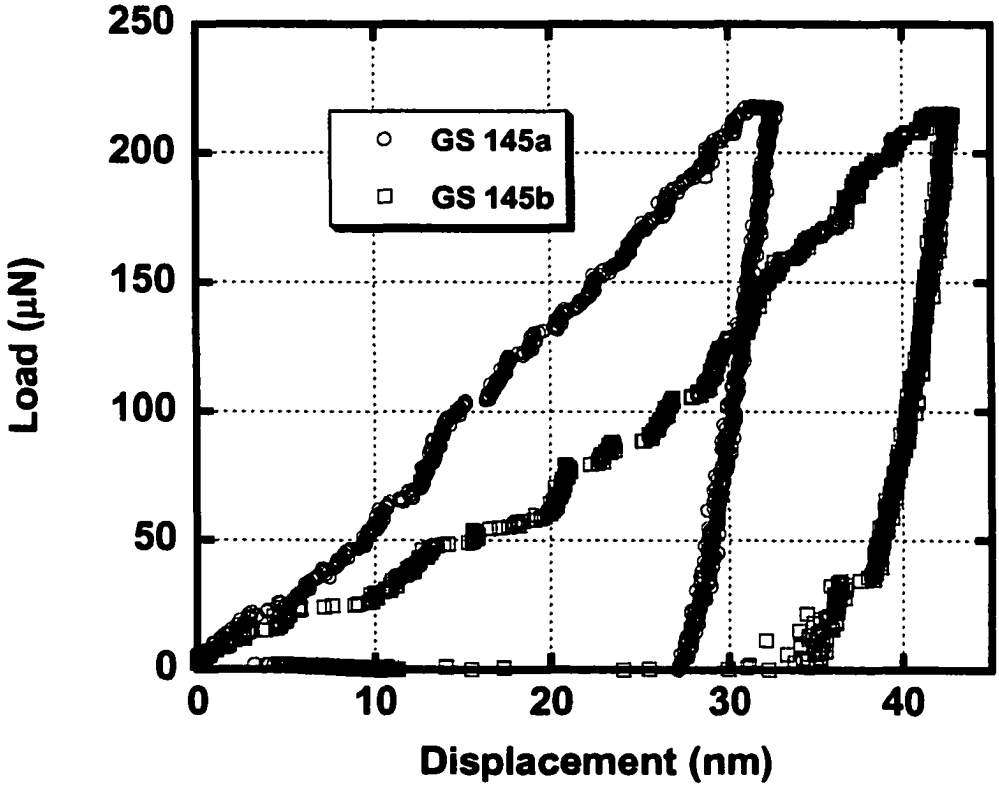

Figure 5.11. Comparison of two loading curves (GS 145). Indentation location may affect the different loading behavior. The grain boundary deformation could cause the hardening behavior of GS 145 a. The detailed analyses including images of indentation area are shown in the case of GS 200gb.

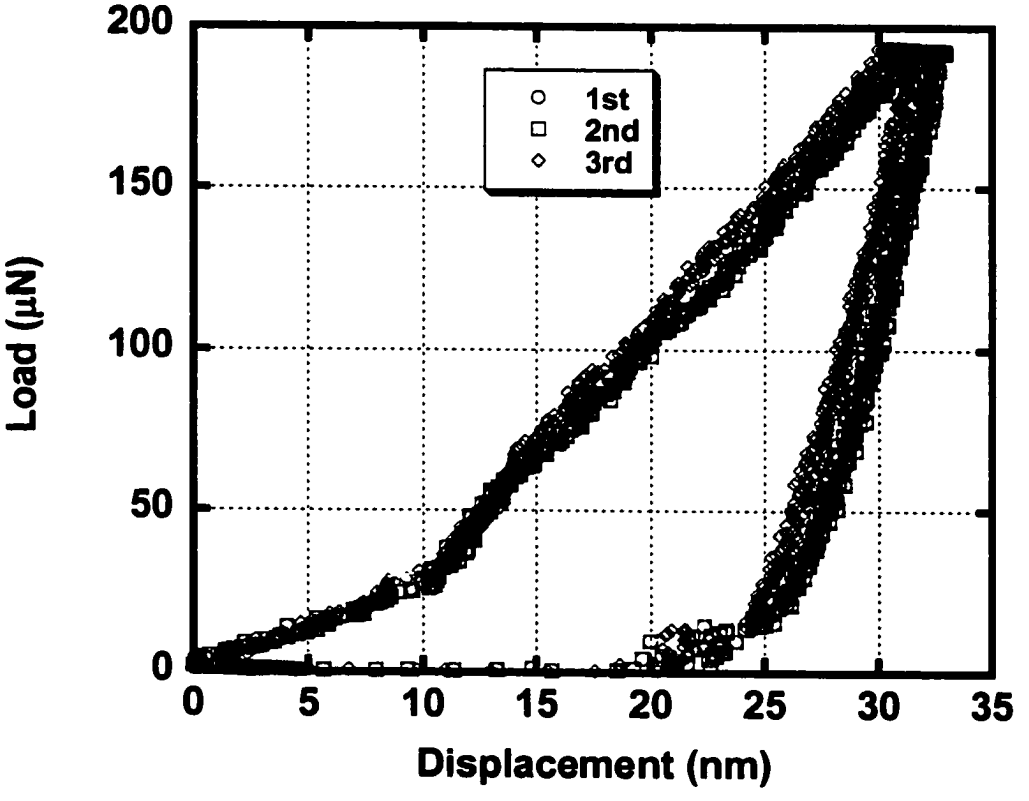

Figure 5.12. Nanoindentation on GS 35. All loading behaviors are very similar. The deformation does not depend on the indentation position (microstructure insensitive deformation).

5.5.3 Strain gradient effects

Comparison of the strain gradient model with Berkovich tip [Nix et al. 1998] and experimental data of GS 35 is shown in Figure 5.14. Although the strain gradient model predicts high hardness at the low displacement, hardness of GS 35 is consistent with indentation depth.

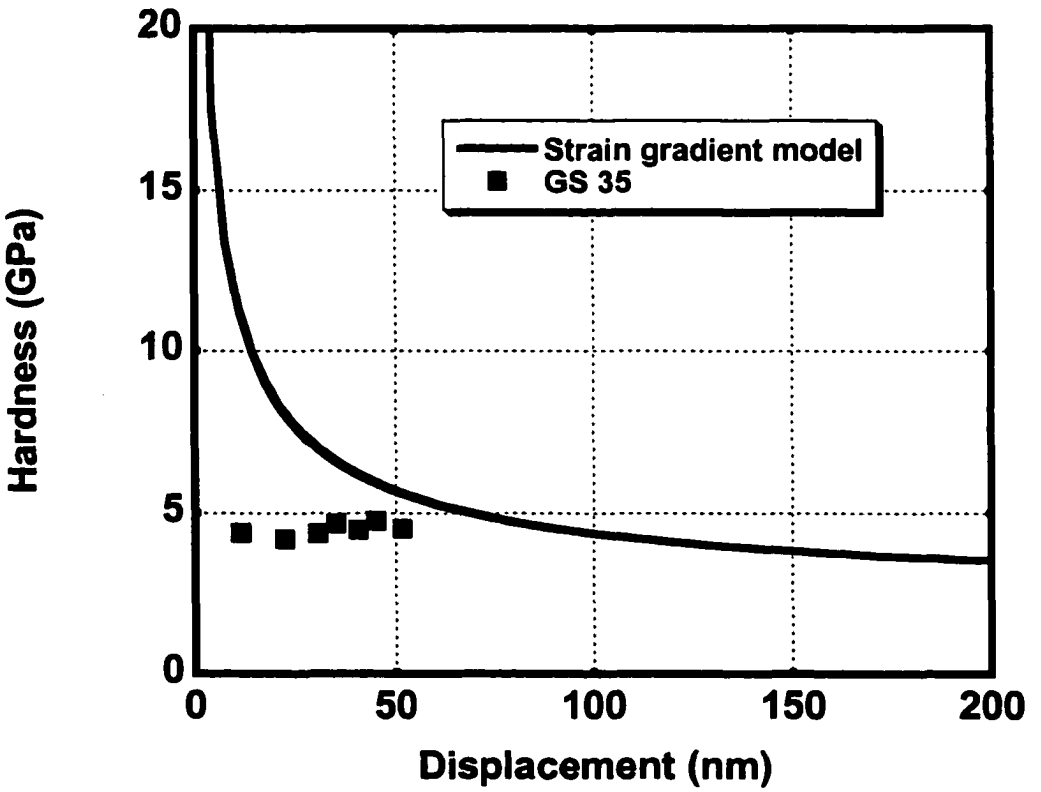

Figure 5.14. Comparison of strain gradient model with Berkovich tip and experimental data of GS 35. The hardness of GS 35 is almost consistent with indentation depths.

5.6 Discussion

5.6.1 General discussion of grain boundary source model

The behavior of GS 35 and GS 145 can be explained by examining the role of the grain boundaries as dislocation sources. Li and Chou [Li et al. 1970] suggested that grain boundaries act as sources of dislocations. The ability to emit dislocations depends on the structure and composition of the grain boundary, but is not related to grain size. The theory was based on the observation that advancing slip activity occurs at the vicinity of grain boundaries, and the dislocation emission occurs with grain boundary dislocations (ledges). The grain boundary source may describe the elastic-plastic soft behavior of GS 35 and GS 145 at the early deformation.

Several other recent studies of small-grained materials support the grain boundary source theory. Results from indentation of Au films were also explained using the grain boundary source theory, and an embedded atom simulation of plastic deformation from a grain boundary confirmed the theory [Lilleodden et al. 2001]. The plastic deformation of a bulk nanocrystalline material has been modeled as the nucleation of extended dislocations by the successive emission of two partial dislocations from the grain boundaries [Yamakov et al. 2001]. At a high enough stress, a single partial is nucleated from a grain boundary in small grains.

A similar low-strength loading behavior associated with high defect density has also been reported [Bahr et al. 1998]. The dislocation density determined elastic or non-elastic behavior. The high defect density samples could not follow the elastic behavior, whereas the specimen with the low defect density reached near theoretical shear stress before the plastic deformation occurred.

5.6.2 Effect on small and large grained film (easy plasticity vs. Hertzian loading)

We begin by analyzing the behavior of GS 200, the large grained film, in which the sudden pop-in behavior at a low load is due to plastic deformation.

The maximum pressure under an indenter tip, P_o, is given by [Johnson 1985]

$$P_o = \frac{3P}{2\pi a^2} = \left(\frac{6PE_r^2}{\pi^3 R^2}\right)^{\frac{1}{3}} \quad (5.28)$$

From the above equation of contact radius (a), indenter radius (R), and the load (P), P_o can be defined as the maximum shear stress under a spherical elastic contact. The shear stress can be obtained from the relationship

$$\tau_{max} = 0.31P_o = 0.31\left(\frac{6PE_r^2}{\pi^3 R^2}\right)^{\frac{1}{3}} \quad (5.29)$$

where P is the load value at which the plastic deformation occurs (plastic threshold). From Equation 5.29, the maximum resolved shear stress at the point of discrete behavior in the GS 200 loading curve is 6 GPa. While this may not be the exact value of shear that exists on the slip planes of a (111) textured film, it provides a reasonable number for comparison to dislocation theory.

The flow stress of materials ranges between two bounds. The upper bound is the high stress required for a shear collapse of the perfect lattice and the lower bound is the stress needed for glide of existing dislocations [Cahn et al. 1993]. In the former case, nucleation of a dislocation loop induced during indentation initiates plastic deformation. If we assume a single grain of GS 200 is a perfect single crystal, the shear stress for nucleation of a dislocation loop in one grain during indentation is the ideal shear strength. Pt is a high stacking fault energy FCC material. Thus, a high theoretical value is expected

for homogenous dislocation nucleation. The ideal shear strength can be given by [Cahn et al 1993, Hull et al. 1984, Hertzberg 1996]

$$\tau \approx \frac{\mu}{10}, \text{ or } \tau \approx \frac{\mu}{2\pi} \quad (5.30)$$

where μ is a shear modulus. The shear modulus of Pt (111) is 76 GPa. So the theoretical shear stress required for plastic deformation is in the range of 7.6 to 12.1 GPa. Thus, the theoretical strength value is close to the experimental measurement of 6 GPa for the maximum shear stress. The first deviation of GS 200 from the elastic loading curve appears to occur when the maximum shear strength at the tip of the indenter reaches the value of the theoretical strength of Pt. Therefore, the initial pop-in behavior of GS 200 can be reasonably described as plastic deformation of a perfect Pt crystal.

Next, we examine the behaviors of the smaller-grained films, GS 35 and GS 145, at the initial loading portion of the deformation. GS 35 does not follow the elastic response expected of Pt. Instead, easy deformation of GS 35 at the initial loading was observed. GS 145 shows an elastic response at the beginning of the loading curve, but pop-in behavior starts at a lower load compared to the discrete deformation of GS 200. The onset of plasticity of GS 145 initiates more easily than for GS 200. Broadly speaking, then, small grain size results in easier initial plastic deformation than large grain size does.

The observed dependence of initial plasticity on grain size could possibly be attributed to the effect of dislocation density on the deformation behavior. A defect-free, perfect crystal shows the ideal shear stresses whereas materials with the pre-existing defects are prone to plastic deformation more easily. However, work hardening is also

expected in films after thermal treatment [Shen et al. 1998, Keller et al. 1998]. The as-deposited sample has some defects in the material during deposition (Chapter 4). The annealing effect is ignored in this study.

Although GS 200 is thicker than other two samples, the initial deformation of all three films is at a very low depth (less than 11nm). The film thickness does not influence the behavior of the early load-displacement curve.

Figures 5.15 and 5.16 show the average number of grains and grain boundary length contacted versus indentation depth of the three Pt films. The number of grains and grain boundary length are calculated as average grain size divided by the calibrated area function. Compared with GS 200, where on average only one grain was contacted at the initial indent, several grains of GS 35 immediately were involved. GS 145 and GS 200 shows similar contacted grain numbers and grain boundary length during the beginning of the deformation process. Large grain boundary area is involved in the deformation of GS 35. From previous discussion (section 5.61), a dislocation is nucleated from a grain boundary in small grains at a certain level of stress. The grain boundary source theory may describe different the initial low-load behavior between small-grained film and large grained films. In our experimental results, the hardness of GS 35 after indentation is larger than those of GS 145 and GS 200, although the soft deformation was initiated. The traditional grain size hardening mechanism was observed in the loading curve of GS 35. From the dislocation source theory, the emission of dislocations and their trapping in the interior of grain lead to the Hall-Petch relationship.

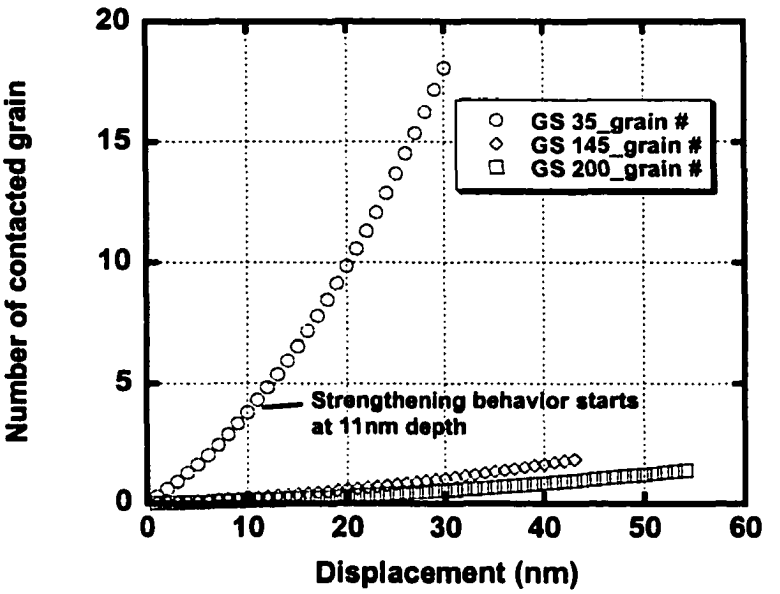

Figure 5.15. Comparison of indented number of grains of GS 35, GS 145 and GS 200 during indentation. Numbers of contacted grains of GS 35 are larger than those of the other films. Hardening mechanism of GS 35 starts at 11 nm displacement, which includes about 4 grains in the deformation.

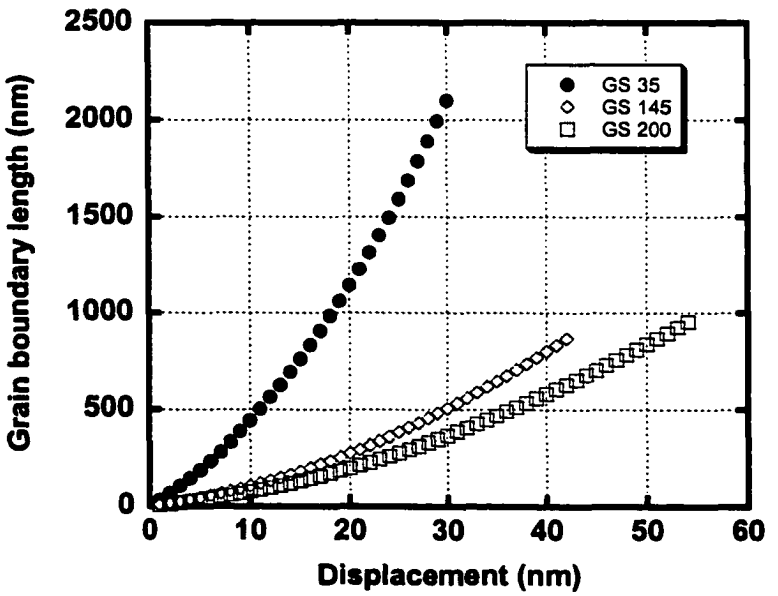

Figure 5.16. Contacted grain boundary length according to indentation depth.

Grain size dependent loading behavior is shown in Figure 5.17. Two loading curves show elastic, soft and hard deformation in a different displacement ranges. Although small-grained film (GS 35) shows the continuous loading curve at the early deformation, the initial loading curve may include several small pop-in behaviors that make the soft deformation of the small-grained films. After soft regime, grain size strengthening mechanism dominates the loading behavior. GS 145 shows three deformation mechanisms; elastic, soft and hard deformations, on the loading curve. GS 35 also shows the three mechanisms on the loading curve, but a very short displacement. All three deformation mechanisms are shown in GS 35 and GS 145. However, GS 200 shows only first two mechanisms due to lack of contacted grain number during the deformation. If limited number of grains are involved in the deformation, the hardening mechanism may not appear because dislocation density is not enough for the strengthening mechanism.

The deformation behaviors of Pt films rely on grain size. The soft deformation and hard deformation account for dislocation density generated from grain boundary and indentation. All loading behaviors of films depend on the microstructure that can generate dislocations during indentation.

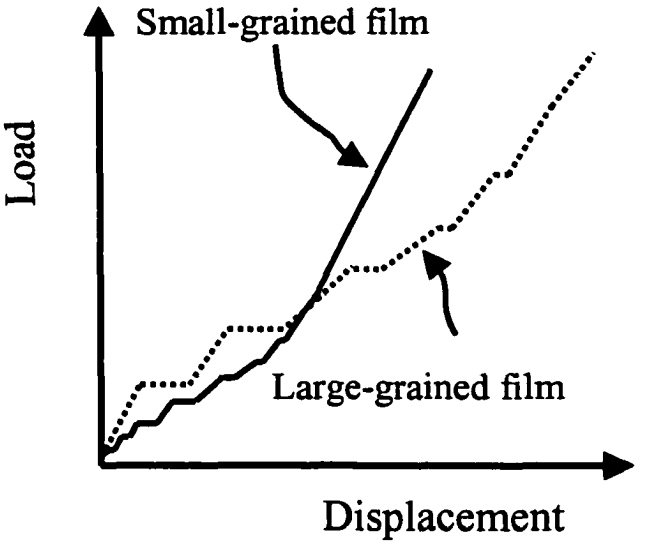

Figure 5.17. Grain size is responsible for the different loading behavior of Pt nanoindentation.

5.6.2 Grain boundary effects (Pop-in event)

As shown in Figure 5.7, this behavior clearly describes the grain boundary effect on the discrete deformation behavior of Pt films. From the grain boundary source theory, the grain boundary acts as a dislocation source. As an indenter tip goes deeper, the grain boundaries provide a lot of dislocations and quickly lead to the hardening mechanism seen in the GS 200gb indentation. Direct force on the grain boundary readily produces nucleation of dislocation and accounts for the strengthening mechanism due to the increase of dislocation density.

Another possible explanation of the two different loading behaviors is that the roughness of the grain boundary area is very high resulting in large contact area, and

therefore led to less total deformation of GS 200gb. The indenter tip may not completely touch the boundary area at the initial loading because the grain boundaries are grooved. If this is true, the pressure of the tip was dissipated due to its contacts with several surrounding grains during the indention. However, the 200nm thick film (GS 145) also showed the similar loading behaviors, and less roughness is expected on its surface. Thus, the indenter tip on GS 200gb probably delivers direct force on the contact area, and roughness can be discounted as the cause of the apparent hardening.

The two loading behaviors of GS 200c and GS 200gb may be discussed as the different deformation behaviors of single crystal material and polycrystal material. The deformation of GS 200c contacts only one single grain, whereas GS 200gb covers a few grains during indentation. Single grain deformation may act like single crystal behavior. The early deformation of GS 200c may follow the single crystal deformation mechanism such as easy glide [Hirth 1982] while GS 200gb can show harder deformation behavior because the several slip systems in polycrystals suppress the easy glide.

If we remove the pop-in behavior in GS 200c, the loading curves of GS 200c and GS 200gb are very similar to each other as shown in Figure 5.18. This result implies that grain boundary proximity impedes pop-in behavior and only a defect-free crystalline material can produce the discrete deformation loading behavior. The loading curve between pop-ins was explained as an elastic response of a single crystal [Gouldstone et al. 2000]. But in this study, the loading behavior right after each pop-in event can be explained as an elastic-plastic deformation due to the grain boundary effect.

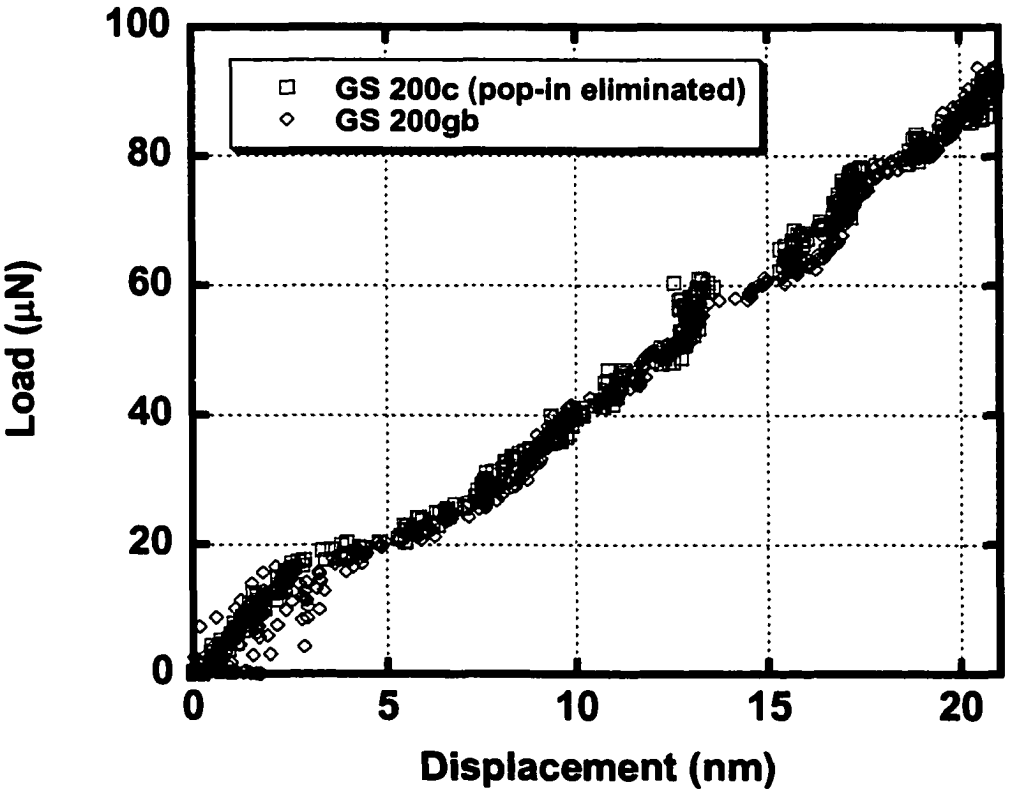

Figure 5.18. GS 200c and GS 200gb loading curves without pop-in behavior of GS 200c. The loading behaviors of two samples are almost identical without pop-in behavior.

Figure 5.19 illustrates grain boundary effects on dislocation density. If the indenter tip deforms the grain boundary area, large numbers of dislocations can be generated because the grain boundary acts as a dislocation source. Microplastic incompatibility effects are also possible because of the discontinuous nature of slip. A slip band can impinge on a grain boundary. High dislocation density due to secondary slip dislocations can be generated during indentation on a grain boundary. Indentation on the interior of a grain causes a relatively low dislocation density, and results in discrete deformation behavior.

Figure 5.20 illustrates load-displacement curves of Pt films according to the grain boundary deformation. At the initial loading portion, only elastic deformation dominates the loading behavior. After elastic response, discrete deformation behavior starts. Large pop-in behavior is observed during indentation(a). However, if indentation includes grain boundary area, grain boundary deformation induces large dislocation density resulting in high hardness and less pop-in events(b).

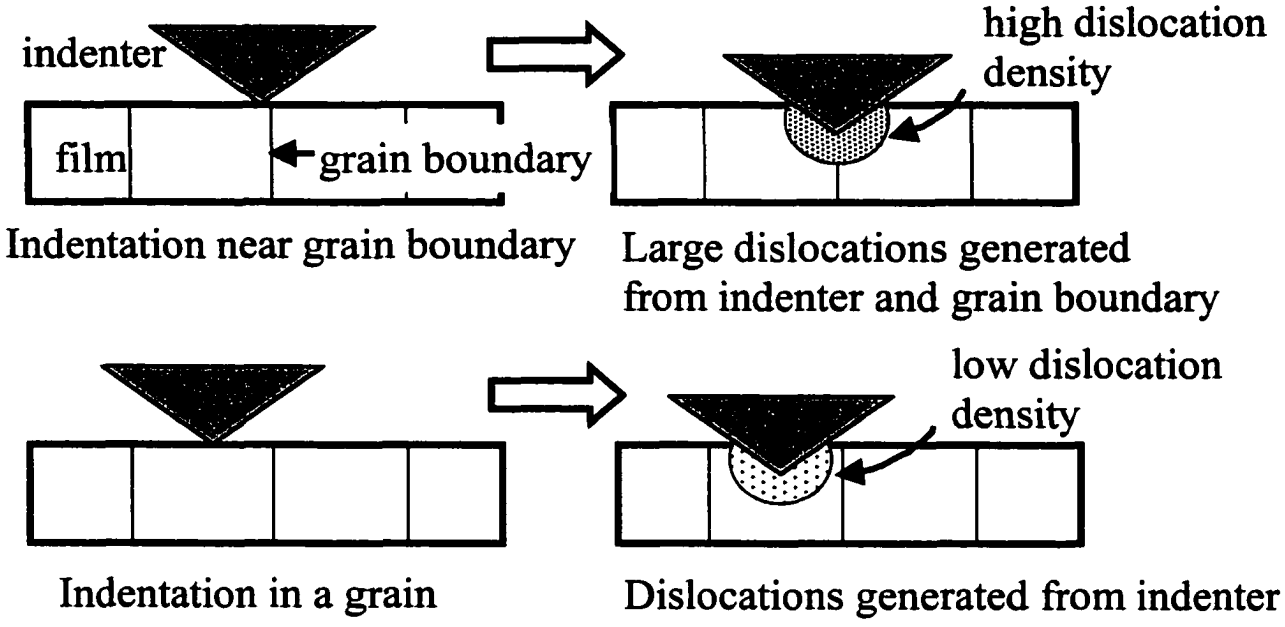

Figure 5.19. Grain size effects on dislocation density. High dislocation density is expected on grain boundary indentation. Single grain deformation may follow single crystal deformation while grain boundary indentation shows polycrystalline deformation.

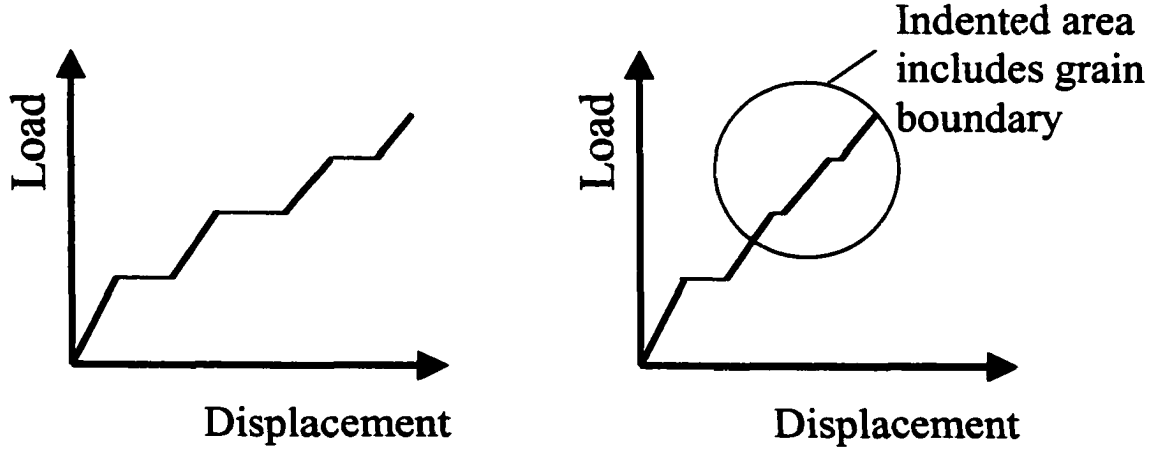

(a) indentation in the middle of a grain

(b) indentation near grain boundary and grain boundary deformation starts as displacement increases

Figure 5.20. Schematic diagram of load-displacement curves. Loading behavior depends on microstructure of indented area.

From hardness versus displacement curves of GS 35, GS 145 and GS 200 (Figure 5.6a), GS 200 shows high strength at the low depth whereas GS 35 shows low hardness. However, hardness increase is observed at the large displacement of GS 35, and hardness decrease is shown in GS 145 and GS 200. Hardness increase in GS 35 is explained by the Hall-Petch mechanism. The transition from elastic deformation to plastic deformation and low dislocation density in the indented area due to large deformation volume under the indenter may account for hardness decrease in GS 145 and GS 200. However, GS 145 also shows the hardness increase at the end of the loading curve. Hardness increase shows high dislocation density because several grains are involved in the deformation.

Figure 5.21 represents the loading behavior of Pt film according to grain boundary deformation. Elastic deformation at the initial loading shows high hardness, and pop-in behavior is responsible for the soft deformation. The soft region represents easy deformation, as shown in the GS 35 loading curve, at the early part of GS 35 and in the GS 145 loading curve right after elastic deformation in Figures 5.4 and 5.5. In the soft region, only a small amount of grain boundary area or no grain boundary area is involved in the deformation. After soft deformation, the hardening mechanism appears due to several grain deformations. The hard region includes large grain boundary deformation area resulting in hard hardness.

5.6.4 Strain gradient effects

The effect of spherical indenter on strain gradient plasticity is shown in Figure 5.22. Although spherical indenter effects is included in the strain gradient model, the model does not predict hardness behavior of GS 35 with increasing displacement.

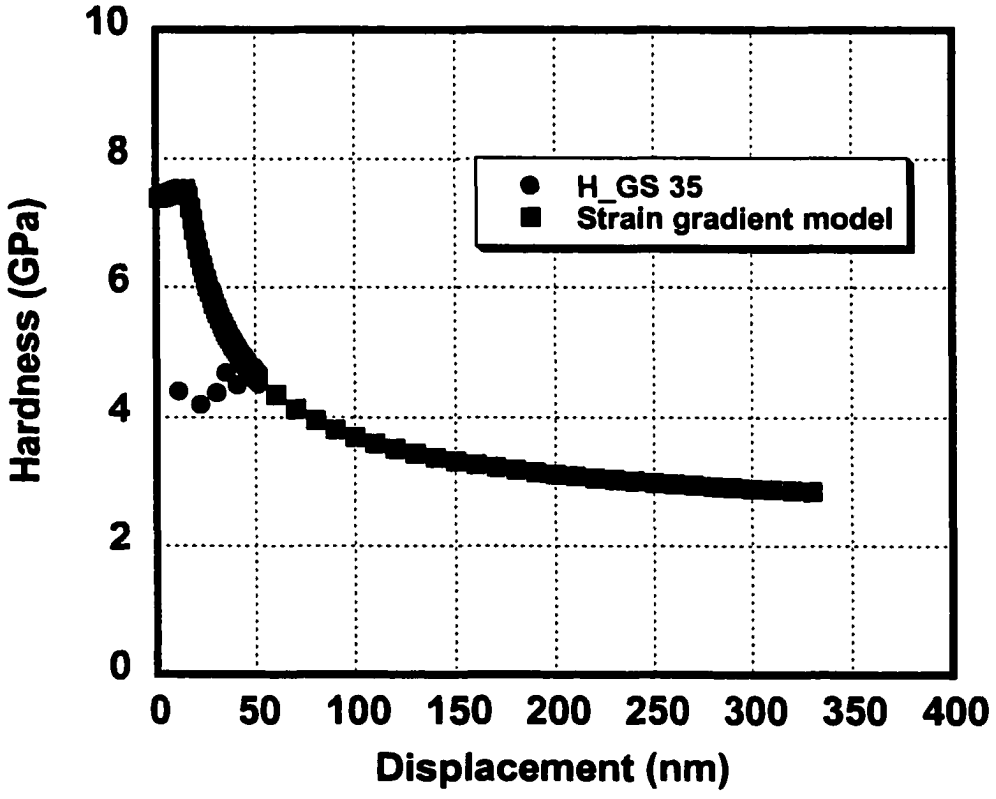

Figure 5.22. Comparison of strain gradient model (spherical indenter at very shallow displacement (up to 14nm) and berkovich indenter) and measured hardness of GS 35.

The grain boundaries that are involved in GS 35 deformation may produce large numbers of dislocations. Thus, the strain gradient model that predicts lower dislocation density with increasing indentation depth can not be applied to the small-grained film of GS 35. Instead of the geometrically necessary dislocation density (ρ_G), the statistically necessary dislocation density (ρ_s) dominates the behavior of GS 35.

5.6. Summary

We have investigated loading behavior of three Pt films in terms of grain size and grain boundary. Pt films have unique loading behavior according to grain size. Elastic-plastic transition occurs at near theoretical stress in GS 200 (large grained film) through a large pop-in event. In contrast, the loading curve of GS 35 appears to be continuous. Immediate inelastic deformation behavior occurs on the low load-displacement curve. At large displacement, deformation of Pt films follows the Hall-Petch relationship (grain size strengthening mechanism). However, low hardness of small grained films is observed at small displacement. The grain boundary source theory [Lilleodden et al. 2001, Yamakov et al. 2001] may be responsible for the soft behavior of small grained film. The grain boundary plays an important role on loading behavior of Pt films. Pop-in behaviors of Pt films are affected by the presence of a grain boundary in the indented area. Large discrete deformation behaviors (pop-in events) were observed when a single grain was indented whereas less pop-in events were observed if an indentation was performed near or on the grain boundary area. Higher load is required for the deformation of GS 200gb (grain boundary indentation). Grain boundary deformation is responsible for the high hardness of Pt film. When the indentation size is similar to the inhomogeneous

Ch. 6 Effects of alloying on low temperature flow stress behavior

6.1 Introduction

Plastic deformation of metals can be controlled by a variety of dislocation strengthening mechanisms. The flow stress of a bulk metal is determined by the propagation of dislocations through the structure of the material. The flow stress of metallic thin films also depends on dislocation motion. However, the mechanical behavior of metal thin films is very different from that of bulk metals. In the most cases, the flow stress of a film is much higher than that of the same bulk material. The strengthening of thin films has been explained on the basis of small grain size and dimensional constraints on dislocation motion [Nix 1989, Venkatraman et al 1992, Keller et al. 1998].

Systematic work regarding detailed strengthening mechanisms of metallic thin films is required to understand the deformation mechanisms. Moreover, the mechanical properties of solid solution thin films have not been heavily studied. Thus, the flow stress behavior of alloy films is a worthwhile area for investigation.

In this work, the flow stress of Pt and Pt-Ru thin films measured by the wafer curvature method and nanoindentation technique was studied. Pt-Ru alloy films in the composition range of 0 to 20 Ru wt% were prepared. The flow stress behavior of the alloy films was explored to examine the relative importance of various strengthening mechanisms. The strengthening contributions of dimensional constraint, grain size effect

and solid solution effect were systematically investigated. Finally a comparison of two different hardness values obtained from two unique test methods, nanoindentation and wafer curvature, were examined. A discrepancy between the two results is explained by modifying the Tabor equation [Tabor 1951].

6.2 Sample preparation

The films used in these experiments were Pt and Pt-Ru alloy thin films (type 1 films). The thickness of each film was about 200 nm. Alloys of 1,2,5,10 and 20 wt % Ru were fabricated for the flow stress measurements. The detailed fabrication procedures are described in Chapter 3.

Two techniques, nanoindentation and wafer curvature, were used to measure the flow stress of Pt and Pt-Ru thin films. For the wafer curvature measurement, the films were thermocycled up to 800°C in N_2 atmosphere. Indentations were performed on as-deposited Pt and Pt-Ru films. A maximum load of 200 μN with a Berkovich tip was used for the nanoindentation measurements. The detailed experimental conditions are described in Chapter.3.

6.3 Stress measurement using Stoney equation

. Thin film stress can be measured from the radius curvature change of the substrate. With a thin film deposited on a substrate, intrinsic stress in the film may deform the substrate. Also, heating and cooling of the film-substrate composite can result in residual stress due to different coefficients of thermal expansion of the film and the substrate. A stress-strain relationship for the film can be found from this deformation.

Stoney [Stoney 1909] originally derived the relationship between the stress and the curvature change of the film-substrate system. There are several basic assumptions behind the stress derivation from the curvature change. First, the substrate is uniformly thick, elastic, homogeneous and the radius of the substrate is very large. Second, the thickness of the substrate is much larger than that of the thin film. Third, there is a neutral plane where no stress exists at the midpoint of the substrate at $t_s/2$. The sum of the moments and the sum of the forces are zero at this point. Figure 6.1 shows the beam-bending theory to derive the stress-curvature relationship. For pure bending of the film-substrate system, F_f is a force on the film per unit width defined by

$$F_f = \sigma_f t_f \quad (6.1)$$

The moment (force times perpendicular distance) on the substrate exerted by the film is

$$M_f = \int_0^{t_s/2} F_f dy = \int_0^{t_s/2} \sigma_f t_f dy = \sigma_f \frac{t_f t_s}{2} \quad (6.2)$$

The substrate stress is defined by

$$\sigma_s = \frac{E_s}{1-\nu_s}\varepsilon_s \quad (6.3)$$

where E_s is the Young's modulus of the substrate, and ν_s is the Poisson's ratio of the substrate. The strain in a plane that is parallel to and at a distance of y from the neutral plane can be expressed as

$$\varepsilon_s = \frac{y}{r} \quad (6.4)$$

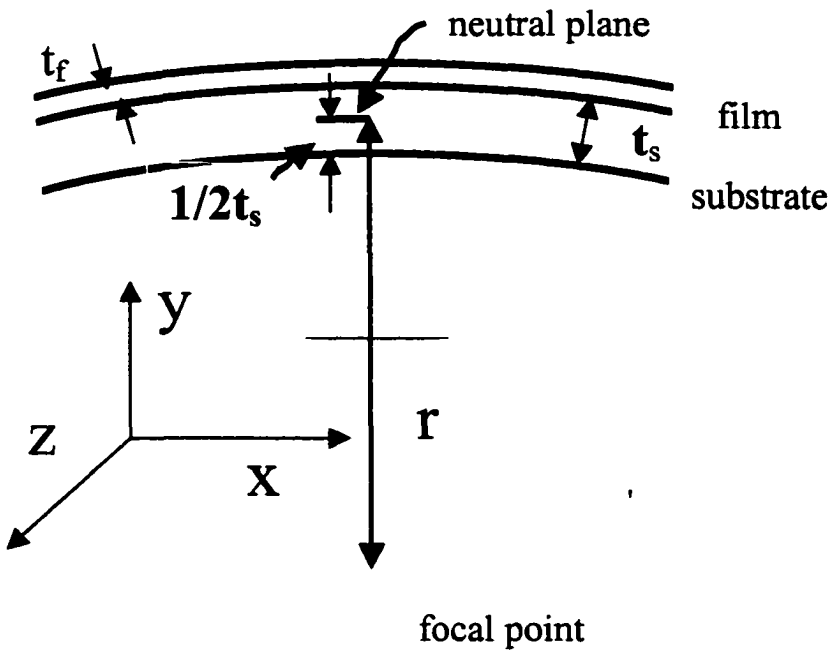

Figure 6.1. Schematic diagram of thin film and substrate system. The substrate thickness (t_s), thin film thickness (t_f), and the radius of curvature (r) of the system are defined. [Murarka 1993]

The moment of the substrate is defined by

$$M_s = \int_{-t_s/2}^{t_s/2} \sigma_s y dy = \int_{-t_s/2}^{t_s/2} \frac{E_s}{r(1-\nu_s)} y^2 dy = \frac{E}{3r(1-\nu)} \frac{t_s^3}{4} \quad (6.5)$$

by equating Equation 6.2 and Equation 6.5 relationship, Stoney's equation can be obtained.

$$\sigma_f = \frac{E_s t_s^2}{6(1-\nu_s) r t_f} \quad (6.6)$$

6.4 Results and Discussion

6.4.1 Hardness and flow stress data from wafer curvature and nanoindentation methods

The flow stresses of Pt and Pt-Ru thin films were obtained from nanoindentation and wafer curvature methods. The stress-temperature curves measured with the wafer curvature technique are shown in Figure 6.2. The indentation loading behavior of Pt and Pt-20wt%Ru films are shown in Figure 6.3. The AFM images after indentation are also shown in Figure 6.4. The flow stress and hardness according to Ru wt% are represented in Figure 6.5. The flow stress increases with Ru content from both measurements. The flow stress from the wafer curvature method is in the range of 839 MPa to 1720 MPa. It should be noted that the flow stress value of the Pt-2wt%Ru film shows a lower value than the ones of other Ru alloy films. This is because of the different thermal cycling conditions of the Pt-2wt%Ru film. Air was accidentally introduced in the wafer curvature measurement during thermal cycling. Ru is expected to oxidize at high temperature, and this may have caused the unusual flow stress value of the Pt-2wt%Ru film. The hardness of Pt and Pt-Ru films measured by nanoindentation are in the range of 5.1 GPa to 8.5 GPa. In the following sections, a model for the flow stress is developed and compared to the wafer curvature measurements. Then the wafer curvature results are compared to the nanoindentation measurements.

6.4.2 Dimensional constraint

A model that describes the dislocation interaction with the film interfaces has been developed by Nix [Nix 1989] and Freund[Freund 1987]. The model is described in Chapter 2. If the film has no passivation layer on the surface, the minimum stress for yielding is given by [Nix 1989]

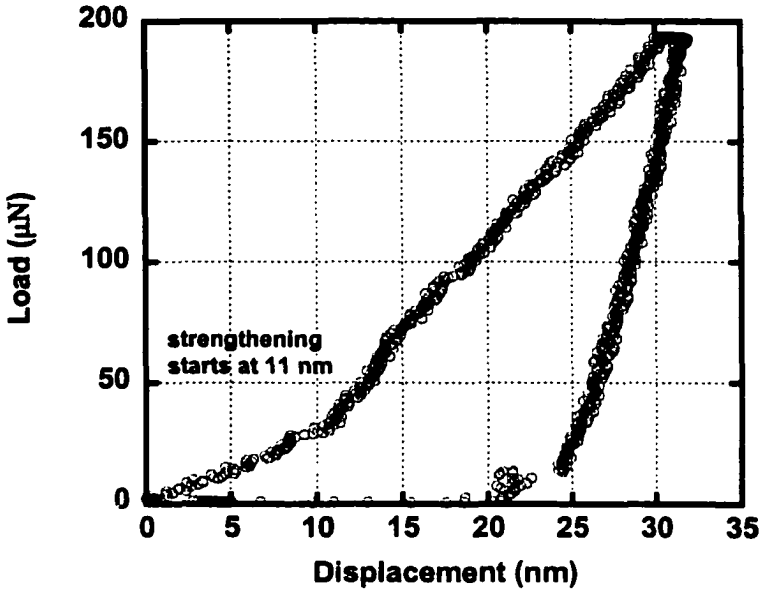

(a) Pt as-deposited film

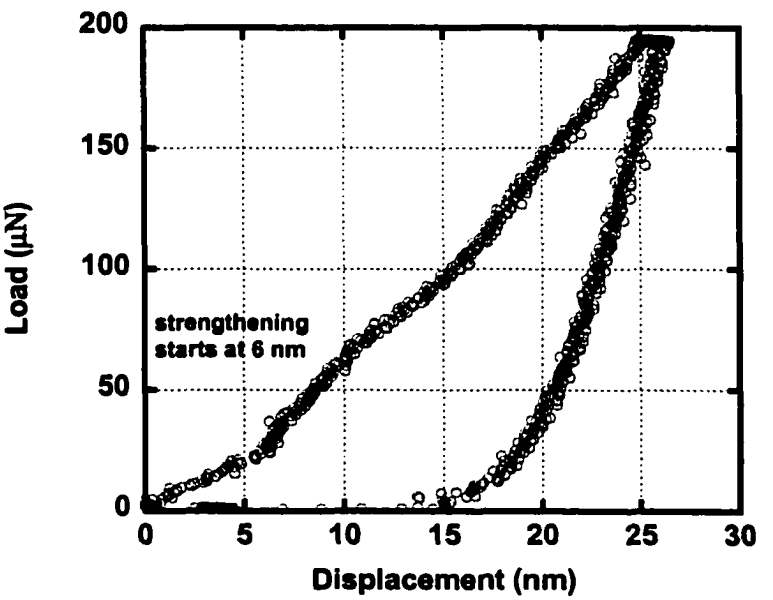

(b) Pt-20wt%Ru as-deposited film

Figure 6.3. Load-displacement curves of Pt and Pt-20wt%Ru thin films. Higher load is required for the deformation of the Pt-20wt%Ru film compared with the Pt film. In the loading curve of the Pt-20wt%Ru film, the strengthening behavior is observed earlier compared with the Pt film.

(a) Pt film

(b) Pt-20wt%Ru film

Figure 6.4. AFM images of indented area of as-deposited films. The indentation size in the Pt film is larger that that in the Pt-20wt%Ru film. The high strength of Pt-20wt%Ru is evident.

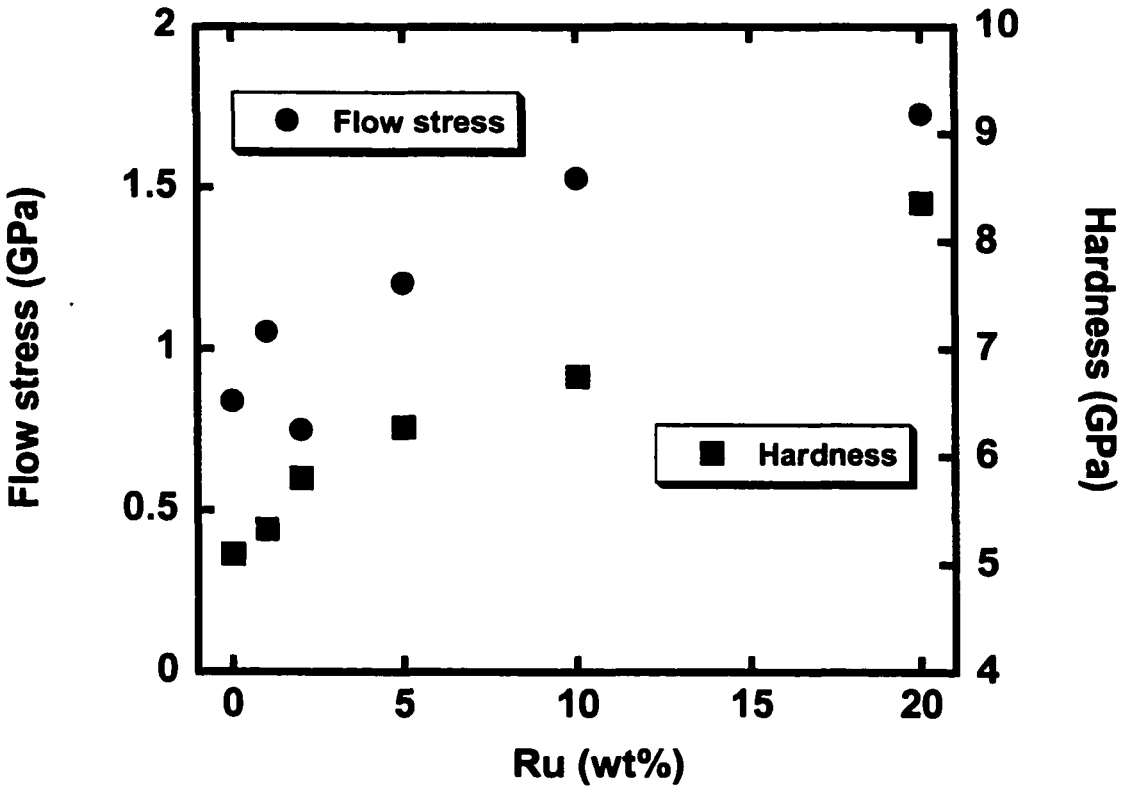

Figure 6.5. Flow stress and Hardness of Pt and Pt-Ru thin films. The flow stress was obtained from the wafer curvature method while the hardness was measured by nanoindentation technique. The flow stress is in the range of 839 MPa to 1,720 MPa according to Ru wt%, and the indentation hardness also increased from 5.09GPa to 8.5 GPa with Ru additions.

Figure 6.7 compares the flow stress of the Pt and Pt-Ru films predicted from the Nix equation to those from experimental measurement. The measured flow stress is significantly higher than the predictions of the Nix equation. The predictions of flow stress are in the range of 229 MPa to 247 MPa. The parameters for this evaluation are listed in Table 6.1. Although the calculation predicts a slight increase of flow stress with Ru wt%, the change in the measured flow stress of the films is much higher than predicted from the Nix model. To estimate the difference of the flow stresses between the Nix equation and measured flow stress of the Pt-Ru films, the measured flow stress and calculated flow stress are normalized by the effective modulus (Equation 6.7). The graph of normalized stress against Ru additions is shown in Figure 6.8. The normalization removes the effect of alloying from the Nix calculation, which only describes the dimensional constraints on the flow stress. Although the normalized values calculated from the Nix equation are almost constant with Ru wt%, the measured stress rapidly increases with increasing to Ru content.

From this model, the yield strength of the film depends inversely on the thickness of the film. As a single threading dislocation moves in a slip plane of the film, a dislocation is created along the film-substrate interface. The work required for the creation of the dislocation at the interface is provided from the applied stress. However, the model predicts much lower values of the flow stress than the ones measured from the experiments. The energy balance model (Nix model) underestimates the flow stress of films because the movement of only a single dislocation is considered. Also, no obstacles to dislocation motion or grain size strengthening have been considered in this model. It is

clear from the comparison of model and experiment that additional strengthening mechanisms influence the deformation behavior of the Pt-Ru films.

Table 6.1. The parameters and relations for the flow stress calculation.

Parameter	Symbol	Value	Parameter	Symbol	Value
Burger's vector	b	2.77~ 2.753×10^{-10}m	Poisson's ratio	ν	0.39~0.3658 [Zinov'yev 1984]
Shear modulus	μ_f Film μ_s Substrate	60.6~75.77GPa 66.5GPa [Zinov'yev 1984, Nix 1989]	Grain Size	d	29.2~36.5 nm
Constants	B	0.9025~0.9085	Hall-Petch Constant	K	0.18 MPa $m^{1/2}$ [Huang 2000]
	βs	0.829~0.834 [Venkatraman 1992]			
	$\frac{\sin\phi}{\cos\phi\cos\lambda}$	3.464 [Sanchez 1992]	Line tension	E_L	$1/2\mu b^2$ [Haasen 1996]
Thickness	h	200nm	Constant	A	0.7

Solute atom distance from a slip plane	z $\frac{b}{\sqrt{6}}$ [Haasen 1996]	
Obstacle strength	$K \approx \frac{2E_L}{10} \approx \mu b^2 \sqrt{\delta^2 + \eta^2 \beta^2}, \beta \approx \frac{1}{20}$ $\eta \approx \frac{1}{\mu}(\frac{d\mu}{dc})$, c : Solute atom content Misfit parameter, $\delta \approx \frac{1}{a}\frac{da}{dc}$, a : Lattice parameter [Haasen 1996, Cahn 1996]	

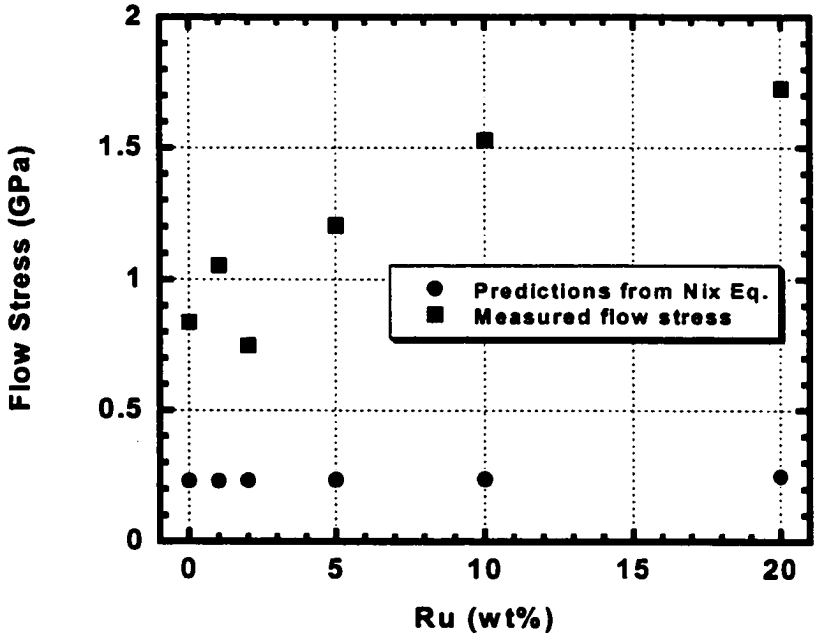

Figure 6.7. Comparison of measured flow stress and calculated flow stress. The flow stress was measured from the wafer curvature method and calculated from the dimensional constraint mechanism given by Equation 6.7.

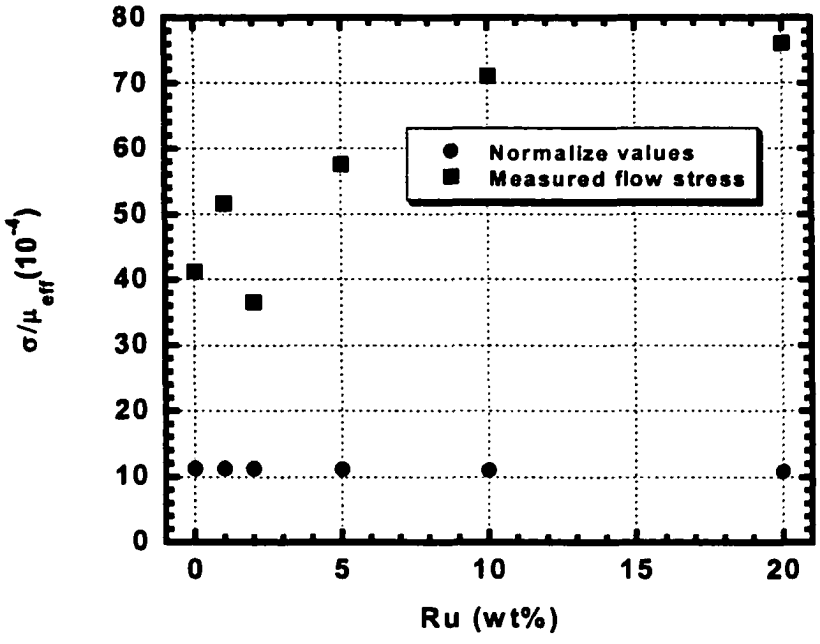

Figure 6.8. Flow stress is normalized by the effective modulus.

6.4.3 Grain size strengthening

The effect of grain size on the flow stress of metals is a well known strengthening mechanism at low temperature. The grain size effects are often described by the Hall-Petch relationship, which is based on the proposition that plastic deformation involves glide of dislocations that can pile up at a grain boundary. The stress concentration of the pileups at a grain boundary assists the propagation of slip from a grain to its neighbor. The grain boundary contribution to strengthening can be defined by

$$\sigma_{gs} = kd^{-1/2} \qquad (6.8)$$

where d is the grain diameter and k is the Hall-Petch coefficient.

To the best of our knowledge, Hall-Petch coefficient has not been determined experimentally for Pt, so our value was obtained via calculation: 0.18 MPa-$m^{-1/2}$ [Huang et al. 2000]. The theoretical value of the coefficient is given by

$$k = 0.18\mu\sqrt{b} \quad (6.9)$$

where μ is the shear modulus and b is the Burgers vector of a dislocation in the Pt film. The value of $\mu\sqrt{b}$ is 1 for Platinum.

The strength of the film can now be described by the sum of Nix equation, σ_h, (dimensional constraint) and the Hall-Petch equation, σ_{gs}, (grain size strengthening) [Venkatraman 1992], which is given by

$$\sigma_{flow} = \sigma_h + kd^{-1/2} \quad (6.10)$$

This equation assumes that the stress required for dislocation motion is constrained by the substrate, proportional to inverse film thickness, and the movement of a dislocation is also impeded by the grain boundary simultaneously.

The grain size strengthening mechanism can be obtained from Equation 6.8. The average grain sizes of Pt and Pt-Ru films are in the range of 100 to 46 nm, and the average grain size versus Ru wt % is shown in Chapter 4.

To estimate the grain size strengthening effects on the Pt and Pt-Ru films, the stresses due to dimensional constraints and the Hall-Petch equation are represented in Figure 6.9. The measured flow stress of Pt is 838 MPa and the expected flow stress from Equation 6.10 is 798 MPa. Although the grain size strengthening mechanism predicts an increase of flow stress with Ru wt%, the difference of the stress values between the measured flow stress and predicted flow stress is large. If we change the Hall-Petch

constant for the Pt thin film from 0.18 MPa-$m^{-1/2}$ to 0.297 MPa-$m^{-1/2}$, the predicted flow stress can nicely fit to measured flow stress at high Ru content, (5, 10, and 20 wt% of Ru in Pt matrix film). However, the flow stress of pure Pt is much lower than that of predicted Pt from the modified Hall-Petch equation as shown in Figure 6.10. So simply using a larger K value is not enough to fully account for the observed strength. Figure 6.11 shows hardness of as-deposited and annealed films. The hardness values of as-deposited films are larger than those of annealed films. The effect of grain size on hardness is clearly observed.

Some evidence has showed that the grain size strengthening term does not follow the traditional Hall-Petch relationship exactly. The values of the Hall-Petch coefficient for aluminum and copper thin films are approximately twice the common bulk values for those metals [Venkatraman et al. 1992, Keller et al. 1998]. Venkatraman [Venkatraman et al. 1992] explained that the flow stress behavior of Al thin films may depend on 1/d instead of $d^{-1/2}$. However, 1/d dependence in grain size strengthening term is not applicable for Pt and Pt-Ru thin films. The stress of grain size strengthening from 1/d dependence is much higher than that of measured flow stress. The Hall-Petch relationship describes the strengthening mechanism of bulk materials with various grain sizes well [Hansen et al. 1977, Hughes et al. 1986]. From the calculated value of Equation 6.10, it appears that the grain size strengthening mechanism should strongly contribute to the flow stress of the films due to small grain sizes associated with Ru additions. Although grain size strengthening term can predict some of the flow stress increase according to Ru wt%, the Hall-Petch relationship cannot fully predict the flow stress behavior exactly.

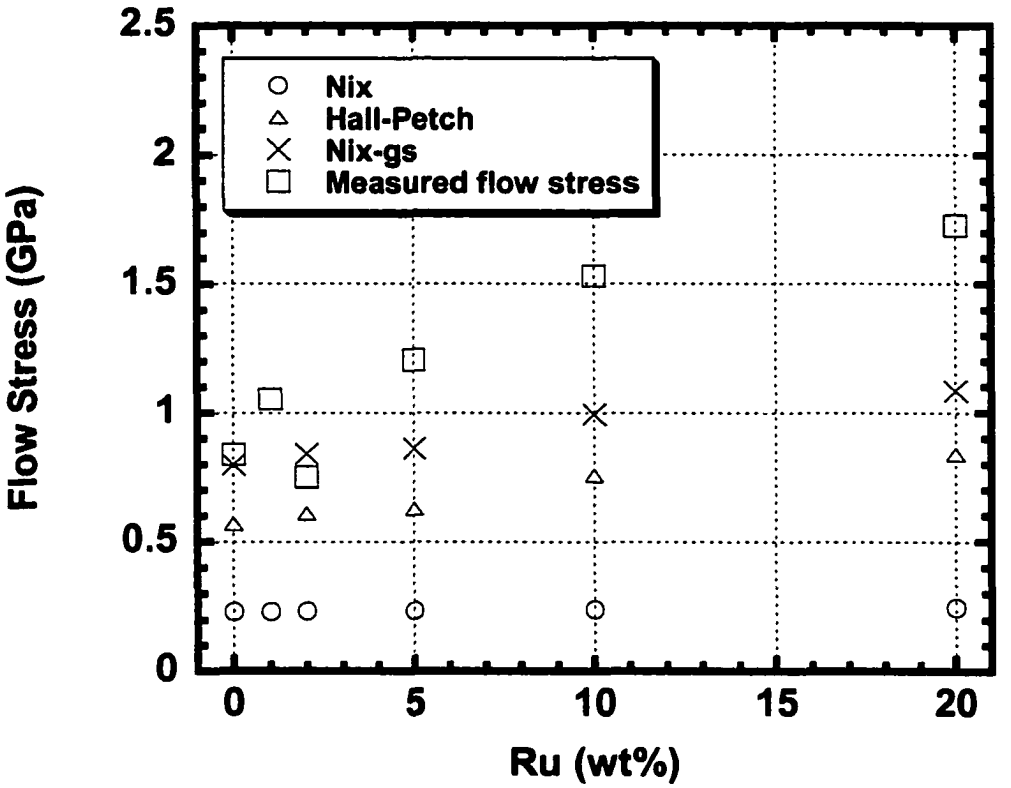

Figure 6.9. Comparison of measured flow stress and calculated flow stress from Equation 6.10. The pure Pt flow stress well predicts with calculation of the simple model, including dimension constraints and microstructure constraints strengthening mechanisms. However, high Ru wt%-Pt films show higher flow stress than the ones from the model, Equation 6.10

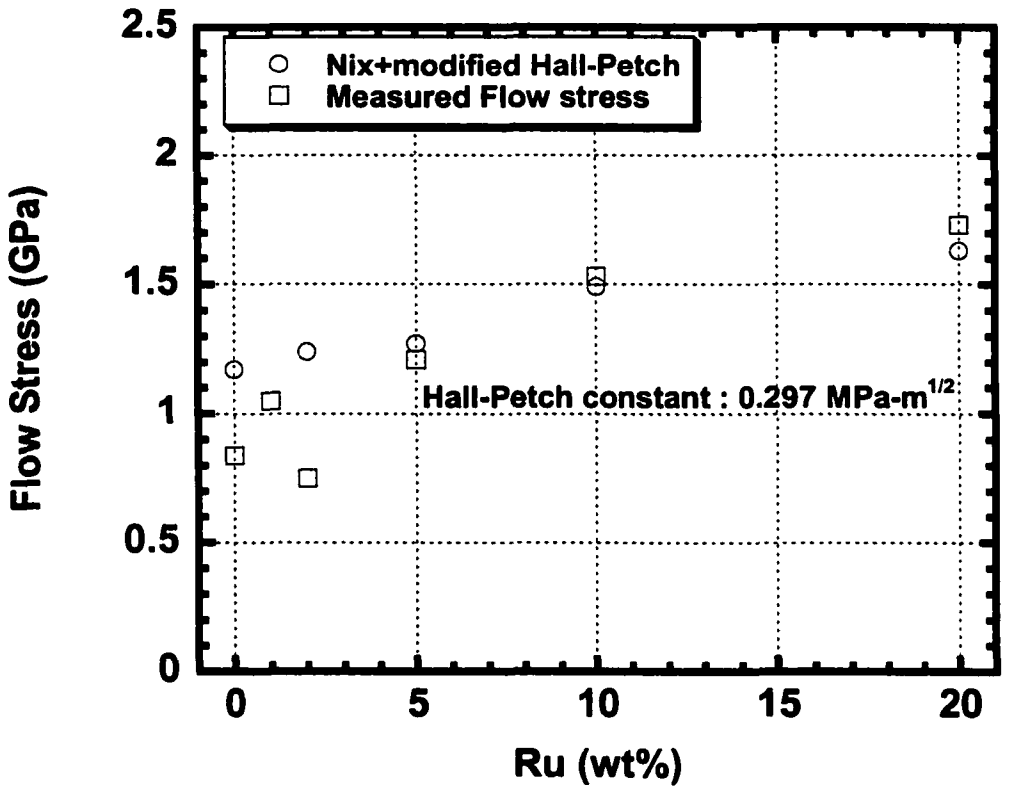

Figure 6.10. Flow stress of Pt-Ru thin films according to Ru wt% is shown. The high Hall-Petch constant, 0.297 instead of 0.18 was used for the calculation. Although the measured flow stress and calculated flow stress represent good agreement according to Ru increase, the predicted flow stress of pure Pt is much higher than the measured value.

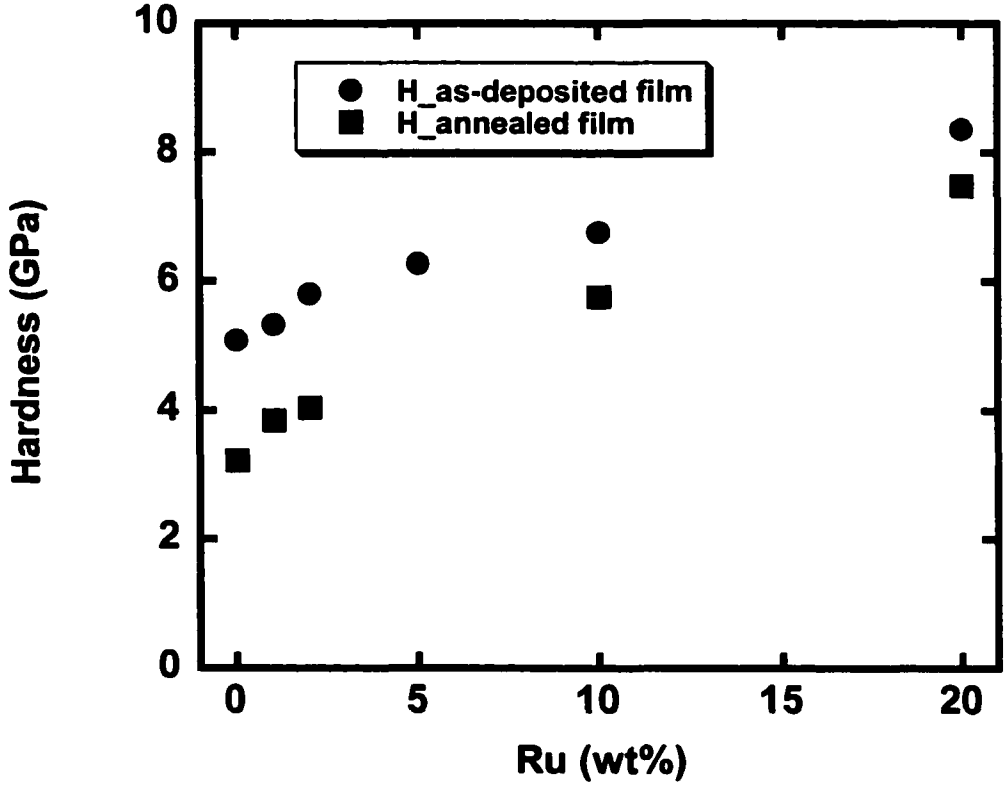

Figure 6.11. Grain size effects on hardness. Hardness is measured from nanoindentation method. Annealed films were thermocycled up to 800°C. The hardness values of as-deposited films are larger than those of annealed films.

adjusted for this equation. This model was originally designed by Labusch [Labusch 1970]. Our version of the equation, along with its parameters, is simplified for FCC solid solution strengthening following Haasen [Haasen 1996]. The parameters and relationships for the calculation are listed in table 6.1. The total flow stress including solid solution strengthening mechanism is shown by

$$\sigma_{flow} = \sigma_h + \sigma_{gs} + \sigma_{ss} \quad (6.12)$$

As shown in Figure 6.12, the calculated flow stress increases from 799 MPa to 1840 MPa with Ru wt% increase. The agreement with the measured results is very reasonable, considering the simplicity of the modeling approach. The calculated flow stresses and experimentally measured flow stresses of Pt-Ru thin films show the importance of the solid solution hardening effect. The dimensional constraint mechanism and grain size strengthening mechanism do not show large changes with the increase of Ru. In contrast, the solid solution strengthening model predicts a significant increase in strength similar to the increase that was measured. This result supports the conclusion that solid solution alloying can significantly increase the strength of thin metal films over a wide range of solute content. It is possible that the solute may also affect work hardening, but this potential contribution cannot be easily evaluated.

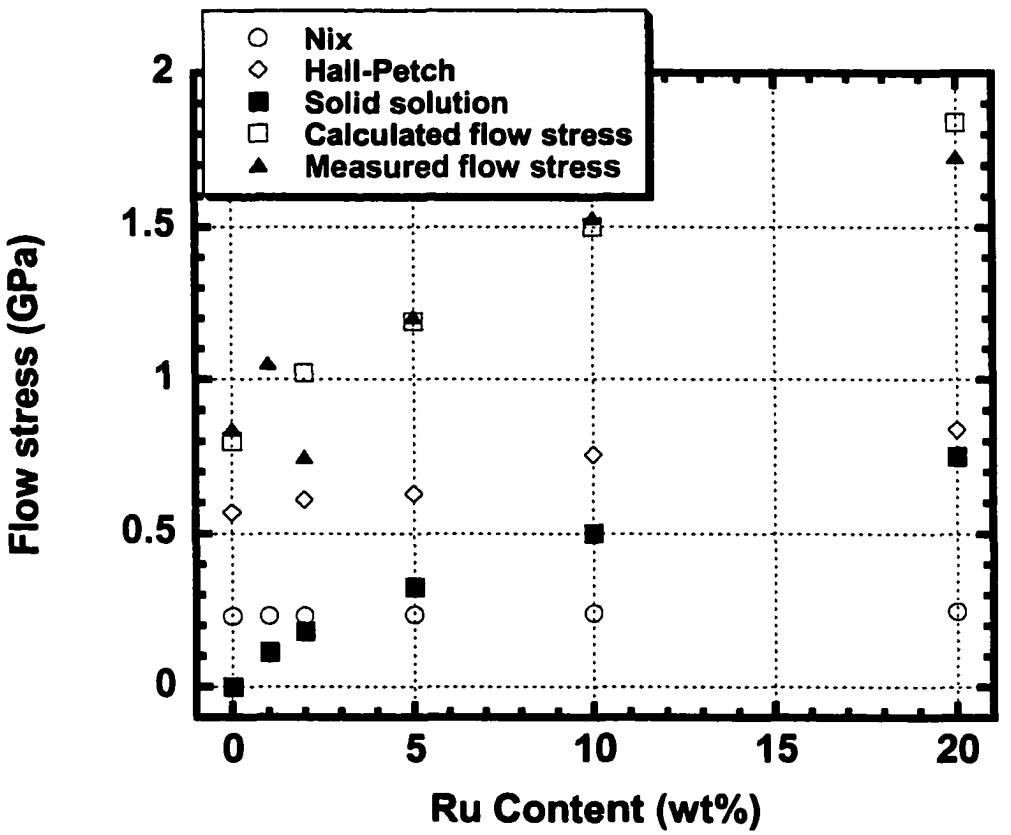

Figure 6.12. Comparison of measured flow stress from wafer curvature method and calculated flow stress from Equation 6.12 that includes film thickness, grain size and solid solution strengthening mechanisms. The calculations from Equation 6.13 well predict the flow stress changes with Ru wt%. The solid solution strengthening is a dominant hardening mechanism in Pt-Ru films.

6.4.5 Comparison of nanoindentation and wafer curvature results

Flow stress obtained from the wafer curvature method is often converted to hardness using the Tabor relationship [Tabor 1951].

$$H = 3\sigma \quad (6.13)$$

Figure 6.13 shows Hardness changes with Ru increase measured from nanoindentation and predicted from wafer curvature measurements. Measured Hardness values from nanoindentation are a factor of two higher than those from wafer curvature technique. The different hardness values from nanoindentation and wafer curvature method might come from several discrepancies between the two techniques and sets of samples. First, indentation size of nanoindentation may influence the flow stress. Several researchers reported a size dependence of the measured hardness when the indentation size is small [Nix 1998, Ashby 1970, Ma 1995]. As indentation size increases, hardness decreases, especially in the range of sub-micrometer depth. Strain gradient theory of the plasticity was introduced to describe the size dependence hardness. From the strain gradient plasticity, the geometrically necessary dislocations during indentation determine the flow stress, and the dislocation density of geometrically necessary dislocations is proportional to the inverse of the indentation depth [Nix 1998]. So small indentation area contributes to a higher value of the hardness. However, in Chapter 5 it is demonstrated that this is not a significant factor in small-grained films. In the present nanoindentation study, pre-existing residual stresses may affect the plastic deformation. The residual stresses of indented specimens (as-deposited films) are compressive, which is measured from the wafer curvature technique as shown in Figure 6.2. The compressive stress may change the flow stress level. For instance, the tensile residual stress in the film adds to the

magnitude of the shear stress that is introduced by indentation because the tip of indenter applies a compressive force on the film. The plastic deformation of the film depends on the shear stress, thus tensile residual stress in the film contributes to the onset of plastic deformation. The compressive residual stress may affect the plastic deformation in the opposite way. Tsui [Tsui 1996] introduced traditional hardness data for the Rockwell B hardness on a high carbon steel bar to demonstrate the residual stress effect on hardness. Although the tensile and compressive stress in the material affects hardness, the effect of residual stress is small. Tsui [Tsui 1996] also reported the effect of an residual stress on hardness behavior of aluminum alloy were measured by nanoindentation. However, after re-evaluating the contact area by optical measurement, hardness of the specimen was consistent over the range of residual stress. Hardness is therefore most likely to be independent of residual stress. Another possible reason for the different values from nanoindentation and wafer curvature method is that the nanoindentation experiments are performed at room temperature, but the wafer curvature method introduces large thermal cycling to apply the force on the film. At high temperature, inelastic deformation such as diffusional mechanisms, arises as described in Chapter 7. The inelastic deformation, which is dependent on the microstructure and the thickness of films, may influence the yield stress of the films after or during thermal cycling [Kobrinsky 1998]. However, in our wafer curvature results, this is not a significant factor.

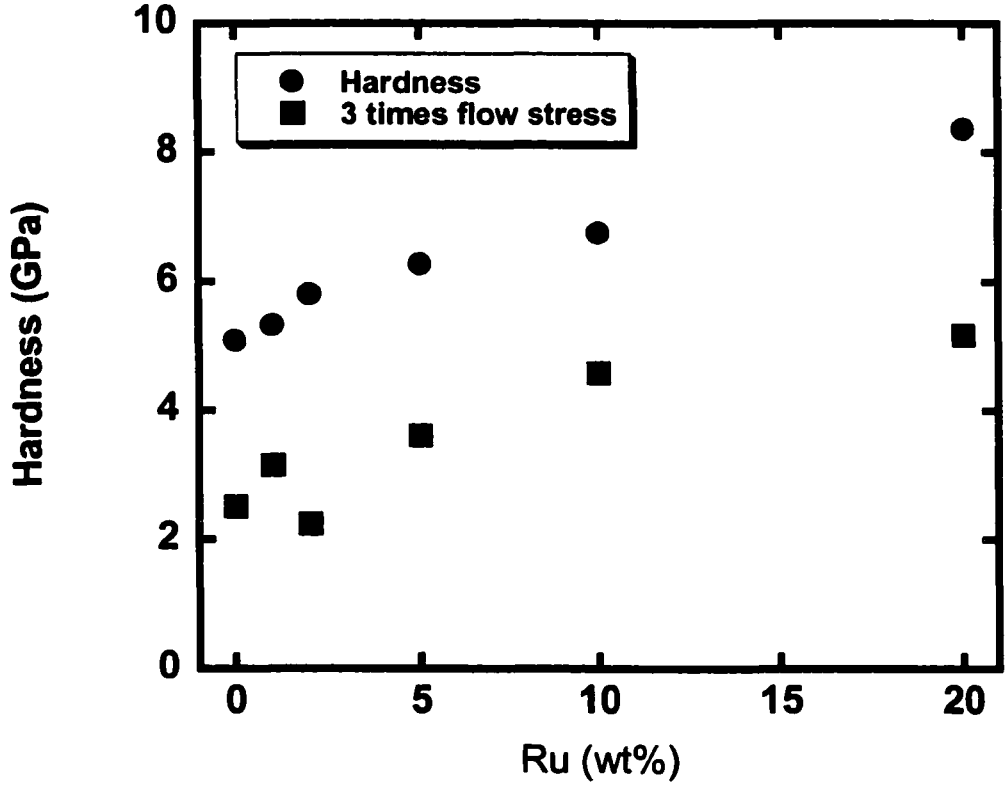

Figure 6.13. Hardness of Pt and Pt-Ru films from two test methods. Two different hardness values, which were measured from nanoindentation (circle) and wafer curvature method (square), are shown. The hardness values measured from wafer curvature method are obtained from the Tabor relation, Equation 6.13

Finally, the microstructure difference is one of the main reasons for the higher hardness from nanoindentation than the ones from the wafer curvature method. The average grain sizes of the films after heating up to 800 °C are larger than those of the as-deposited films. The grain size strengthening mechanism may contribute to the high hardness in as-deposited films. However, the grain size strengthening can not fully explain the large difference between hardness values from the two test methods. We can evaluate the grain size effects on hardness because the flow stress model described in the previous sections, Equation 6.12, includes a grain size hardening term and the model very well predicts the flow stress behavior according to Ru wt%. However, after we take into account the grain size change in hardness calculation, the large difference between the measured hardness and calculated hardness still exists as shown in Figure 6.14.

Several factors are discussed to explain the discrepancy between the hardness values from two unique test methods. The small indentation size may enhance the hardness of films because of the increase of dislocation density in the low load-displacement. The residual compressive stress might influence the hardness from nanoindentation by reducing the shear stress that is applied from the indentation. Grain size difference in testing specimens can contribute to hardness change. Unfortunately, none of the factors can be shown to be responsible. If we modify the Tabor empirical relationship, we can get a good agreement in hardness values from two different techniques, as shown in Figure 6.15. The modified relationship between hardness and flow stress is given by

$$H = 4\sigma \qquad (6.14)$$

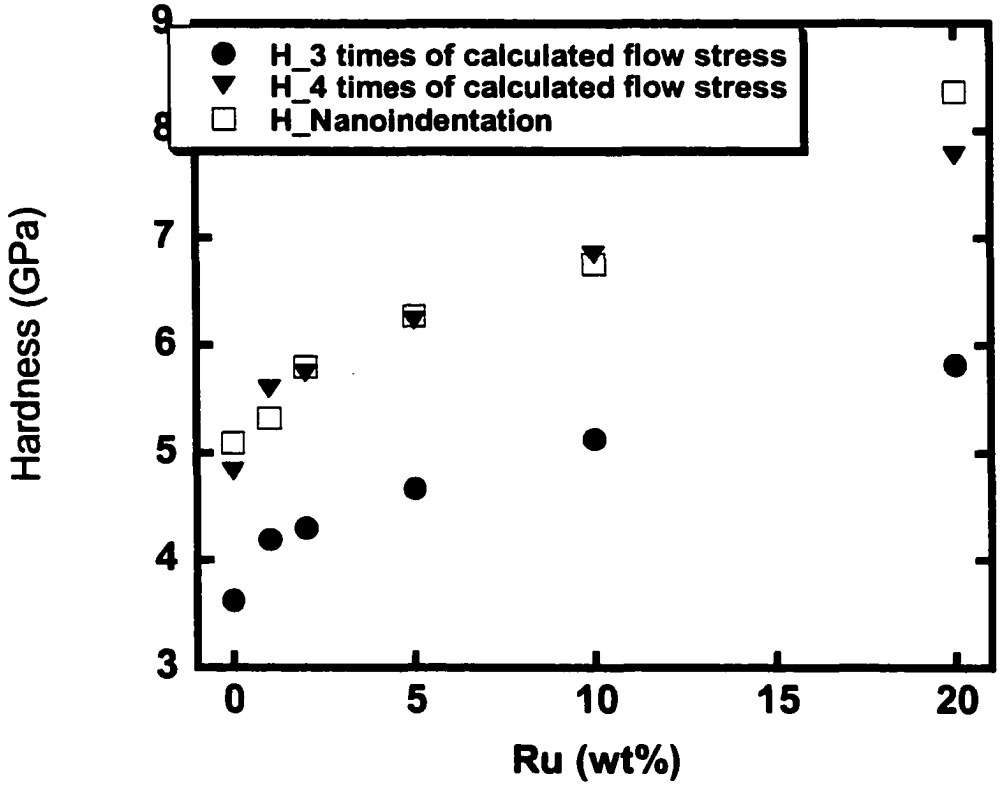

Figure 6.15. Hardness of Pt and Pt-Ru films. Measured hardness values from nanoindentation are agree with the calculated hardness values. The calculated hardness (triangle) is obtained from 4 times of the flow stress model, Equation 6.12. Average grain sizes of as-deposited films are used for this calculation. The traditional Tabor relation is also represented as circle dots in the graph, but the original empirical relationship does not describe the hardness behavior of Pt and Pt-Ru films.

The original Tabor equation is that hardness and flow stress are related by a factor of 3. This is an empirical equation by comparing the hardness and flow stress values in bulk specimens. In our study, the mechanical test of Pt and Pt-Ru thins film shows somewhat different relationship of hardness and flow stress. The modified Tabor given in Equation 6.14 can predict the relationship well.

6.6 Summary and Conclusions

The hardness of the solid solution alloy films is increased by an increase in Ru content. Three strengthening mechanisms are investigated to understand flow stress behavior of Pt and Pt Ru thin films at room temperature. A schematic diagram of the dislocation motion in the film is shown in Figure 6.16. The dislocation motion in thin films is constrained by three factors: dimension of film (thickness), grain boundary and solute atom. The dimensional constraint (thickness effects) cannot predict the flow stress of films well. The grain size hardening predicts more reasonable flow stress values compared to the dimensional constraint mechanism. However, the grain size strengthening combined with dimensional constraints cannot fully describe the flow stress change with Ru increase. After the solid solution strengthening term is added to the strengthening mechanisms of Pt-Ru alloy films, the flow stress behavior can be well predicted by the three hardening mechanisms. The solid solution strengthening mechanism significantly increases the film strength.

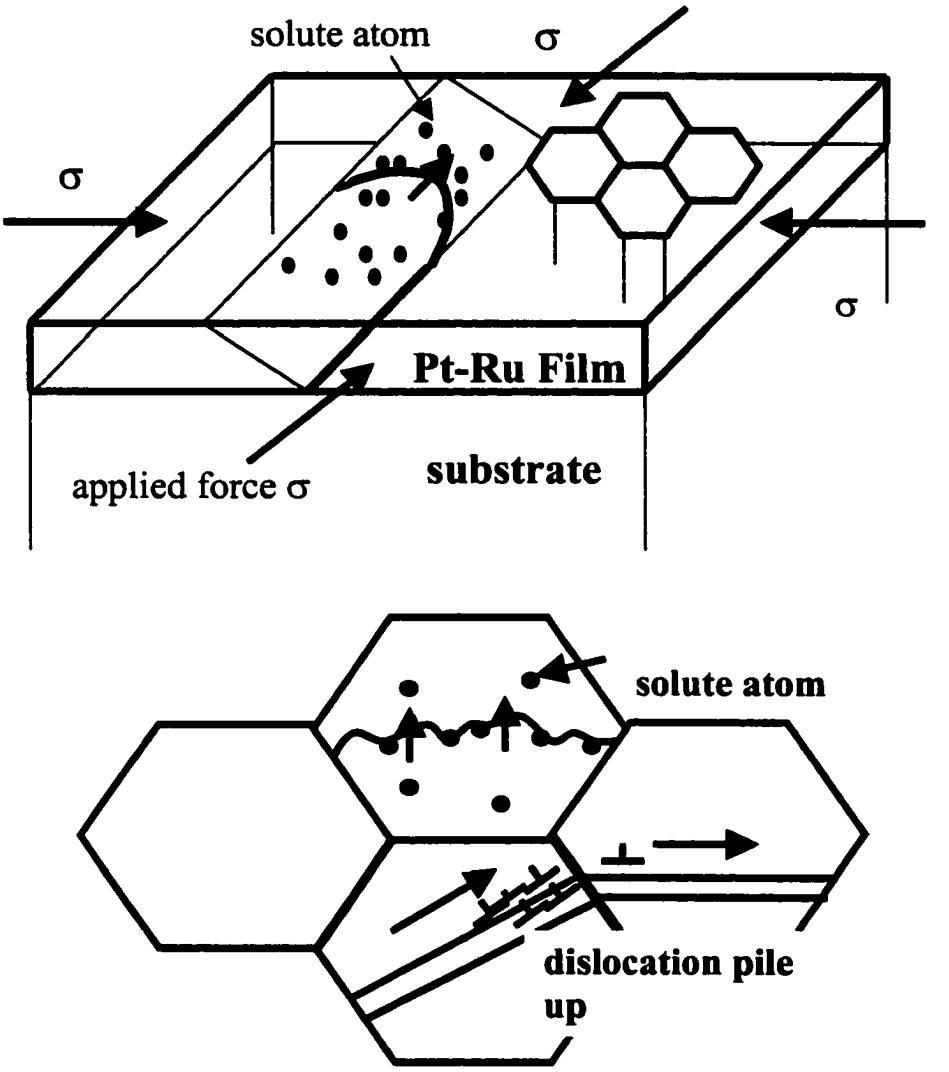

Figure 6.16. Schematic diagrams of dislocation motions in Pt-Ru thin film. 3 strengthening mechanisms of dimension, microstructure and solid solution hardenings are illustrated. The movements of dislocation are constrained by 3 different factors.

A flow stress model based on dislocation motion in thin films, which includes three strengthening terms due to substrate constraint, grain size strengthening and solid solution strengthening, very well predicts the flow stress change over a wide range of solute content. A comparison of the relative contributions of the three mechanisms reveals that the solid solution strengthening mechanism is the main mechanism associated with the film hardening.

Hardness values obtained from the nanoindentation technique and wafer curvature method shows a discrepancy. Several factors including indentation size effect and the grain size change after thermal cycling could be responsible for the different hardness values from nanoindentation and wafer curvature methods. From our nanoindentation and wafer curvature results, a modified Tabor equation, $H=4\sigma$, can predict the relationship between hardness and flow stress.

Ch. 7 Relaxation mechanisms of Pt thin films at high temperature

7.1 Introduction

Pt is used as an electrode material for DRAM device application due to its excellent properties [Chapter 1 of this dissertation]. For this application, high processing temperature is applied for the device fabrication. A large temperature range of thermal cycling during processing induces stress in the film due to the difference in coefficient of thermal expansion between the Pt film and substrate. Grain growth and diffusional mechanisms, which are dominant at high temperature, result in changing the stress state of the Pt bottom electrode. Therefore, it is important to understand the mechanical behavior of Pt films during thermal cycling for this application. However, there has been little study of the fundamental mechanical properties of Pt thin films. Only studies of Pt thin film behavior influenced by interaction with a Ti adhesion layer have been introduced, but do not provide systematic understanding of mechanical behavior of the film at high temperature [Hren 1992, Spierings 1995]. In our study, Pt thin films with different grain sizes were compared and the thermocycling behaviors of the films were investigated according to possible high temperature relaxation mechanisms. A modification to one model, the diffusional wedge model, provides a good match to the experimental data.

7.2 Experimental Techniques

Two types of Pt films were compared in this study. One Pt film (type 1) was prepared at Lehigh University while other Pt films (type 3) and data were used from experiment results obtained by Fahey [Fahey 1998]. The first set of Pt films were prepared by DC-magnetron sputtering at ambient temperature onto uncooled substrates at a base pressure of 4.5×10^{-9} torr (Type 1). After film fabrication, the thickness of the films was found to fall in the range of 200nm as measured by Alpha Step Profilometer (Tencor). Certain samples were annealed at 800°C in N_2 atmosphere to observe microstructure changes. TEM image analysis was performed to measure average grain sizes of the as-deposited and annealed Pt films. The X-ray diffraction method was used to observe crystal texture. 250 nm thick (type 3a) and 200 nm thick (type 3b) Pt films was deposited by RF Magnetron Sputtering on Si (001) wafers with 100 nm of thermal SiO_2 (type 3) [Fahey 1998]. Each substrate wafer was first heated to 500°C in the deposition chamber under vacuum for 30 min. The substrate temperature was then lowered to 350°C for deposition. Ar pressure of 15×10^{-3} torr was used to produce these Pt films. The film microstructure was characterized both before and after post-growth annealing using x-ray diffraction and scanning probe microscopy (SPM).

The stress in the Pt films was measured by the wafer curvature method. Ramping rates of 6°C per minute were used for the temperature cycling (type 3a film) in air atmosphere [Fahey 1998]. Ramping rates were 10°C/min (type 3b film) [Fahey 1998] and 12°C/min (type 1 film) for the thermal cycles done on this system in N_2 atmosphere. The experimental conditions and sample names are listed in Table 7.1

Table 7.1 Pt films experimental conditions and names

	Film	Name	Wafer curvature measurement
Type 1 (deposited at room temperature)	Pt 200 nm thick	Type 1	800°C in N_2 atmosphere
Type 3 (deposited at 350°C) [Fahey 1998]	Pt 250 nm thick Pt 200 nm thick	Type 3a Type 3b	660°C in air atmosphere 1000°C in N2 atmosphere

7.3 Results and Discussion

7.3.1 Microstructure and Stress-temperature curves of Pt films

Pt films with different grain sizes were prepared by sputtering. As-deposited Pt films of type 3 [Fahey 1998] have a grain size on the order of 100nm whereas the average grain size of an as-deposited film of type 1 is 35 nm. All films showed strong (111) crystal orientation. Films of the three types listed in Table 7.1 were subjected to different thermal cycling conditions. Type 3a was thermocycled up to 660°C, while Type 3b and type 1 were heated up to 1000°C and 800°C, respectively. Wafer curvature results are shown in Figures 7.1 and 7.2 for temperature cycling up to 660°C, 1000°C and 800°C. Type 3b and type 1 films were thermal cycled more than two times. After the first thermal cycling, the stress-temperature curves become stable loops as shown in Figures 7.1(b) and 7.2. The grain size of an as-deposited film is usually very small and this small-grained structure is unstable. The excess volume associated with the large number of grain boundaries in as-deposited films is largely removed during the first heating. The stress-temperature curves show that the microstructures of Pt films change rapidly during heating but quickly reach an equilibrium state.

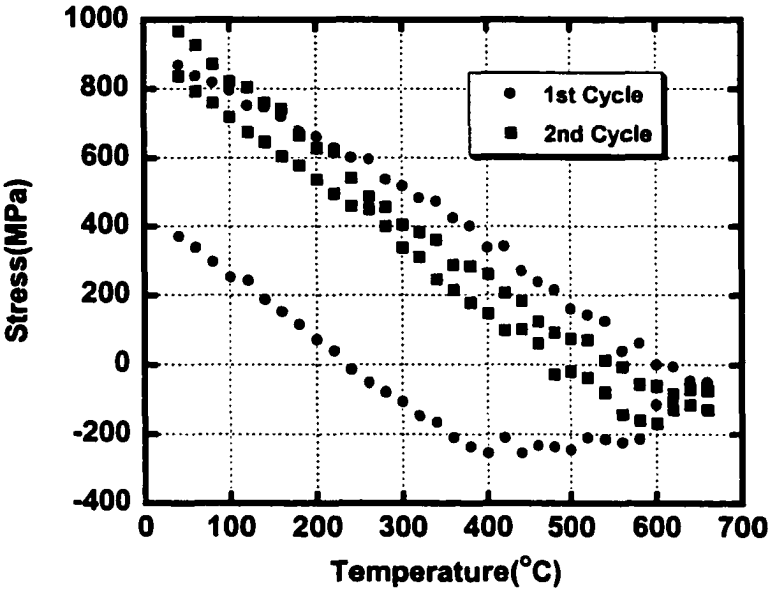

(a)

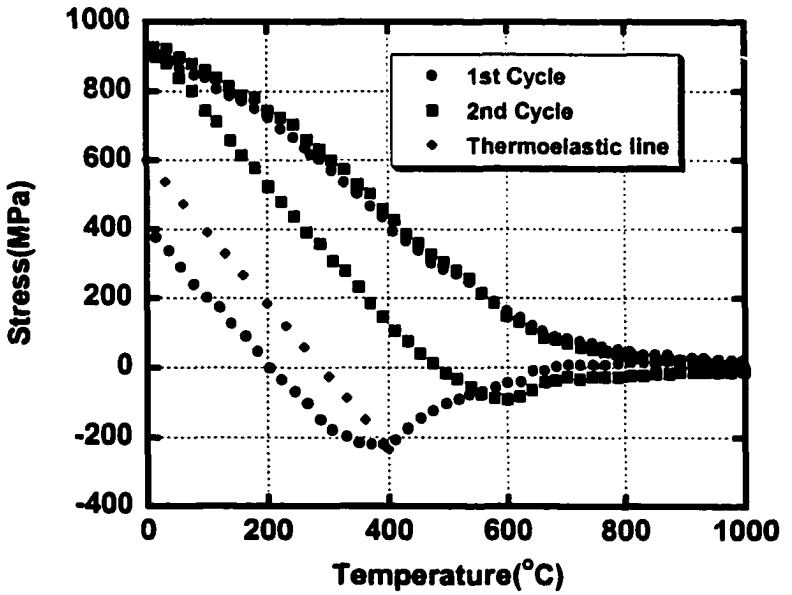

(b)

Figure 7.1. Stress-temperature curves for Pt thin films. (a) the Pt film (type 3a), which is 250nm thick, annealed up to 660°C. (b) 200 nm thick Pt film (type 3b) thermocycled up to 1000°C. The modulus used in (b) for a film is {111} textured. [Fahey 1998]

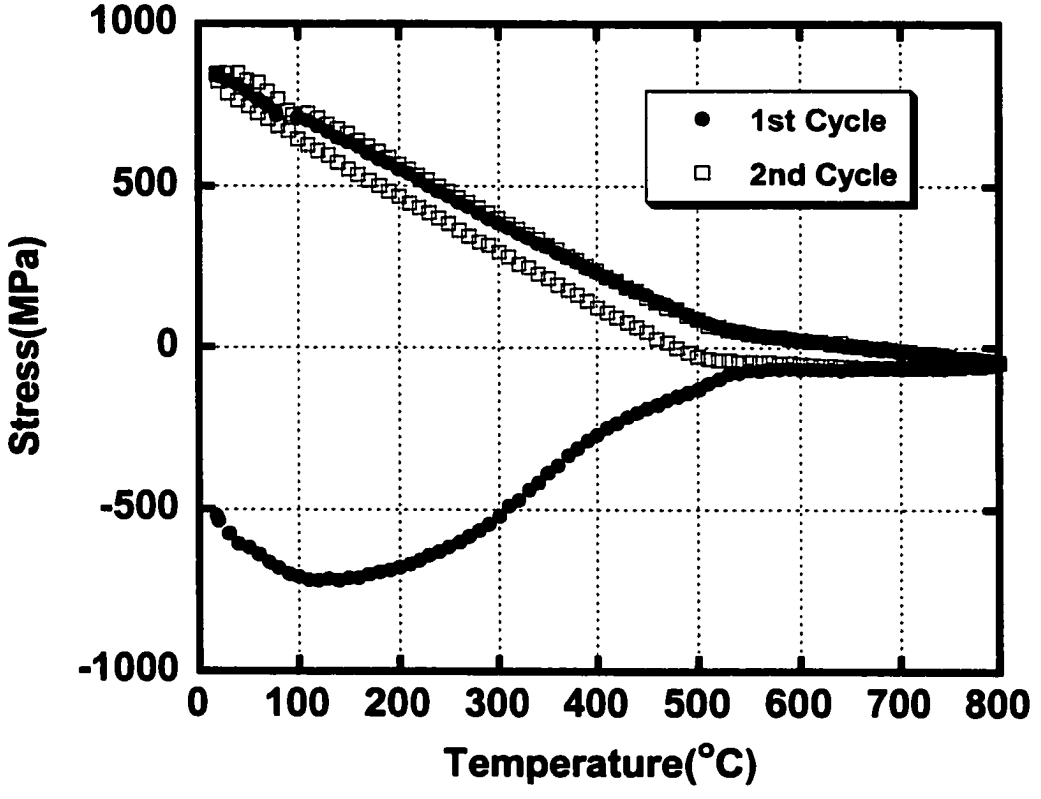

Figure 7.2 Stress-temperature curve of Pt film. Pt film (type 1) was thermocycled up to a temperature of 800°C. The film is 200nm thick and shows strong (111) orientation.

Any thermal cycling after the first cycle distinguishes the inherent mechanical behavior of Pt films, which is elastic and plastic deformation, from the microstructure effects, which is mostly grain growth effects.

Several different types of strain can develop in the film: the applied strain due to thermal expansion mismatch of the film and substrate and growth strains that are associated with the change in density. The stress in the film is determined by the total of all the elastic and plastic deformation mechanisms acting during thermal cycling. During heating in the low temperature regime, the film deforms elastically in response to the thermal expansion mismatch of the Pt film and the Si substrate because plastic deformation mechanisms are not active. In the first cycle, the stress behavior of type 3b and type 1 follows a thermoelastic line up to 400°C shown in Figures 7.1(b) and 7.2. The difference in thermal expansion coefficients for the film and substrate is 6×10^{-6} °C^{-1}. The thermoelastic line is described by the stress-temperature relationship, Equation 2.6. Strong (111) orientation was observed in all of the Pt films. So the biaxial modulus for (111) orientation is used for the thermoelastic line calculation. The slope of the line matches with that of the stress-temperature curve at the low temperature region below 400°C. Upon further heating, the shape of the stress-temperature curve is determined by a combination of grain growth stresses and the thermal stress. The intrinsic stress of type 3b was –200MPa after deposition, as is indicated by the thermoelastic behavior at 350°C, the deposition temperature. Although the film of type 3b was prepared at 350°C, the deposition temperature is only $0.28T_m$. Thus, significant intrinsic stress is observed to contribute to the total stress during the first cycle. In Figure 7.2, large compressive residual stress at room temperature is shown in the as-deposited type 1 film. This is due

to the sputtering deposition conditions. Low Ar working pressure contributes to compressive internal stress in metal films during film deposition [Thornton 1979].

The second stress-temperature curves also show elastic behavior at the initial temperature region as shown in Figures 7.1 and 7.2. At some point (about 500°C), the stress-temperature curves do not follow the elastic line. This behavior indicates the onset of plastic deformation. Upon further heating, the stress level of Pt films is determined by the dominant plastic deformation mechanisms. This behavior is similar to that in the stress-temperature curve of Cu films [Flinn et al 1987]. In both curves of Figures 7.1(b) and 7.2, the Pt stress falls steadily to zero as the temperature increases above 600°C and 500°C, respectively. During cooling, the slopes of the stress-temperature curves increase as the plastic deformation mechanisms slow down. This is in contrast to the temporary increase in compressive stress observed from approximately 400-600°C in previous studies [Hren et al. 1992, Spierings et al. 1995]. It was proposed that this increase was due to the interaction between the Pt and the underlying Ti adhesion layer used in both cases. In our samples, the lack of a compressive stress increase coupled with the absence of a Ti layer supports this hypothesis and confirms that the high residual stresses at room temperature are due to the inherent behavior of the Pt thin film.

The high temperature mechanical behaviors of metallic films have been explained by two relaxation models, the deformation mechanism maps model and the diffusional wedge model [Thouless et al. 1993, Gao et al. 1999]. In the next section, these two approaches are investigated to understand stress-temperature behavior of Pt films.

7.3.2 Deformation mechanism maps model (deformation maps model)

Thouless and Vinci [Thouless et al. 1993, Vinci et al. 1995] discussed the high temperature relaxation mechanisms of metallic films. The model of plasticity is based on the deformation mechanism map approach introduced by Frost and Ashby [Frost et al. 1982]. The deformation mechanism maps of bulk crystalline materials were constructed in terms of temperature to understand a dominant deformation mechanism in a region of stress-temperature map. Since several deformation mechanisms are active and they are often competing with each other, deformation maps of crystalline materials show information about the range of dominance of the mechanisms of plasticity. Thouless [Thouless et al. 1993] proposed five individual mechanisms to explain the stress-temperature behavior of Cu thin films. Modified creep equations for the bulk material were applied to thin films since the stress state and microstructure are different in thin films compared to bulk materials.

Deformation mechanisms in this model are grain boundary and lattice diffusion creep, dislocation glide (yield), low temperature dislocation creep and high temperature dislocation creep. The diffusion creep mechanism is the flow of vacancies and interstitials through a crystal under the influence of applied stress. This mechanism can be specified by two mass transport methods. If diffusion occurs along grain boundaries, the grain boundary creep (Coble) mechanism is active. If creep is the result of diffusion through the lattice, lattice creep (Nabarro-Herring creep) is dominant. The equations for diffusion creep were modified by Thouless to account for the fact that atoms must diffuse from the grain boundaries in the film to the nearby film surface rather than between

neighboring grain boundaries in order to reduce the stress of the film. The plastic strain rate ($\dot{\varepsilon}_1$) due to grain boundary creep mechanism is given by

$$\dot{\varepsilon}_1 = \frac{3\delta D_{0b}\Omega}{kTdh^2}\sigma \exp\left(\frac{-Q_b}{kT}\right) \quad (7.1)$$

where is the atomic volume, k is Boltzmann's constant, d is the average grain size of the film, and h is the thickness of the film, σ is the stress in the film, T is the absolute temperature, Q_b is the activation energy for grain boundary diffusion, and δD_{0b} is the pre-exponential coefficient for grain boundary diffusion. The plastic strain rate resulting from the diffusion lattice creep mechanism is defined by

$$\dot{\varepsilon}_2 = \frac{3D_{0v}\Omega}{kTdh}\sigma \exp\left(\frac{-Q_v}{kT}\right) \quad (7.2)$$

where Q_V and D_{0v} are the activation energy and pre-exponential coefficient for lattice diffusion.

The dislocation glide mechanism involves dislocation motion along slip planes and is thermally activated. The plastic strain rate due to dislocation glide is given by

$$\dot{\varepsilon}_3 = \frac{\dot{\gamma}_0}{\sqrt{3}}\exp\left[\left(1-\frac{\sigma}{\sqrt{3}\hat{\tau}}\right)\left(\frac{-Q_g}{kT}\right)\right] \quad (7.3)$$

where $\dot{\gamma}_0$ is a pre-exponential constant, Q_g is the activation energy for dislocation glide, and $\hat{\tau}$ is the shear strength at 0 K.

Dislocation creep includes the movement of dislocations by the diffusional transport of vacancies under the influence of applied stress. At high temperature, dislocation climb is controlled by diffusion from the dislocation through the lattice whereas the dislocation movement is controlled by diffusion along the dislocation core at

Table 7.2. The parameters used in calculation for stress-temperature behavior of Pt films.

Parameter	Symbol	Value	Units	Reference
Atomic volume	Ω	1.51×10^{-29}	m^3/atom	[Brown 1980]
Burger's vector	b	0.277	nm	
Grain size	d	200, 100	nm	
Film thickness	h	200, 250	nm	
Shear modulus	μ	76	GPa	
Biaxial modulus	M	320	GPa	
Shear strength	τ	462, 900	Mpa	
Glide prefactor	γ_0	10^6	s^{-1}	[Frost et al. 1982]
Power law exponent	n	5		
Dorn constant	A	200, 1000		
Power law breakdown	α'	700, 1000	kJ/atom	
Activation energy	Qg	2.33×10^{-21}	kJ/atom	
Lattice diffusion activation energy	Qv	4.62×10^{-22}	kJ/atom	[Brown 1980]
Grain boundary diffusion activation energy	Qb	2.77×10^{-22}	kJ/atom	
Dislocation core diffusion activation energy	Qc	2.77×10^{-22}	kJ/atom	
Lattice duffusion prefactor	D_{ov}	2.2×10^{-5}	m^2/s	[Brown 1980]

Grain boundary diffusion prefactor	δD_{ob}	6.1×10^{-15}	m^3/s
Dislocation core diffusion prefactor	acD_{oc}	6.8×10^{-24}	m^4/s

The simulated stress-temperature curve of Pt film can be constructed with the Equations 7.1, 7.2, 7.3, 7.4, 7.5 and 7.6 using the values for the parameters listed in table 7.1.

Simulated stress-temperature curves

The calculated stress-temperature curves for a 200 nm thick Pt film according to different average grain size are shown in Figure 7.3. A heating and cooling rate of 10°C/min is used for the stress-temperature plots. Although different grain sizes were taken into account for the simulation, the simulation curves exhibit similar stress behavior. The effect of grain boundary diffusion is very active and leads to the stress free state in the film above about 350°C. Figure 7.4 shows thickness effects on stress evolution of the film. If we take into account length of diffusion paths such as film thickness and grain size together, the film can maintain an increasing stress level at high temperature as the film thickness increases, but complete stress relaxation is always observed above 600°C for films up to 3μm thick (much thicker than the films measured in this study).

Comparison of the model and experimental data

As is shown in Fig. 7.5, only if we completely remove the diffusion creep mechanisms can we closely reproduce the first heating curve Pt films. This approach only takes into account the dislocation creep mechanisms at high temperature. Obviously, the simulations in Figures 7.3 and 7.4 do not agree with the measured stress-temperature behavior of Pt films as shown in Figures 7.1 and 7.2. One possible interpretation of these comparisons is that these mechanisms, $\dot{\varepsilon}_1$ and $\dot{\varepsilon}_2$, must be greatly inhibited in these films and that dislocation processes must still play a significant role in the relaxation at higher temperatures [Flinn et al. 1987, Keller 1995]. The grain growth and work hardening may be responsible for the difference between the model and the measured curve. However, if we modify the parameters in the calculations, we can closely produce the second stress-temperature behavior of Pt films as shown in Figure 7.6. When only the dislocation creep mechanisms are active at high temperature, the modification of $\hat{\tau}$, A and α' allow us to construct the high temperature stress-temperature behavior of Pt film. A value $6 \times 10^{-3}\mu$ of $\hat{\tau}$ is for bulk Platinum. The higher shear stress is expected in thin film compared to bulk material. Instead of $6 \times 10^{-3}\mu$, $12 \times 10^{-3}\mu$ is used for the calculation. A and α' are empirical constants. Thus two values are adjusted for the construction. Grain growth effects on the stress evolution can be eliminated at the second thermal cycling. Thus, the discrepancy between the predicted curve and measured curve could be attributed to work hardening effects.

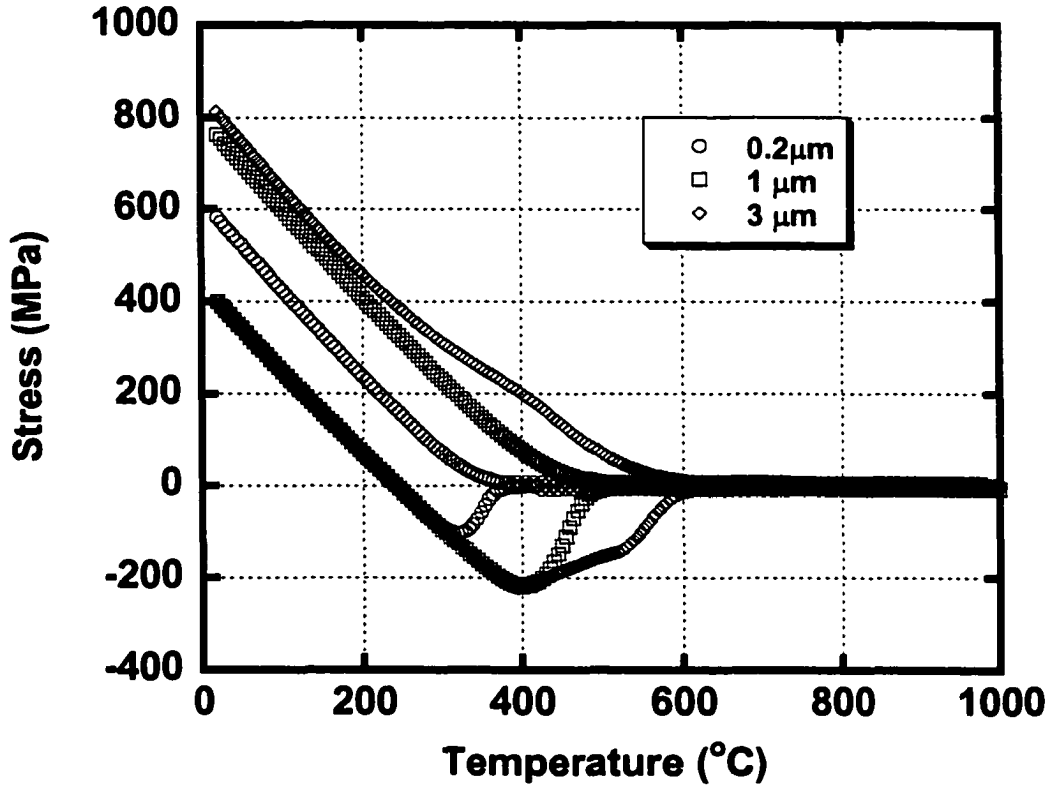

Figure 7.4. Simulated stress-temperature curve of Pt films. Thicknesses of films are 0.2 μm, 1 μm and 3 μm and grain sizes are same as the thicknesses of films. All stress of films are completely relaxed at high temperature.

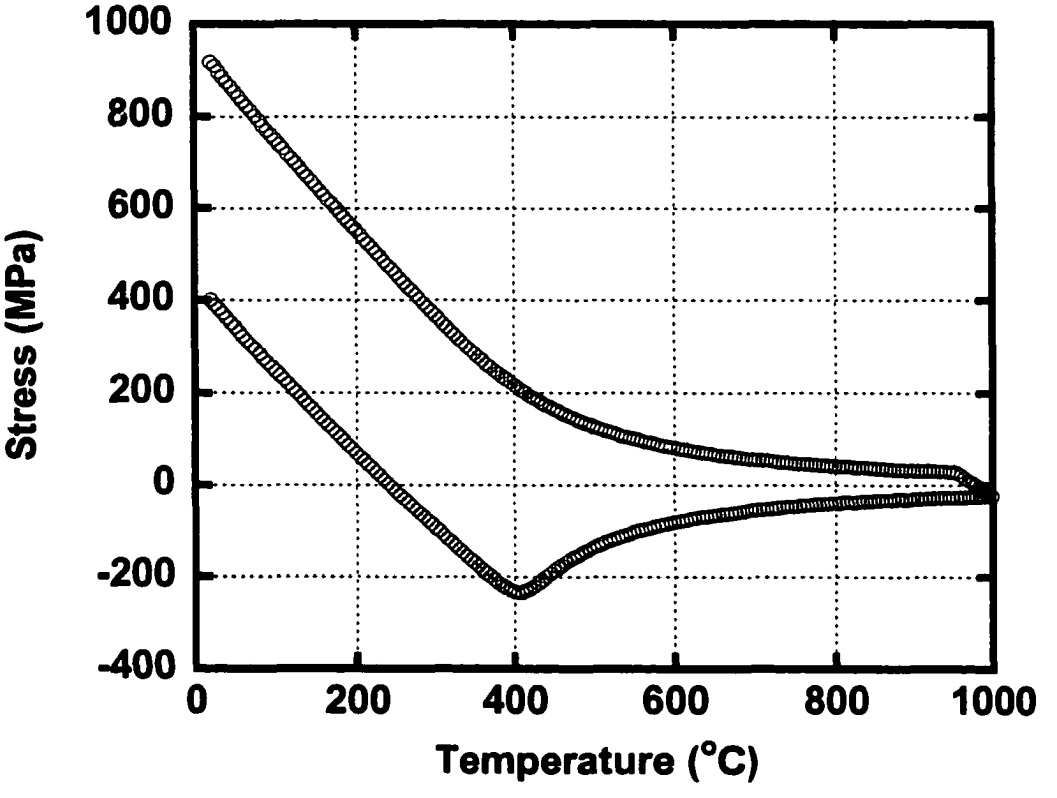

Figure 7.5. Simulated stress-temperature curves for Pt film. The diffusion creep mechanisms are eliminated in this calculation. Only dislocation creep mechanisms are dominant at high temperature.

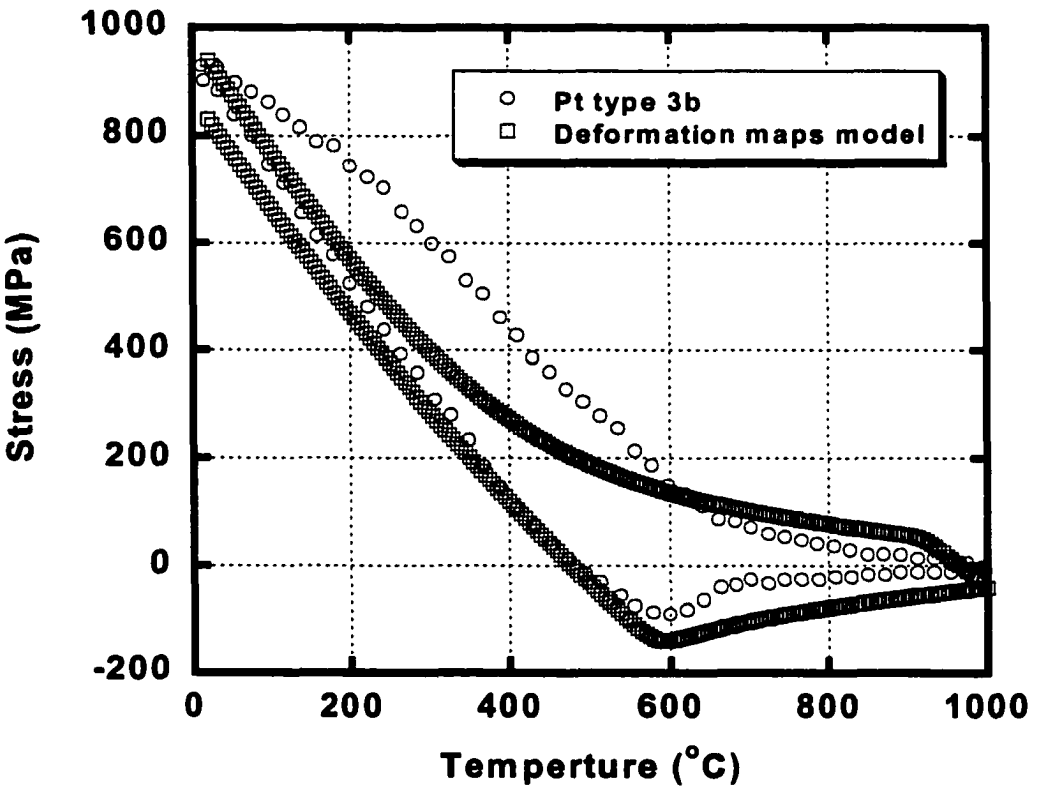

Figure 7.6. The simulated curve uses only the mechanisms of dislocation creep and glide to relieve the stress. For the simulation of this curve, modification of A, α' and $\hat{\tau}$ is used. Values of 200, 700 and 900 MPa are used for A, α' and $\hat{\tau}$, respectively. Curve shows good agreement with the second thermoclcying curve of Pt film. Difference between the predicted curve and measured stress may be attributed to work hardening effects during cooling process.

However, when we introduce the model to small-grained Pt film (type 1), the model cannot reproduce high temperature stress behavior as shown in Figure 7.7. The model predicts a stress level at high temperature whereas small-grained film shows low stress level above 500°C. Since Pt films have no surface oxide, there is no reason why the diffusion mechanisms should be inactive. The diffusion mechanisms should be even more active in the fine-grained film but the experimental data still shows less relaxation than is predicted by the model. There is no way that the dislocation creep model (alone) can fully account for the experimental observations.

The stress relaxation behavior of Pt films can also be inhibited due to the substrate effects on the relaxation mechanism. Strong adhesion between the film and the substrate eliminates the stress relaxation path at the interface. The stress at the center and bottom of the grain cannot be completely relaxed by the mechanism. Thus, the relaxation mechanism that includes substrate constraint effects should be introduced to examine high temperature behavior of the film.

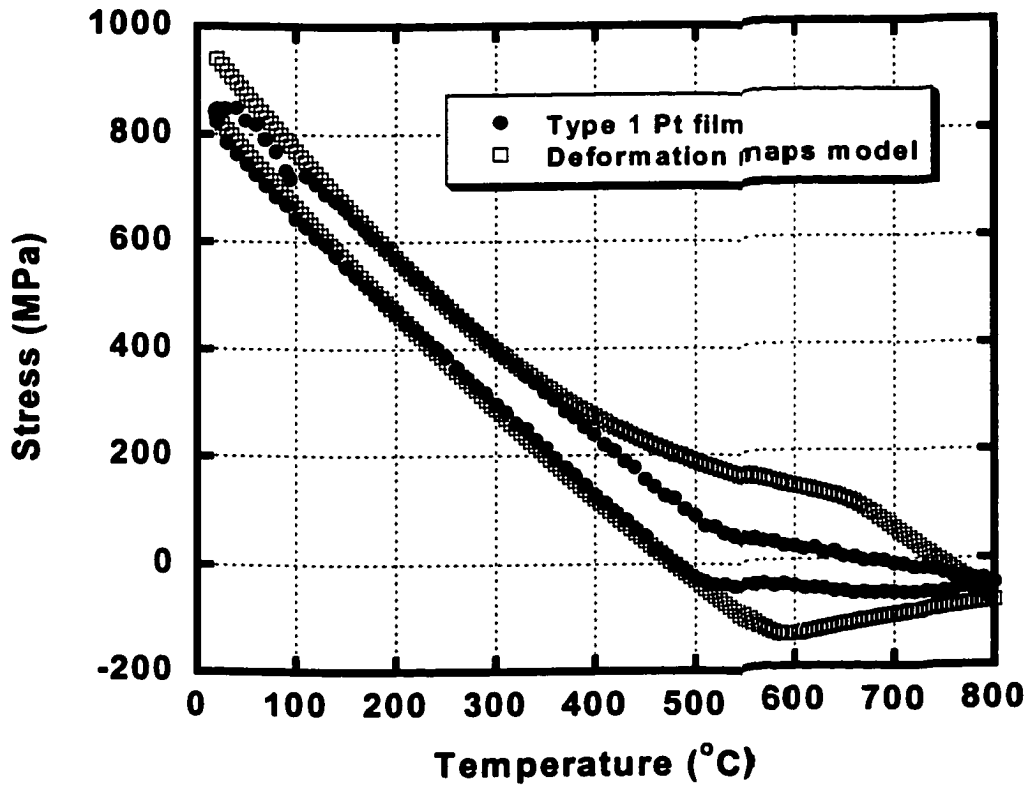

Figure 7.7. Comparison of the deformation maps model and measured stress-temperature curve of Pt film (type 1). Diffusion creep mechanisms are eliminated in this calculation. The deformation maps model predicts high stress level at high temperature.

7.3.3 Diffusional wedge model

Difusional relaxation of unpassivated films has been studied by Turlo and Gao [Turlo 1992, Gao et al.]. This mechanism follows the suggestion by the Jacson and Li [Jackson et al. 1982], that stress relaxation of unpassivated films would occur near the surface but not near the film/substrate interface because a well bonded interface inhibits diffusional relaxation. This approach proposed that grain boundaries in thin films are the paths to relax the stress of films during thermal cycling, resulting in a decrease in the stress at the grain boundary, σ_{gb} as shown in Figure 7.8. The kinetics of relaxation of the average grain boundary stress can be expressed in a recent model by Gao as [Gao et al. 1999]

$$\left(\frac{d\sigma_{gb}}{dt}\right) = -\frac{\sigma_{gb}}{\tau_{gb}} \quad (7.7)$$

where t is the time for the diffusional relaxation during thermocycling and τ_{gb} is the time constant for the grain boundary diffusion process [Dlabec 2000] expressed as

$$\tau_{gb} = \frac{0.3(1-\nu^2)\pi h^3 k_B T}{E\delta D_{gb}\Omega} \quad (7.8)$$

where Ω is the atomic volume and δD_{gb} is the grain boundary diffusivity given by

$$\delta D_{gb} = \delta D_{ob} \exp\left(-\frac{Q_b}{RT}\right) \quad (7.9)$$

By treating the diffusionally relaxed grain boundaries as cracks in the film, the relation of the relaxation effect on the curvature of the substrate and the average stress in thin films can be expressed as [Turlo 1992]

$$\Delta K_{crack} = -6\frac{1-\nu_s}{E_s}\frac{h}{t_s^2}\Delta\sigma\left[1-\exp\left(-\frac{7.53\pi}{6}\frac{h}{d}\right)\right] \quad (7.10)$$

where $\Delta\sigma$ is the film stress change due to diffusional relaxation (σ_o initial stress- σ_{gb} grain boundary stress), h is the film thickness, t_s is substrate thickness, d is the grain size of the film and E_s and ν_s are the modulus and Poisson's ratio of the substrate, respectively. Thus, the rate of partial grain boundary relaxation (grain boundary stress) is expressed as

$$\left(\frac{dK}{dt}\right)_{gb} = 6\left(\frac{1-\nu_s}{E_s}\right)\frac{h}{t_s^2}\left[1-\exp\left(-\frac{7.53\pi}{6}\frac{h}{d}\right)\right]\frac{d\sigma_{gb}}{dt} \quad (7.11)$$

The basic assumptions of this model are that only diffusion and elastic deformation mechanisms are responsible for stress evolution during thermal cycling. The stress evolution in terms of elastic deformation and grain boundary diffusional relaxation can be expressed as [Nix 1998]

$$\frac{d\sigma}{dt} = \frac{E_s}{1-\nu_s}\frac{t_s^2}{6h}\left(\frac{dK}{dt}\right) = \frac{E_s}{1-\nu_s}\frac{t_s^2}{6h}\left[\left(\frac{dK}{dt}\right)_{elastic} + \left(\frac{dK}{dt}\right)_{gb}\right] \quad (7.12)$$

where $\left(\frac{dK}{dt}\right)_{elastic}$ is the rate of curvature change due to elastic deformation according to thermal cycling. This term is defined by

$$\left(\frac{dK}{dt}\right)_{elastic} = -6\frac{1-\nu_s}{E_s}\frac{h}{t_s^2}\left(\frac{E_f}{1-\nu_f}\right)(\alpha_f-\alpha_s)\frac{dT}{dt} \quad (7.13)$$

where α_f and α_s are the coefficients of thermal expansion of the film and substrate. E_f is modulus of the film. By combining Equations 7.11 and 7.13, stress change in film during thermal cycling can be rearranged by

$$\frac{d\sigma}{dt} = -\left(\frac{E_f}{1-\nu_f}\right)(\alpha_f - \alpha_s)\frac{dT}{dt} + \left[1 - \exp\left(-\frac{7.53\pi}{6}\frac{h}{d}\right)\right]\frac{d\sigma_{gb}}{dt} \qquad (7.14)$$

where $\frac{d\sigma_{gb}}{dt}$ is defined by $-\frac{\sigma_{gb}}{\tau_{gb}}$ (Equation 7.7). Grain boundary relaxation according to thermal cycling also follows the same approach described above. The grain boundary stress change is a combination of thermal induced elastic deformation and grain boundary relaxation and given by

$$\left(\frac{d\sigma_{gb}}{dt}\right) = -\left(\frac{E_f}{1-\nu_f}\right)(\alpha_f - \alpha_s)\frac{dT}{dt} - \frac{\sigma_{gb}}{\tau_{gb}} \qquad (7.15)$$

Equations 7.15 and 7.16 can be used to predict the stress-temperature curve of Pt films. All values of the parameters that used in this calculation are listed in Table 7.1.

Simulated stress-temperature curve

The relaxation behavior of thin films is very dependent on temperature, film thickness and average grain size. Figures 7.9 and 7.10 show the predicted effects of temperature, film thickness and grain size on the stress development during thermal cycling. A heating and cooling rate of 12 °C/min is used for the stress-temperature plots. A stress drop on heating is observed while a rapid increase in stress on cooling is shown. The stress behavior on cooling at the highest temperature does not follow the elastic stress behavior.

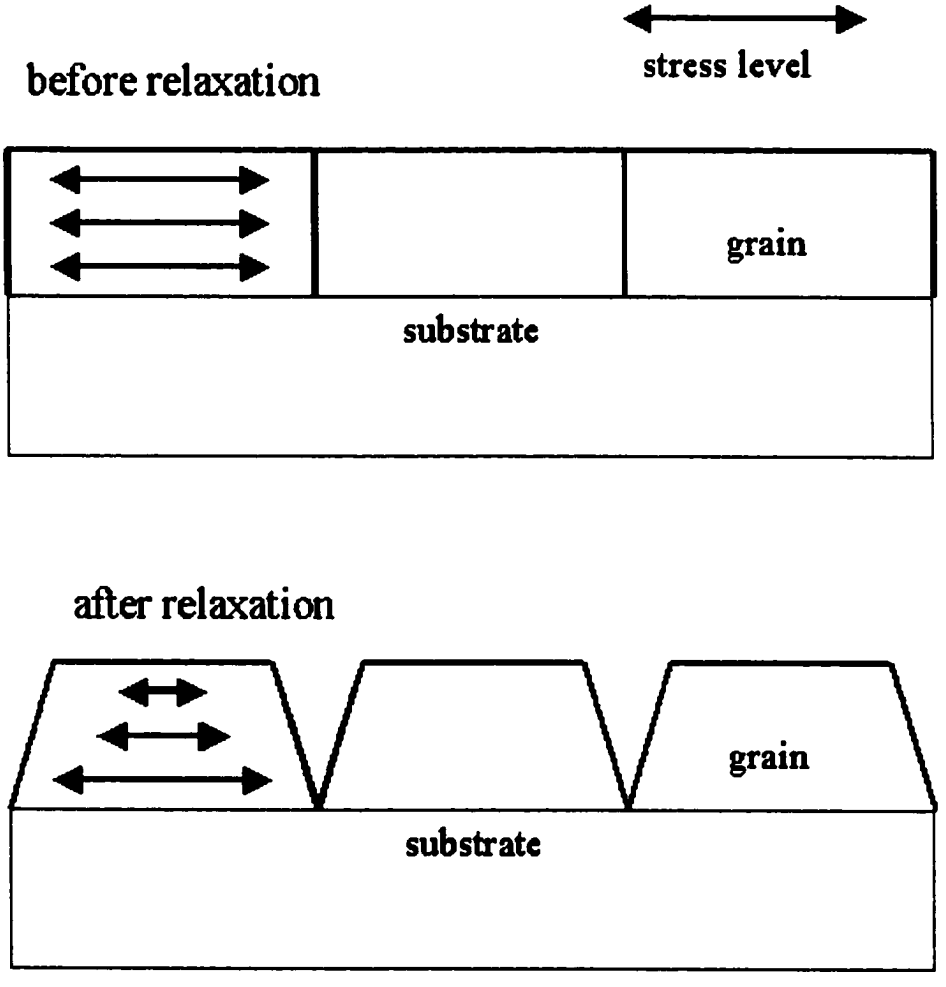

Figure 7.8. A schematic of stress level within a grain. Diffusion wedges forms at grain boundary, and the stress field is inhomogeneous in the film plane and in the direction normal to the film plane. Stress is relaxed at the film surface and at the grain boundary.

The relaxation rates of thicker films are slower at high temperature than those of thinner films because the diffusion paths are longer. The predictions from the model also indicate that thicker films have higher stress than thinner films after stress evolution.
This is an incorrect result because the dislocation motion at room temperature is constrained by film dimensions and this simulation does not include dislocation effects. Thinner films are usually expected to have higher residual stress than thicker films. The assumption of the model is that the films can relax the stress only through the diffusional process. High density of relaxation path in thinner films leads to low stress level whereas low density of the path in thicker films results in high stress level during thermal cycling. The grain size of films should also affect the relaxation rate as shown in Figure 7.10.

Comparison of model and experimental results

Figure 7.11 presents the diffusional relaxation model and experimental measurement of one Pt stress-temperature curve. The model calculation predicts thermal cycling behavior very similar to experimental observations. This agreement is especially good above 600°C. Figure 7.12 and Figure 7.13 show the diffusional wedge model and experimental Pt stress-temperature curves cycling up to 1000 °C (type 3b) and 800°C (type 2). The model can predict the heating portion of type 3 Pt film cycling, but does not show such good agreement with the stress-temperature behavior of the Type 1 sample that rapidly relaxes above 500°C. The cooling parts of both measured Pt film curves show different behaviors compared to the model predictions. The slope of cooling curve of type 3b film is moderately changed, but the sudden slope of stress-temperature curve change in type 1 Pt film is observed below 500°C. This behavior could be explained that

relaxation rates of the films are different. The relaxation mechanism in type 1 film stops below 500°C whereas the mechanism in type 3b film slows down at 700°C. So, relatively high residual stress is developed in type 3b film at low temperature regime due to the transition of relaxation mechanism. Diffusional relaxation mechanism according to different grain sizes may affect the stress evolutions of Pt films. High density of the diffusional path makes the stress relaxation more effective and produces fast relaxation behavior at high temperature in the case of type 1 film (smaller grain size compared to type 3b film). Although experimental curves of Pt films (type3b and type 1) show a large difference in relaxation temperature, the model does not predict as large a difference.

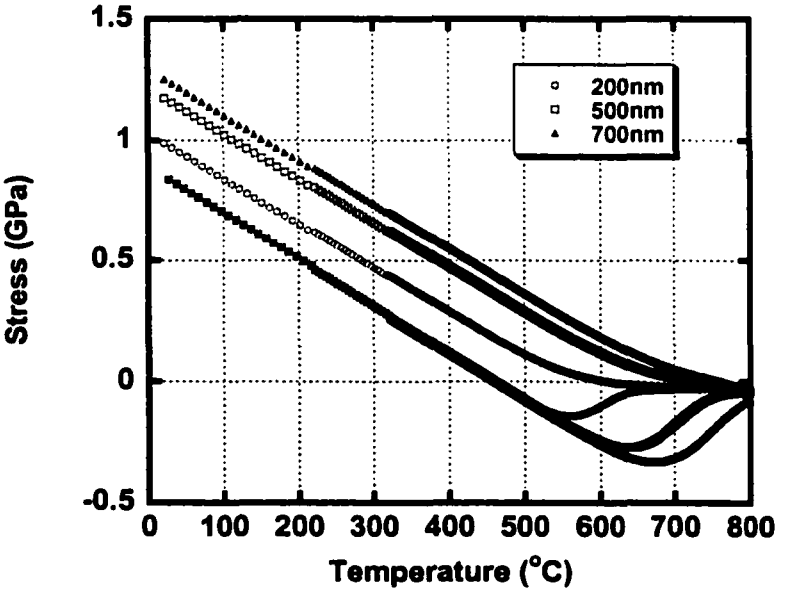

Figure 7.9. The stress-temperature plots from diffusional wedge model. The ratio of grain size and film thickness is one. The stress-Temperature curve of 200nm thick film is shown in circle dots and the curve of 500 nm thick film is shown in square dots. The triangle dots represent the stress-temperature curve of 700 nm thick film.

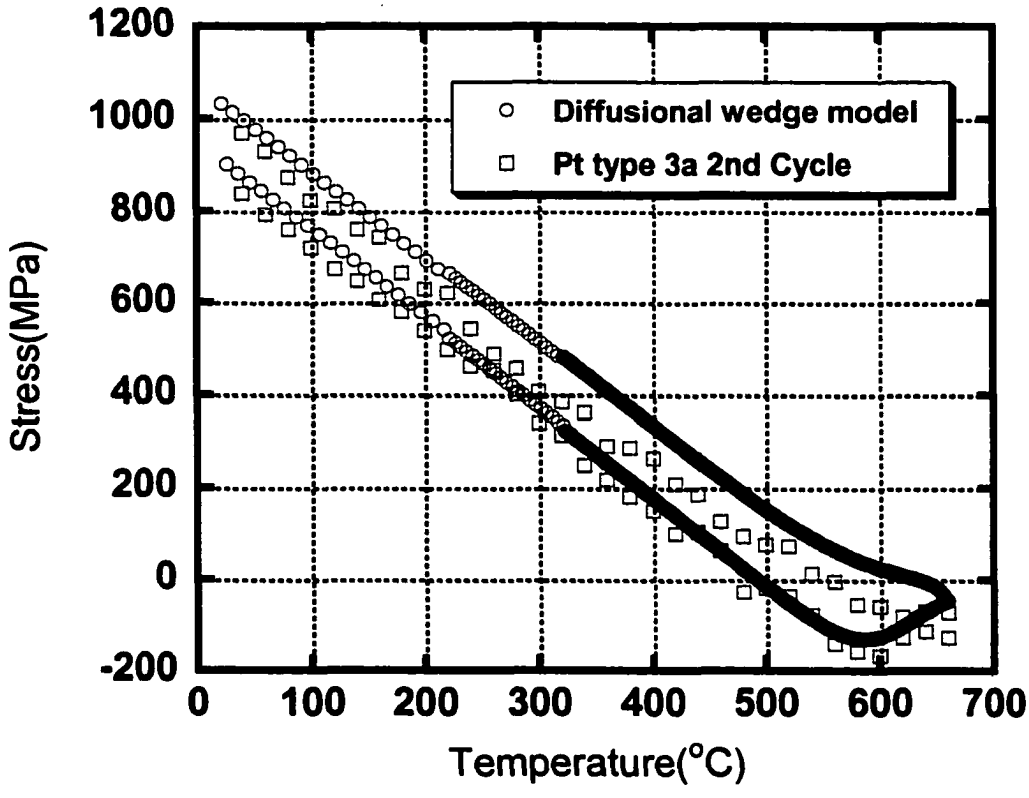

Figure 7.11. Diffusional wedge model curve and experimental curve. The thickness of the film is 250nm and average grain size is 200nm. Good agreement between the model and measured data is shown.

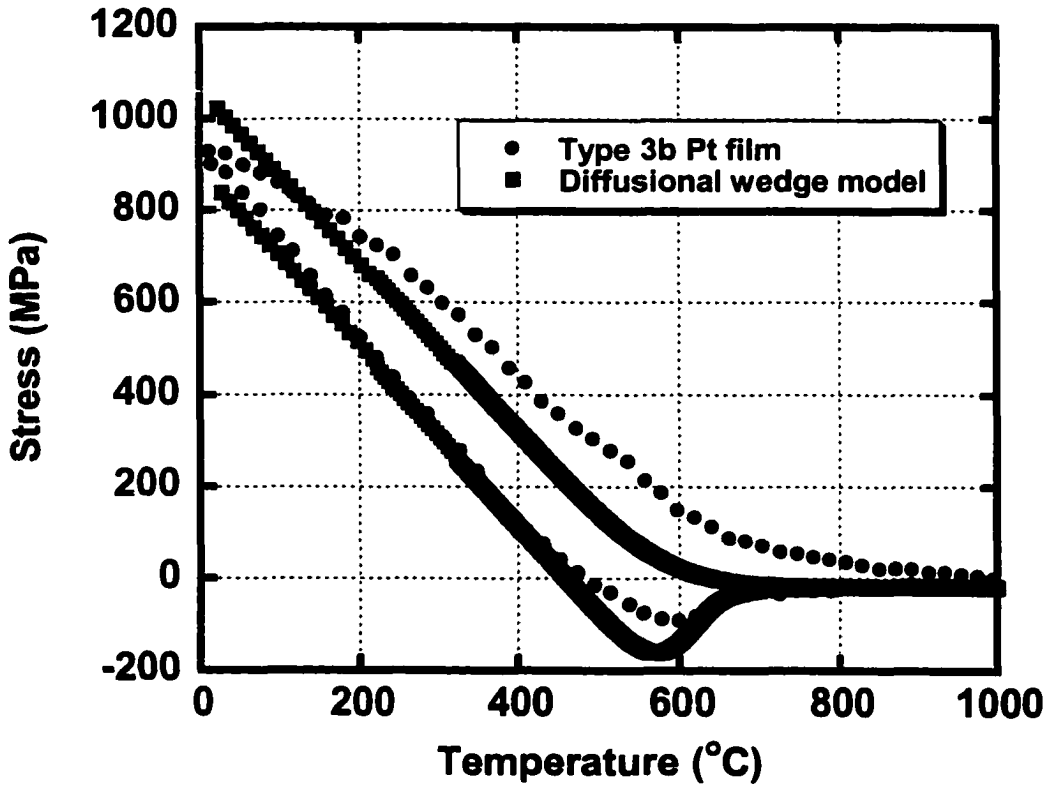

Figure 7.12. Comparison of stress-temperature curves of diffusion wedge model and Pt type 3b film. Although the model predicts completing relaxation above 600°C, the film maintains a certain level of the stress at high temperature.

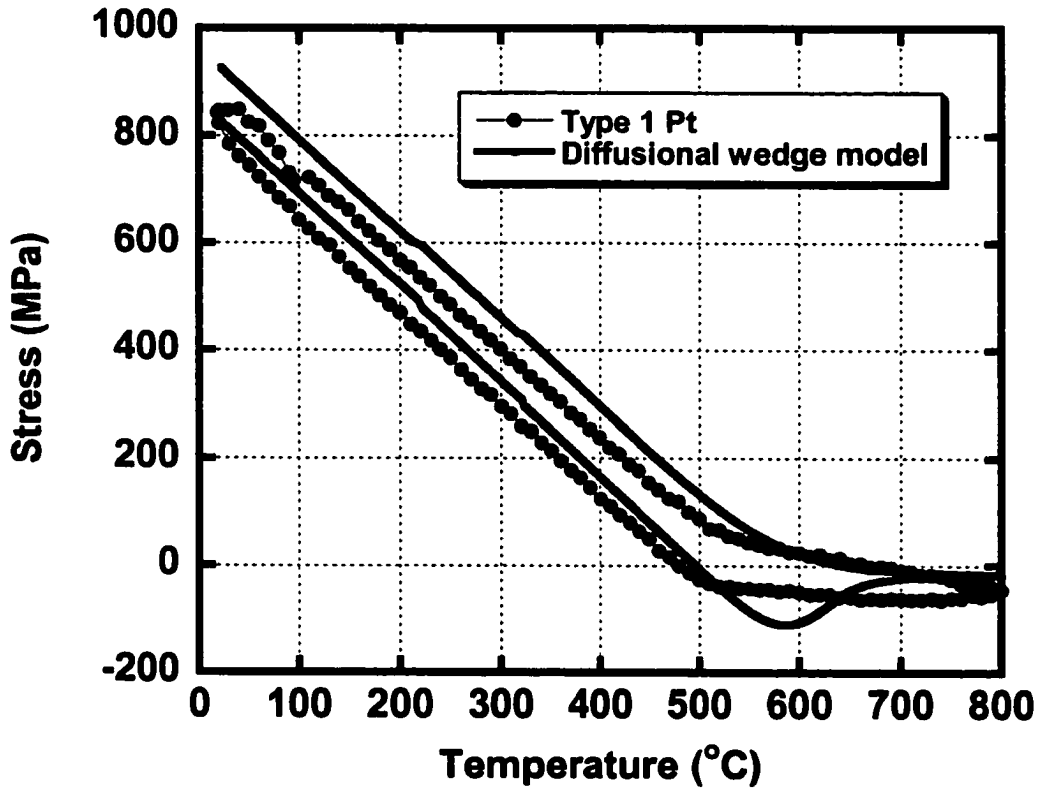

Figure 7.13. Diffusional wedge model and measured stress-temperature curve of type 1 Pt film. The model inaccurately predicts the stress-temperature behavior of Pt film.

7.3.4 Small grained film behavior (Deformation maps model and diffusion wedge model)

The high density of diffusion paths such as grain boundaries in Pt film (type 1) may cause the complete relaxation behavior of Pt film (type 1). To test this hypothesis, the parameters for the diffusional wedge model were modified to better match the high temperature mechanical behavior of the small-grained Pt film.

As shown in Figure 7.14, with modifications we can closely reproduce the thermal cycling behavior of the type 1 Pt film using the diffusion wedge model. In order to construct the stress-temperature curve, we need to change the thickness value of the film from 200 nm to 100 nm. This result implies that the film is acting like a columnar film of half its thickness. It is a reasonable approach because the average grain size of the type 1 film is about 100 nm. If we consider that this film is composed of a couple of grains thick as shown in Figure 7.15, the upper grains in the film may follow the prediction of the deformation mechanism map model since the model allows free sliding between the grains. According to that model, the stress state of a 100 nm thick Pt film drops to zero for all temperature above 350°C. We can therefore completely ignore the upper half of the film during stress evolution above 350°C which leads to the wedge diffusion relaxation mechanism for a 100 nm thick film with average 100 nm grain size. To support this result, the cross-section TEM image was acquired to observe grain morphology in the film. As shown in Figure 7.16, a semi-columnar structure is observed on the image with the film 1-2 grains thick. The microstructure of the films shows a good agreement with the grain structure assumption.

The combination of the deformation mechanism map mechanism and the diffusion wedge mechanism in the type 1 Pt film is illustrated in Figure 7.17. This figure describes two mechanisms acting simultaneously at high temperature. The upper portion of the film follows the deformation maps model whereas the lower half of the film is controlled by the diffusional wedge model. The stress in the upper half of the grains can completely be relaxed since diffusion creep mechanisms dominate at high temperature. The bottom grains cannot be completely relaxed due to the substrate constraints effects on the diffusion mechanism. This analysis leads to the conclusion that the diffusion wedge model alone is very effective only for thin and small-grained films that exactly match its assumptions, but that a minor modification can broaden its applicability.

Figure 7.18 shows the second stress-temperature curves of the Pt-Ru alloy films. These curves show high strength of the films with increasing Ru content at room temperature [discussed in Chapter 6]. However, no significant strengthening effects are observed at high temperature. The relaxation behavior of the alloying films is also observed. Alloying is only effective at low temperatures where dislocation motion seems to dominate. It is not effective at high temperature where diffusion dominates. This is in agreement with the high solubility (small segregation) expected for Ru in Pt. This behavior is not seen in bulk materials because the scale and constraints are different. Solid solution strengthening Pt alloys show bulk strengths at high temperature well above that of pure Pt [Usikov 1980].

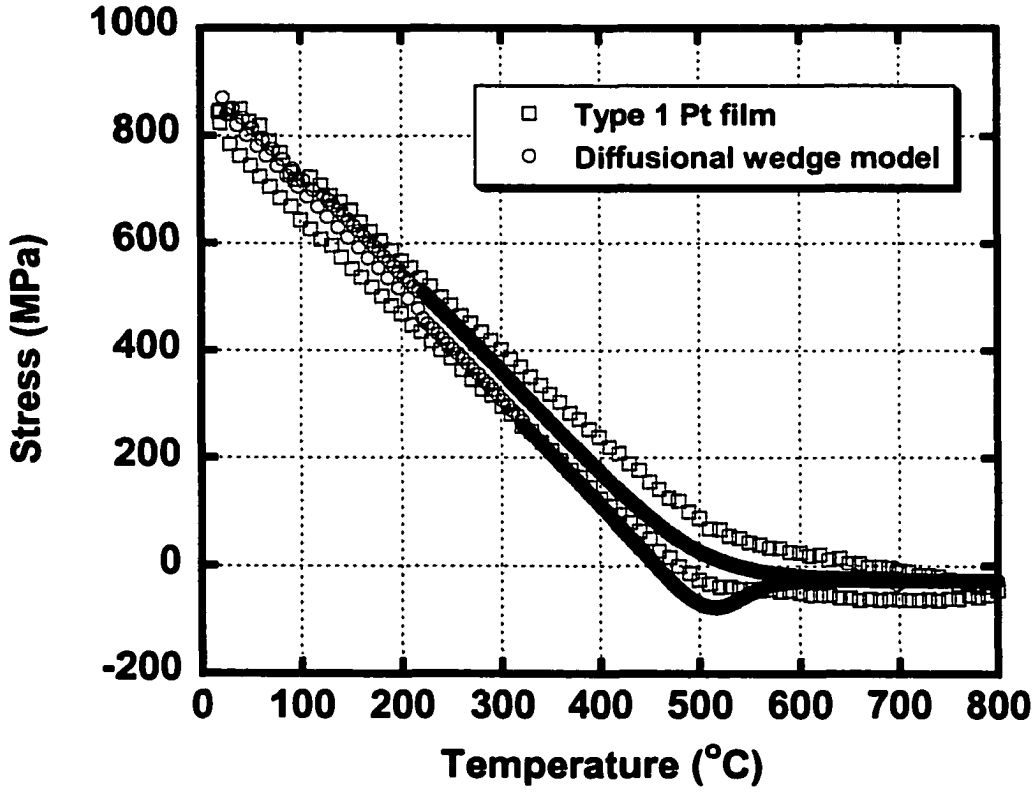

Figure 7.14. Diffusional wedge model and measured stress-temperature curve of Pt film (type 1). The model can closely reproduce the stress-temperature behavior by changing the thickness parameter from 200 nm to 100 nm.

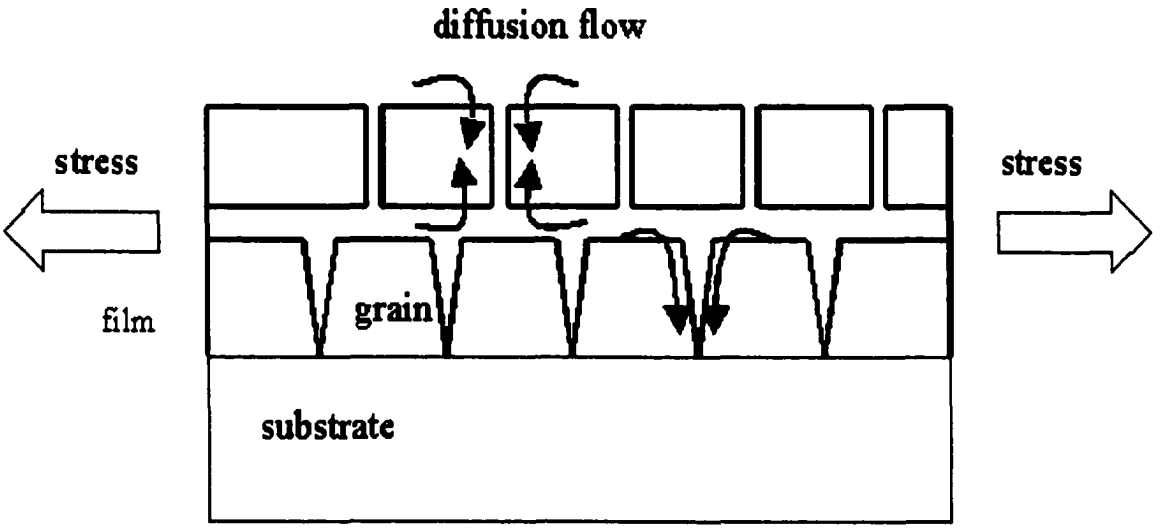

Figure.7.17. A schematic diagram of relaxation mechanisms in the small-grained film under tensile stress. Upper grains in the film follow the deformation maps model. Diffusion flow occurs freely between top and bottom grain boundaries. Bottom grains follow diffusional wedge model because substrate constraints at the bottom grains/substrate interface blocks the diffusional mechanism.

7.4 Summary and Conclusions

We have investigated the stress-temperature behavior of thin film Pt with different average grain sizes. The stress-temperature behavior of Pt films is similar to that of bare Cu film. Since Pt does not form a native oxide on the top, the relaxation mechanisms drop the stress almost to zero at high temperature. Two different microstructures in Pt films represent different stress evolutions at high temperature. The relaxation rate of the Pt film with the smallest grain size (type 1) is much faster than that of a Pt film having a relatively large grain size (type 3b). Two relaxation mechanism models, the deformation maps model and the diffusional wedge model, have been used to understand the stress-temperature behavior of Pt films. The deformation maps model inaccurately predicts stress-temperature behavior since the model predicts a stress free state above 350°C. The model is based on the assumption that diffusional mechanism can occur at the interface between film and substrate. However, the relaxation mechanisms should be inhibited due to a bonding between film and substrate. Diffusional wedge model including the effect of the substrate constraint on the stress relaxation agrees with the stress-temperature behavior of Pt thin films. A combination of the two models is found to be most accurate in the case of a non-columnar film by changing the thickness parameter.

Consistent with the domination of diffusion at high temperature, solid solution strengthening is found to be ineffective above approximately 600°C. This illustrates an example of the effect of scale on mechanical behavior.

Ch. 8 Conclusions

In this dissertation, we have investigated the mechanical behavior of Pt and Pt-Ru thin films. Nanoindentation and wafer curvature techniques were used to examine the mechanical properties of the films. The conclusions of the mechanical behavior of Pt and Pt-Ru alloy thin films are reviewed here. Recommendations for future work are also presented.

Microstructure dependent deformation behavior was systematically explored to understand pop-in behavior of polycrystalline materials. A small-grained film and a large-grained film displayed very different loading behaviors. The length scale of deformation is very sensitive to microstructure length scale (grain size). The effect of grain size on the plastic deformation was investigated. The first pop-in behavior is understood as an elastic-plastic transition. Grain boundaries play an important role in the load-displacement behavior of Pt films. The loading behaviors of Pt films are described as a dislocation activity. However, the dislocation model only describes the experimental results qualitatively. Quantitative analysis is required to have a better understanding of deformation mechanisms in terms of grain size and grain boundary area.

The strengthening mechanisms of solid-solution alloy thin films were investigated to improve fundamental understanding of the deformation mechanisms of thin films. The hardness of the solid solution alloy films is increased by an increase in Ru content. The predicted flow stress and measured flow stress both increase and show similar tendencies. A flow stress model based on dislocation motion in thin films, which includes three strengthening terms due to substrate constraint, grain size strengthening and solid

solution strengthening, does a reasonable job of predicting the flow stress change according to the Ru content. The detailed analyses of three strengthening mechanisms show that that the solid solution strengthening mechanism is mostly responsible for the film hardening. The different hardness values from two unique test methods, nanoindentation and wafer curvature techniques, were evaluated, and a modified Tabor equation describes new hardness and flow stress relationship.

Thermocycling behaviors of Pt films with different grain sizes were investigated to understand stress relaxation mechanisms. Grain size dependent stress-temperature behavior were observed. Two models, the deformation mechanism map model and the diffusional wedge model, were explored to explain the mechanical behavior of Pt thin films according to thermal cycling. Diffusional wedge model does predict the stress-temperature behavior of Pt films. The model is very effective for thin and small-grained film. However, these models ignore the effects of strain hardening (dislocation effects) on relaxation mechanisms of thin films. The dislocation mechanism may be active for the stress-temperature behavior during thermal cycling. This modification will be investigated for further study in this area.

Grain sizes of annealed films decrease according to Ru content. The solute atoms may drag grain boundary motion resulting in grain size decrease. However, from these observations it cannot be determined if the measured grain sizes are the maximum possible for each composition or if they simply indicate significant differences in growth rate. Grain growth mechanism in terms of solute content should be investigated.

Hillock formations on Pt and Pt-Ru films after certain annealing conditions were also examined to understand hillocks mechanisms. Several factors including composition

and annealing atmosphere affect the hillock formation. Although cross-section images of hillocks suggest that grain boundary sliding is a main mechanism, detailed analysis of hillock mechanisms is required to understand hillock formation (buckling type) on Pt and Pt-Ru thin films.

This work has been explored to refine the understanding of mechanical behaviors in thin films. Through the dissertation, Pt and Pt-Ru thin films have been investigated by using the nanoindentation and wafer curvature techniques. Several unique mechanical behaviors of the films are attributed to microstructures according to grain size and composition.

Kristensen, N., Ericson, F., Schweitz, J. A., and Smith, U. (1991) "Grain collapses in strained aluminum thin films," Journal of Applied Physics, 69, 2097.

Lee S., Bravman, J. C., Doan, J. C., Lee, S., Flinn, P. A., and Marieb, T. N. (2002) "Stress-induced and electromigration voiding in aluminum interconnects passivated with silicon nitride," Journal of Applied Physics, 91, 3653.

Lee, J., Johnson, L., Safari, A., Ramesh, R., Sands, T., Gilchrist, H., and Keramidas, V. G. (1993) "Effects of crystalline quality and electrode material on fatigue in $Pb(Zr,Ti)O_3$ thin film capacitors," Applied Physics Letters, 63, 27.

Li, P., Lu, T. M., and Bakhru, H. (1991) "High charge storage in amorphous $BaTiO_3$ thin films," Applied Physics Letters, 58, 2639.

Mattox D.M. (1982) "in Deposition technologies for films and coatings-development and applications," 63.

Olowolafe, J. O., Jones, R. E., Jr., Campbell, A. C., Hegde, R. I., Mogab, C. J., and Gregory, R. B. (1993) "Effects of anneal ambients and Pt thickness on Pt/Ti and Pt/Ti/TiN interfacial reactions," Journal of Applied Physics, 73, 1764.

Parikh, N. R., Stephen, J. T., Swanson, M. L., and Myers, E. R. (1990) "Study of diffusion barriers for PZT deposited on Si for nonvolatile random-access memory technology," Mat.Res.Soc.Proc., 200, 193.

Ramesh, R., Chan, W. K., Wilkens, B., Gilchrist, H., Sands, T., Tarascon, J. M., Keramidas, V. G., Fork, D. K., Lee, J., and Safari, A. (1992) "Fatigue and retention in ferroelectric Y-Ba-Cu-O/Pb-Zr-Ti-O/Y-Ba-Cu-O heterostructures," Applied Physics Letters, 61, 1537.

Sakuma, T., Yamamichi, S., Matsubara, S., Yamaguchi, H., and Miyasaka, Y. (1990) "Barrier layers for realization of high capacitance density in $SrTiO_3$ thin-film capacitor on silicon," Applied Physics Letters, 57, 2431.

Savitsky, E. et al. (1978) "MIR Publication," Moscow

Spierings, G. A. C. M., Dormans, G. J. M., Moors, W. G. J., Ulenaers, M. J. E., and Larsen, P. K. (1995) "Stresses in $Pt/Pb(Zr,Ti)O_3$ Pt thin-film stacks for integrated ferroelectric capacitors," Journal of Applied Physics, 78, 1926.

Sreenivas, K. and Sayer, M. (1988) "Characterization of $Pb(Zr,Ti)O_3$ thin films deposited from multi-element metal targets," Journal of Applied Physics, 64, 1484.

Takemura, K., Sakuma, T., and Miyasaka, Y. (1994) "High dielectric constant (Ba,Sr)TiO/sub 3/ thin films prepared on RuO_2 sapphire," Applied Physics Letters, 64, 2967.

Thouless, M. D., Gupta, J., and Harper, J. M. E. (1993) "Stress development and relaxation in copper films during thermal cycling," Journal of Materials Research, 8, 1845.

Tu, K-N, Mayer, J. W., and Feldman, L. C. (1992) "Electronic thin film science for electrical engineers and materials scientists,"

Usikov, M. P. et al. (1981) Russian Metallurgy-USSR, 5, 114.

Chapter 2

"Metals handbook Properties and selection" (1990); Nonferrous alloys and special purpose materials," 707.

d'Heurle, F. M. and Harper, J. M. E. (1989) "Note on the origin of intrinsic stresses in films deposited via evaporation and sputtering," Thin Solid Films, 171, 81.

Flinn, P. A., Gardner, D. S., and Nix, W. D. (1987) "Measurement and interpretation of stress in aluminum-based metallization as a function of thermal history," IEEE Transactions on Electron Devices, ED-34, 689.

Flinn, P. A. and Chien, Chiang (1990) "X-ray diffraction determination of the effect of various passivations on stress in metal films and patterned lines," Journal of Applied Physics, 67, 2927.

Flinn, P. A. (1991) "Measurement and interpretation of stress in copper films as a function of thermal history," Journal of Materials Research, 6, 1498.

Freund, L. B. (1987) "Stability of a dislocation threading a strained layer on a substrate," Journal of Applied Mechanics, Transactions ASME, 54, 553.

Gao, H., Zhang, L., Nix, W. D., Thompson, C. V., and Arzt, E. (1999) "Crack-like grain-boundary diffusion wedges in thin metal films," Acta Materialia, 47, 2865.

Griffin, A. J., Jr., Brotzen, F. R., and Dunn, C. (1986) "Hall-Petch relation in thin film metallizations," Scripta Metallurgica, 20, 1271.

Grovenor, C. R. M., Hentzell, H. T. G., and Smith, D. A. (1984) "Development of grain structure during growth of metallic films," Acta Metallurgica, 32, 773.

Hoffman, D. W. and Thornton, J. A. (1982) "Internal stresses in Cr, Mo, Ta, and Pt films deposited by sputtering from a planar magnetron source," Journal of Vacuum Science and Technology, 20, 355.

Kang, Y. S., Ho, P. S., Knipe, R., and Tregilgas, J. (1997) "Film thickness effect on tensile properties and microstructures of submicron aluminum thin films on polyimide," Thin Films: Stresses and Mechanical Properties VI.Symposium, 35.

Kim, D. K., Nix, W. D., Vinci, R. P., Deal, M. D., and Plummer, J. D. (2001) "Study of the effect of grain boundary migration on hillock formation in Al thin films," Journal of Applied Physics, 90, 781.

Kretschmann, A., Kuschke, W. M., Baker, S. P., and Arzt, E. (1997) "Plastic deformation in thin copper films determined by X-ray micro-tensile tests," Thin Films: Stresses and Mechanical Properties VI.Symposium, 59.

Massalski T B, Okamoto H, Subramanian P.R., and Kacprzak L (1990) "Binary Alloy Phase Diagrams,"

Movchan, B. A. and Demchishin, A. V. (1969) "Investigation of the structure and properties of thick vacuum- deposited films of nickel, titanium, tungsten, alumina and zirconium dioxide," Fizika Metallov i Metallovedenie, 28, 653.

Nix, W. D. (1989) "Mechanical properties of thin films," Metallurgical Transactions A (Physical Metallurgy and Materials Science), 20A, 2217.

Ohring M. (1992) "The Material science of thin films," Academic press, INC.

Oliver, W. C. and Pharr, G. M. (1992) "Improved technique for determining hardness and elastic modulus using load and displacement sensing indentation experiments," Journal of Materials Research, 7, 1564.

Ruud, J. A., Josell, D., and Spaepen, F. (1993) "New method for tensile testing of thin films," Journal of Materials Research, 8, 112.

Sanchez, J. E. and Arzt, E. Jr (1992) "Effects of grain orientation on hillock formation and grain growth in aluminum films on silicon substrates," Scripta Metallurgica et Materialia, 27, 285.

Shen, Y. L., Suresh, S., He, M. Y., Bagchi, A., Kienzle, O., Ruhle, M., and Evans, A. G. (1998) "Stress evolution in passivated thin films of Cu on silica substrates," Journal of Materials Research, 13, 1928.

Thompson, C. V. (1993) "The yield stress of polycrystalline thin films," Journal of Materials Research, 8, 237.

Thompson, C. V. (1993) "Texture evolution during grain growth in polycrystalline films," Scripta Metallurgica et Materialia, 28, 167.

Thornton, J. A. (1977) "High rate thick film growth," Annual Reviews Mater.Sci., 239.

Thornton, J. A., Tabock, J., and Hoffman, D. W. (1979) "Internal stresses in metallic films deposited by cylindrical magnetron sputtering," Thin Solid Films, 64, 111.

Thouless, M. D., Gupta, J., and Harper, J. M. E. (1993) "Stress development and relaxation in copper films during thermal cycling," Journal of Materials Research, 8, 1845.

Thouless, M. D. (1993) "Effect of surface diffusion on the creep of thin films and sintered arrays of particles," Acta Metallurgica et Materialia, 41, 1057.

Turlo, J. F (1992) "Ph.D. Dissertation," Stanford University.

Usikov M.P, Stepanova G.S, and Rytvin E.I (1981) "Russian Metallurgy-USSR,"

Venkatraman, R. and Bravman, J. C. (1992) "Separation of film thickness and grain boundary strengthening effects in Al thin films on Si," Journal of Materials Research, 7, 2040.

Vlassak, J. J. and Nix, W. D. (1992) "New bulge test technique for the determination of Young's modulus and Poisson's ratio of thin films," Journal of Materials Research, 7, 3242.

Chapter 3

Ackland, D. at Lehigh university TEM sample preparation lab.

Fahey, K. P. (1998), Ph.D dissertation, Stanford University

Flinn, P. A., Gardner, D. S., and Nix, W. D. (1987) "Measurement and interpretation of stress in aluminum-based metallization as a function of thermal history," IEEE Transactions on Electron Devices, ED-34, 689.

Gelius, U., Wannberg, B., and Baltzer, P (1990) "A new ESCA instrument with improved surface sensitivity, fast imaging properties and excellent energy resolution," Journal of Electron Spectroscopy and Related Phenomena, 52, 747.

Kim, J. (2001), "Ph.D dissertation," Lehigh University

Reyntjens, S. and Puers, R. (2001) "A review of focused ion beam applications in microsystem technology," Journal of Micromechanics and Microengineering, 11, 287.

Ristau, R. (1998), "Ph.D Dissertation," Lehigh University

Chapter 4

Bhatt, H. J. (1971) "Superior aluminum for interconnections of integrated circuits," Applied Physics Letters, 19, 30.

Chang, C. Y. and Vook, R. W. (1993) "Effect of surface aluminum oxide films on thermally induced hillock formation," Thin Solid Films, 228, 205.

Chaudhari, P. (1974) "Hillock growth in thin films," Journal of Applied Physics, 45, 4339.

Dell'oca, C. J. and Learn, A. J. (1971) "Anodization of aluminum to inhibit hillock growth during high temperature processing (semiconductor device processing)," Thin Solid Films, 8, R47.

Eichorst, D. J., Blanton, T. N., Barnes, C. L., and Bosworth, L. A. (1994) "Influence of processing conditions on hillock formation in electron-beam evaporated platinum/titanium films," Integrated Ferroelectrics, 4, 239.

Ericson, F., Kristensen, N., Schweitz, J. A., and Smith, U. (1991) "A transmission electron microscopy study of hillocks in thin aluminium films," Journal of Vacuum Science & Technology B (Microelectronics Processing and Phenomena), 9, 58.

Genin, F. Y. (1995) "Initial stages of the formation of holes and hillocks in thin films under equal biaxial stress," Acta Metallurgica et Materialia, 43, 4289.

Hren, P. D., Rou, S. H., Al Shareef, H. N., Ameen, M. S., and Aucielto, O. (1992) "Bottom electrodes for integrated Pb(Zr, Ti)O_3 films," Integrated Ferroelectrics, 2, 311.

Iwamura, E., Ohnishi, T., and Yoshikawa, K. (1995) "A study of hillock formation on Al-Ta alloy films for interconnections of TFT-LCDs," Thin Solid Films, 270, 450.

Kim, D. K., Heiland, B., Nix, W. D., Arzt, E., Deal, M. D., and Plummer, J. D. (2000) "Microstructure of thermal hillocks on blanket Al thin films," Thin Solid Films, 371, 278.

Kim, D.K., (2001), Ph.D Dissertation, Stanford University

Lahiri, S. K. and Wells, O. C. (1969) "Reversible hillock growth in thin films," Applied Physics Letters, 15, 234.

Lahiri, S. K. (1970) "Stress relief and hillock formation in thin lead films," Journal of Applied Physics, 41, 3172.

Lahiri, S. K. (1975) "Absence of hillock formation in epitaxial lead films," Journal of Applied Physics, 46, 2791.

Lee, W. J., Kim, Y. M., and Kim, H. G. (1995) "Pt-base electrodes and effects on phase formations and electrical properties of high-dielectric thin films," Thin Solid Films, 269, 75.

Marshall, D. B. and Evans, A. G. (1984) "Measurement of adherence of residually stressed thin films by indentation. I. Mechanics of interface delamination," Journal of Applied Physics, 56, 2632.

Matsui, Y., Hiratani, M., Kumagai, Y., Miura, H., and Fujisaki, Y. (1998) "Thermal stability of Pt bottom electrodes for ferroelectric capacitors," Japanese Journal of Applied Physics, Part 2 (Letters), 37, L465.

Nowell, M. M. and Field, D. P. (1998) "Texture and grain boundary structure dependence of hillock formation in thin metal films," Materials Reliability in Microelectronics VIII.Symposium, 115.

Ronay, M. and Aliotta, C. F. (1980) "Hillock formation in lead films by grain boundary sliding," Philosophical Magazine A (Physics of Condensed Matter, Defects and Mechanical Properties), 42, 161.

Sanchez, J. E. and Arzt, E. Jr (1992) "Effects of grain orientation on hillock formation and grain growth in aluminum films on silicon substrates," Scripta Metallurgica et Materialia, 27, 285.

Tao X. (2002), Personal communication, Lehigh university

Tu, K-N, Mayer, J. W., and Feldman, L. C. (1992) "Electronic thin film science for electrical engineers and materials scientists,"

Zielinski, E. M. (1995), "Ph.D Dissertation," Stanford University

Chapter 5

Bahr, D. F., Kramer, D. E., and Gerberich, W. W. (1998) "Non-linear deformation mechanisms during nanoindentation," Acta Materialia, 46, 3605.

Conrad, H. and Narayan, J. (2000) "On the grain size softening in nanocrystalline materials," Scripta Materialia, 42, 1025.

Doerner, M. F. and Nix, W. D. (1986) "A method for interpreting the data from depth-sensing indentation instruments," Journal of Materials Research, 1, 601.

Ma Q. and Clarke D.R. (1995) "Size dependent hardness of silver single crystals," Journal of Materials Research, 10, 853.

Michalske, T. A. and Houston, J. E. (1998) "Dislocation nucleation at nano-scale mechanical contacts," Acta Materialia, 46, 391.

Nix, W. D. and Huajian, Gao (1998) "Indentation size effects in crystalline materials: a law for strain gradient plasticity," Journal of the Mechanics and Physics of Solids, 46, 411.

Oliver, W. C., McHargue C.J., Farlow G.C., and White C.W. (1984) "The hardness of ion implanted ceramics," Mat.Res.Soc.Symp.Proc., 24, 515.

Oliver, W. C. and Pharr, G. M. (1992) "Improved technique for determining hardness and elastic modulus using load and displacement sensing indentation experiments," Journal of Materials Research, 7, 1564.

Page, T. F., Oliver, W. C., and McHargue, C. J. (1992) "The deformation behavior of ceramic crystals subjected to very low load (nano)indentations," Journal of Materials Research, 7, 450.

Shen, Y. L., Suresh, S., He, M. Y., Bagchi, A., Kienzle, O., Ruhle, M., and Evans, A. G. (1998) "Stress evolution in passivated thin films of Cu on silica substrates," Journal of Materials Research, 13, 1928.

Suresh, S., Nieh, T. G., and Choi, B. W. (1999) "Nano-indentation of copper thin films on silicon substrates," Scripta Materialia, 41, 951.

Tao X. (2002) Personnel communication.

Vitovec F.H. (1986) "in Microindenation Technique in materials science and engineering," 175.

Yamakov, V., Wolf, D., Salazar, M., Phillpot, S. R., and Gleiter, H. (2001) "Length-scale effects in the nucleation of extended dislocations in nanocrystalline Al by molecular-dynamics simulation," Acta Materialia, 49, 2713.

Zielinski E.M. (1995) "Ph.D. Dissertation," Stanford University.

Zimmerman, J. A., Kelchner, C. L., Klein, P. A., Hamilton, J. C., and Foiles, S. M. (2001) "Surface step effects on nanoindentation," Physical Review Letters, 87, 165507/1.

Chapter 6

Ashby, M. F. (1970) "The deformation of plastically non-homogeneous materials," Philosophical Magazine, 21, 399.

Cahn R.W and Haasen P., (1996) "Physical Metallurgy," Elsevier Science BV.

Fleck, N. A. and Hutchinson, J. W. (1993) "Phenomenological theory for strain gradient effects in plasticity," Journal of the Mechanics and Physics of Solids, 41, 1825.

Freund, L. B. (1987) "Stability of a dislocation threading a strained layer on a substrate," Journal of Applied Mechanics, Transactions ASME, 54, 553.

Haasen P (1996) "Physical metallurgy," Cambridge University press.

Hansen, N. (1977) "The effect of grain size and strain on the tensile flow stress of aluminium at room temperature," Acta Metallurgica, 25, 863.

Huang, Haibo and Spaepen, F. (2000) "Tensile testing of free-standing Cu, Ag and Al thin films and Ag/Cu multilayers," Acta Materialia, 48, 3261.

Hughes, G. D., Smith, S. D., Pande, C. S., Johnson, H. R., and Armstrong, R. W. (1986) "Hall-Petch strengthening for the microhardness of twelve nanometer grain diameter electrodeposited nickel," Scripta Metallurgica, 20, 93.

Keller, R., Baker, S. P., and Arzt, E. (1998) "Quantitative analysis of strengthening mechanisms in thin Cu films: effects of film thickness, grain size, and passivation," Journal of Materials Research, 13, 1307.

Kobrinsky, M. J. and Thompson, C. V. (1998) "The thickness dependence of the flow stress of capped and uncapped polycrystalline Ag thin films," Applied Physics Letters, 73, 2429.

Labusch, R. (1970) "A statistical theory of solid solution hardening," Physica Status Solidi, 41, 659.

Murarka S.P. (1993) "Metallization theory and practice for VLSI and ULSI ," Butterworth-Heinemann.

Nix, W. D. (1989) "Mechanical properties of thin films," Metallurgical Transactions A (Physical Metallurgy and Materials Science), 20A, 2217.

Nix, W. D. and Huajian, Gao (1998) "Indentation size effects in crystalline materials: a law for strain gradient plasticity," Journal of the Mechanics and Physics of Solids, 46, 411.

Hren, P. D., Al shareef, H., Rou, S. H., Kingon, A. I., Buaud, P., and Irene, E. A. (1992) "Hillock formation in platinum films," Advanced Metallization and Processing for Semiconductor Devices and Circuits - II.Symposium, 575.

Jackson, M. S. and Che-Yu, Li (1982) "Stress relaxation and hillock growth in thin films," Acta Metallurgica, 30, 1993.

Keller, R. M., Kuschke, W. M., Kretschmann, A., Bader, S., Vinci, R. P., and Arzt, E. (1995) "Influence of film thickness and capping layer on the mechanical properties of copper films," Materials Research Society Symposium Proceedings, 391, 309.

Nix, W. D. (1998) "Personal communication"

Spierings, G. A. C. M., Dormans, G. J. M., Moors, W. G. J., Ulenaers, M. J. E., and Larsen, P. K. (1995) "Stresses in Pt/Pb(Zr,Ti)O/sub 3//Pt thin-film stacks for integrated ferroelectric capacitors," Journal of Applied Physics, 78, 1926.

Thornton, J. A., Tabock, J., and Hoffman, D. W. (1979) "Internal stresses in metallic films deposited by cylindrical magnetron sputtering," Thin Solid Films, 64, 111.

Thouless, M. D., Gupta, J., and Harper, J. M. E. (1993) "Stress development and relaxation in copper films during thermal cycling," Journal of Materials Research, 8, 1845.

Turlo, J. F (1992) "Ph.D. Dissertation," Stanford University.

Usikov, M.P. (1980) " Influence of alloying (with Pd, Rh, Ir, Ru) on the dislocation structure and high-temperature creep of platinum," Russian Metallurgy-USSR, 5, 114

Vinci, R. P., Zielinski, E. M., and Bravman, J. C. (1995) "Thermal strain and stress in copper thin films," Thin Solid Films, 262, 142.

VITA

Seungmin Hyun was born on February 5, 1969 to Sukha Hyun and Yookap Kim in Seoul, Korea. After graduating from Banpo High School, Seoul, he entered Korea University and began his undergraduate study in the spring of 1988. He earned a Bachelor degree in Material Science in February 1992. He continued graduate study in the same department. He was awarded the Master of Science degree in Material Science in August 1995. During the years of 1992 to 1994, he also served in military. He started his Ph.D study at Lehigh University in August 1996. During Ph.D study, he was a research assistant in the Department of Materials Science and Engineering. His research topic is the mechanical behavior of metal thin films for microelectronic applications.